InAs/GaAs Quantum Dot Solar Cells

Frank Kafui Kwame Tutu

A thesis submitted to University College London for the degree of
Doctor of Philosophy (PhD)

Department of Electronic & Electrical Engineering
University College London

November 2013

Statement of Originality

I, Frank Kafui Kwame Tutu confirm that the work presented in this thesis is my own. Where information has been derived from other sources, I confirm that this has been indicated in the thesis.

Signed: _____

Date: _____

To my mother, Mrs. Rosina Tutu
and my father, Mr. Prosper Tutu.

Abstract

Self-assembled III-V quantum dots (QDs) have been intensely studied for potential applications in solar cell (SC) devices in order to increase power conversion efficiency. Due to their quantum confinement of carriers, QDs have been proposed as a means of implementing the intermediate band solar cell (IBSC). The IBSC concept is characterised by in an increase in photocurrent and a preservation of output voltage, resulting from an enhanced sensitivity to the solar spectrum. The work reported in this thesis is concerned with the development of InAs QDs in GaAs *p-i-n* solar cell structures, with the aim of realising of an IBSC. The work involves the design, epitaxial growth by molecular beam epitaxy (MBE), device processing and characterisation of the QDSCs.

This thesis first investigates InAs/InGaAs dot-in-a-well (DWELL) solar cell structures grown under different conditions. The use of a high-growth-temperature GaAs spacer layers is demonstrated to significantly enhance the performance of the multilayer DWELL solar cells. Threading dislocations were observed for a 30-layer QD structure with GaAs spacer layers grown at a low temperature (510 ^{o}C). By growing the GaAs spacer layer at a higher temperature (580 ^{o}C), the formation of threading dislocations were suppressed, resulting in enhanced optical properties.

The thesis then goes on to address the main challenges facing QD IBSCs, that is, the reduction in open-circuit voltage and the lack of significant increase in short-circuit current. To eliminate the wetting layer and enhance the open-circuit voltage of the QD solar cell, an AlAs cap layer technique was used. This resulted in an enhancement of the open-circuit voltage of a 20-layer InAs/GaAs QDSC from 0.69 V to 0.79 V. Despite a slight reduction in short-circuit current, for the QDSC with AlAs cap layer, the enhancement in the open-circuit voltage was enough to ensure that its efficiency is higher than the QDSC without AlAs cap layers.

In an attempt to enhance the short-circuit current, an antimony-mediated growth approach was used to grow high-density QDs. After optimisation of the growth temperature and InAs coverage, a very high in-plane QD density of 1×10^{11} cm^{-2} was achieved by applying a few monolayers of antimony prior to QD growth. Compared with a reference QDSC without the incorporation of antimony, the high-density QDSC demonstrates a distinct improvement in short-circuit current from 7.4 mA/cm^2 to 8.3 mA/cm^2. This result shows that a significant increase in short-circuit current could potentially compensate for the drop in open-circuit voltage observed in InAs/GaAs QD solar cells.

Ongoing work on the development of QDSCs with both AlAs capping and antimony-mediated growth have resulted in the simultaneous elimination of the wetting layer and increase in QD absorption in a single device. Overall, the studies in this thesis present important implications for the design and growth of InAs/GaAs QD solar cell structures for the implementation of IBSCs.

Acknowledgements

First, I would like to thank my supervisor Prof. Huiyun Liu for his guidance and support over the last three years. Without his supervision and insightful feedback, I would not have been able to achieve a lot in my PhD research. I would also like to acknowledge all the members of the UCL MBE group, for their friendship and the many stimulating discussions. Dr. Ting Wang, Andrew Lee, Kevin Lee, Dr. Qi Jiang, Dr. Jiang Wu, Dr. Sabina Hatch, Phu Lam, Mingchu Tang and Yunyan Zhang. It was a pleasure working with you all and being part of the group. Special thanks to Prof. Izzat Darwazeh and Dr. Tony Kenyon, both of whom took a personal interest in my success and have been a great source of help and encouragement over the years.

I would like to thank my second supervisor, Dr. Ned Ekins-Daukes of the Quantum Photovoltaics (QPV) group at Imperial College for helping me develop an understanding of the design and characterisation of solar cells. Thanks Ned; you are an inspiration to me, in more ways than you know. I am also grateful to the rest of the QPV group, particularly Kan-Hua Lee, for assisting me with building experimental set-ups and taking measurements in their laboratories.

I would like to thank Prof. Yoshitaka Okada of the Research Center for Advanced Science and Technology, University of Tokyo for his collaboration and kindness. It was for me, the major highlight of the last three years to spend time at the University of Tokyo working with Prof. Okada and the members of the Okada laboratory. I am especially grateful to Dr. Naoya Miyashita and Dr. Yasushi Shoji, for taking time to teach and assist me with device fabrication.

Finally, I would like to express my deepest gratitude to my family; my parents and siblings, Anita Ansu-Gyamfi, Ebenezer Tutu and Annette Tutu, for their patience and encouragement over the course of my PhD project. I am also grateful for great friends like Thomas Allen, Binh Chu and Jerry Thambirajah, who have supported and put up with me in happy and gloomy times.

Table of Contents

List of Figures

List of Tables

List of Publications

Journal Publications:

1. F. K. Tutu, J. Wu, P. Lam, M. Tang, N. Miyashita, Y. Okada, J. Wilson, R. Allison, and H. Liu, "Antimony mediated growth of high-density InAs quantum dots for photovoltaic cells," *Applied Physics Letters*, 103, no. 4, p. 043901, 2013.

2. F. K. Tutu, P. Lam, J. Wu, N. Miyashita, Y. Okada, K.-H. Lee, N. J. Ekins-Daukes, J. Wilson, and H. Liu, "InAs/GaAs quantum dot solar cell with an AlAs cap layer," *Applied Physics Letters*, vol. 102, no. 16, p. 163907, 2013.

3. F. K. Tutu, I. R. Sellers, M. G. Peinado, C. E. Pastore, S. M. Willis, A. R. Watt, T. Wang, and H. Y. Liu, "Improved performance of multilayer InAs/GaAs quantum-dot solar cells using a high-growth-temperature GaAs spacer layer," *Journal of Applied Physics*, vol. 111, no. 4, p. 046101, 2012.

4. S. M. Willis, J. A. R. Dimmock, F. Tutu, H. Y. Liu, M. G. Peinado, H. E. Assender, A. A. R. Watt, and I. R. Sellers, "Defect mediated extraction in InAs/GaAs quantum dot solar cells," *Solar Energy Materials and Solar Cells*, pp. 1–6, Apr. 2012.

5. T. Wang, A. Lee, F. Tutu, A. Seeds, H. Liu, Q. Jiang, K. Groom, and R. Hogg, "The effect of growth temperature of GaAs nucleation layer on InAs/GaAs quantum dots monolithically grown on Ge substrates," *Applied Physics Letters*, vol. 100, no. 5, pp. 052113–052113, 2012.

6. H. Liu, T. Wang, Q. Jiang, R. Hogg, F. Tutu, F. Pozzi, and A. Seeds, "Long-wavelength InAs/GaAs quantum-dot laser diode monolithically grown on Ge substrate," *Nature Photonics*, no. JUNE, pp. 1–4, Jun. 2011.

Conference and Symposia Publications:

1. F. K. Tutu, P. Lam, J. Wu, N. Miyashita, Y. Okada, K.-H. Lee, N. J. Ekins-Daukes, J. Wilson, and H. Liu, "InAs/GaAs quantum dot solar cell with an AlAs cap layer," *UK Semiconductor Conference, University of Sheffield* (2013).

2. F. K. Tutu, I. R. Sellers, M. G. Peinado, C. E. Pastore, S. M. Willis, A. R. Watt, T. Wang, and H. Y. Liu, "Improved performance of multilayer InAs/GaAs quantum-dot solar cells using a high-growth-temperature GaAs spacer layer," *Advances in Photovoltaics Conference, Institute of Physics, London* (2011).

3. F. K. Tutu, I. R. Sellers, M. G. Peinado, C. E. Pastore, S. M. Willis, A. R. Watt, T. Wang, and H. Y. Liu, "Improved performance of multilayer InAs/GaAs quantum-dot solar cells using a high-growth-temperature GaAs spacer layer," *High-Efficiency Materials for Photovoltaics, Imperial College London* (2011).

4. F. K. Tutu, I. R. Sellers, M. G. Peinado, C. E. Pastore, S. M. Willis, A. R. Watt, T. Wang, and H. Y. Liu, "Improved performance of multilayer InAs/GaAs quantum-dot solar cells using a high-growth-temperature GaAs spacer layer," *UK Semiconductor Conference, University of Sheffield* (2011).

Chapter 1

Introduction

1.1 Introduction

The ability to harness and make use of energy, in all its different forms has played a fundamental role in human technological advancement. Indeed, over the centuries, there has been a correlation between a society's living standard and the amount of energy it consumes. Today, energy provision is one of the major challenges facing the globe. The increase in global energy demand, coupled with concerns about climate change, peak oil, and the desire for energy independence, is forcing policy makers to look for alternative energy sources to fuel future economic growth. It is therefore not surprising that the energy issue has been a topical subject in recent years. After the 2011 Fukushima nuclear power plant disaster in Japan, Germany's decision to abandon nuclear power is only a testimony to the fact that a safer, cleaner and more secure source of energy is desperately needed.

The International Energy Agency predicts that the next 50 years will see the global demand for energy more than double. This dramatic increase will be as a result of a combination of the increase in human population and the increase in global economic activity and output. Emerging markets such as China and India contribute significantly to this trend as they invest in

infrastructure and aspire to living standards in the West. Figure 1.1 shows the forecasted world marketed energy consumption.

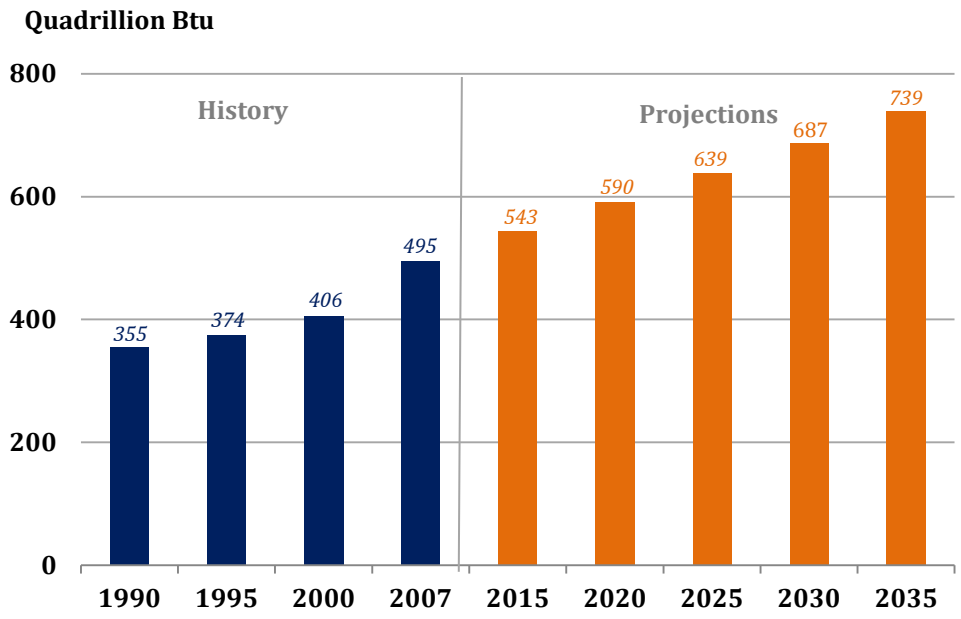

Figure 1.1 World Marketed Energy Consumption [1] **(Btu stands for British thermal unit; 1 Btu is equivalent to 1055 Joules)**

The push to transition from fossil fuels to renewable energies is not only necessitated by the exhaustion of oil and gas reserves, but also by the need to reduce greenhouse gas emissions. It is now widely accepted that climate change is caused by the increase in atmospheric concentrations of greenhouse gases such as CO_2, which is a by-product of the combustion of fossil fuels. A report by the Intergovernmental Panel on Climate Change (IPCC) states, "Warming of the climate system is unequivocal, as is now evident from observations of increases in global average air and ocean temperatures, widespread melting of snow and ice, and rising global average sea level [2]." A range of policies and sustainable development practices have been put in place by governments and international bodies to mitigate the effects of climate change, however the IPCC reports that even with current measures greenhouse gas emission will continue to grow [3].

The challenge therefore, is to produce energy to satisfy the inevitable rise in demand without the production of greenhouse gases. Solar energy has emerged, in the midst of all other renewable energy sources, as the most viable energy sources to meet this challenge, not only because of the sheer abundance of solar radiation reaching the earth's surface but also because solar energy technologies have shown drastic improvements in recent years. There is a large gap between the amount of solar energy used now and its colossal potential. The availability of solar energy is compared to that of other renewable energy sources in Figure 1.2. It is also worth noting that most of the sources of energy humans have learnt to harness, such as fossil fuel, hydroelectric power and wind energy can be traced one way or the other back to solar energy. The International Energy Agency recently predicted that photovoltaics and solar thermal plants might produce most of the world's energy demand by 2060. The U. S. National Academy of Engineering, in its Grand Engineering Challenges report [4], concludes that making solar energy more efficient and affordable is one of the greatest engineering challenge of the 21st Century.

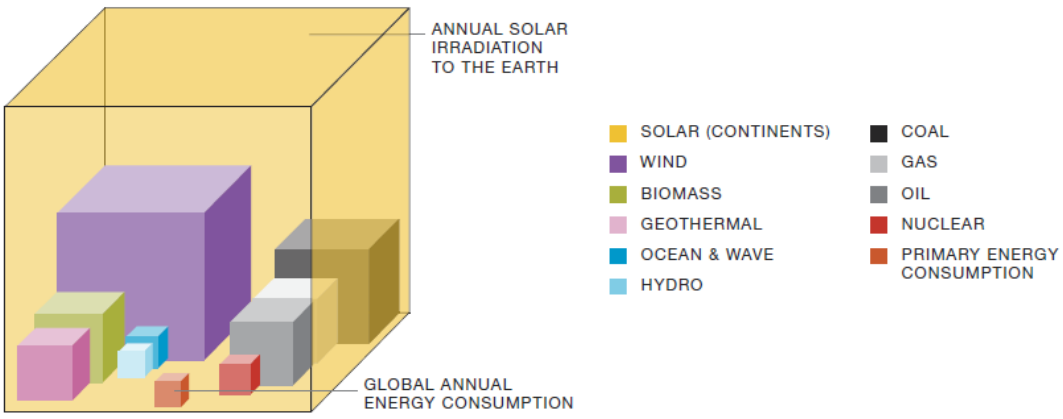

Figure 1.2 Solar Irradiation compared to renewable and established energy sources. (Fossil fuels are expressed with regard to their total reserves whereas renewable energies are expressed to their yearly potential) [5]

1.2 Photovoltaics

Life on Earth is dependent on the conversion of sunlight into other forms of energy. Photovoltaics are a simple but elegant way of harnessing the sun's energy by directly converting the incident solar radiation into electrical energy without moving parts or polluting by-products. Electrical energy is perhaps the most useful form of energy, as it can be easily converted to other forms of energy for immediate use.

Ever since the photovoltaic effect was discovered in 1839 by Edmund Becquerel, the idea of electrical energy from sunlight has proved fascinating to researchers. However, it wasn't until the 1950s that silicon photovoltaics were able to produce useful quantities of power. The first silicon solar cell had an efficiency of 6% [6]. In the 1960s, silicon solar cells were developed for space applications. The 1970s oil crisis called attention to the need for alternative energy sources and this led to solar cells being seriously considered for terrestrial applications. The investments in research and development made since then, have led to the exploration a plethora of solar cell materials in search of a route to low cost photovoltaics with high efficiencies. These materials include amorphous silicon (a-Si), crystalline silicon (c-Si), III-V compounds such as gallium arsenide (GaAs) and II-VI compounds such as cadmium telluride (CdTe) and copper indium gallium selenide (CIGS). Dye-sensitized and organic solar cells have also been of research interest in recent years [7]. However, silicon still remains the leading solar cell material, due to its relative low cost and the advancement of silicon technology from the microelectronics industry. But there are great challenges for further improving the efficiency of silicon-based solar cells.

Terrestrial photovoltaics have found applications in places where conventional electrical supply will be too expensive or impractical, for instance, remote telecommunication equipment, rural electrification and low power consumer electronics applications. Grid-connected photovoltaic systems have also shown a dramatic increase in the past decade. Today, photovoltaics can be found in both rural and urban settings. Due to their

aesthetic quality, solar cells have also found an application in architectural design, where in addition to producing electricity for a building, they also take the role of a building element. These are referred to as building integrated photovoltaics (BIPV).

1.2.1 Photovoltaic Market

The main challenge facing the photovoltaic industry since its inception has been the high production costs. However, due to innovation in the industry, costs have been dropping over the past decades and the global market for photovoltaics has grown significantly. For more than a decade, the photovoltaic industry has experienced an average annual growth rate of 40% [8]. Japan and Germany have led the way in terms of installed capacity due to government incentives. Most of the installed capacity is on-grid, meaning it is connected to the public utility electrical power network. Off-grid installations are common in developing countries where connection to a power grid might not be possible or in cases where it is more desirable to have a stand-alone power system. Figure 1.3 below shows the cumulative installed capacity from 2000 to 2011.

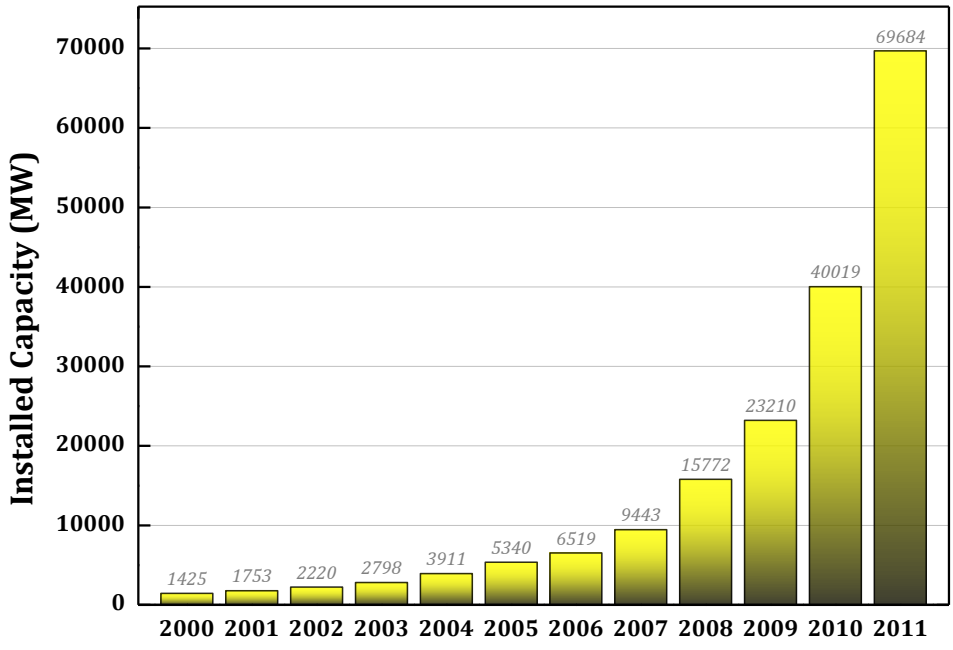

Figure 1.3 Global cumulative photovoltaic installed capacity (adapted from [9])

The adoption of solar energy is also being bolstered by emerging markets such as China and other developing countries, the majority of which are situated in climates where there is a significant amount of solar irradiation. Contrary to what many might believe, photovoltaics have been shown to contribute significantly to power supply even in regions with a dull and cloudy climate. The intermittent nature of solar energy generation is a drawback, but it has been shown that sunshine levels tend to coincide with peak demand periods, especially for commercial buildings.

1.2.2 Generations of Photovoltaics

The ultimate goal of research in photovoltaics is to reduce the cost of production per unit watt, in order to reach grid parity. Grid parity, defined as the point where photovoltaic electricity becomes competitive with electricity generated from more conventional energy sources such as coal, natural gas and nuclear reactors - is typically placed at US $1/W. Photovoltaic technologies can be broadly classified into three groups based on their operating characteristics, cost and efficiency. These are shown in Figure 1.4 as Generations I, II and III.

The first generation of solar cells are characterised by their high cost and relatively high efficiencies (up to 20%). These are solar cells made of crystalline silicon. The best laboratory efficiency achieved for a c-Si solar cell is 25% [10]. Most of the installed photovoltaic capacity today belongs to this group. Second generation photovoltaics refer to thin-film technologies where the semiconductor material is deposited on glass or metal foil. This ensures that only a small amount of material is used leading to a lower cost. Thin-film solar cells on the market now are generally made of a-Si, CdTe and CIGS with the best laboratory efficiencies at 10.1%, 16.7% and 19.4% respectively [10].

Research focus has turned to a new generation of solar cells with the possibility of providing high efficiencies at a lower cost. Possible implementation paths for these cells include multijunction solar cells (MJSC) [11], hot carrier solar cells [12] and intermediate band solar cells (IBSC) [13].

Perhaps the most common of the third generation cells is the multijunction solar cell, where two or more cells are stacked and connected to each other in order to absorb more of the solar spectrum. A triple junction GaInP/GaInAs/Ge solar cell has been demonstrated with an efficiency of 41.1%, however the manufacturing costs still remain high [14].

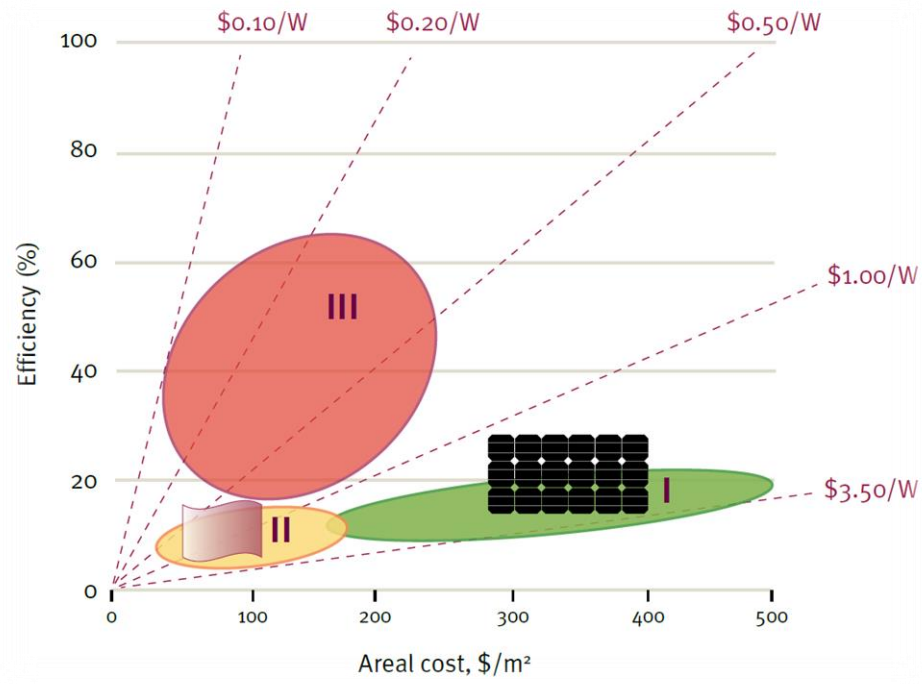

Figure 1.4 Three Generation of Photovoltaic Technology [15]

1.2.3 Quantum Dot Intermediate Band Solar Cells

The IBSC concept is a third generation approach much like the multijunction cell, in that it also aims to increase efficiency by enhancing spectral sensitivity. The difference is that it is a single junction cell. The idea behind this approach is the introduction of an intermediate band within the bandgap of a semiconductor, allowing sub-bandgap absorption of lower energy photons. This will lead to an increase in the current from the cell and provided the voltage is not reduced; an increase in efficiency will be attained. Theoretical calculations predict that intermediate band solar cell could achieve efficiencies as high as 63% under concentrated sunlight [13]. There

have been a few proposals on how to implement the intermediate band but only one has proved promising. Attempts have been made to generate intermediate bands from deep levels in bulk materials. This approach is demonstrated by Si samples being highly doped with Ti [16]. Another bulk material approach uses highly mismatched alloys such as $Zn_{1-y}Mn_yO_xTe_{1-x}$ and $GaN_xAs_{1-x-y}P_y$. There is evidence that these alloys display intermediate band properties [17]. Compared to all other approaches the low-dimensional structure approach using quantum dots (QD) has produced the most practical results [18]. Therefore it is not surprising that most of the experimental effort has focused on this approach, particularly InAs/GaAs QDSCs. The QDs are placed in the intrinsic region of a *p-i-n* structure as a means of introducing the intermediate band.

1.3 Thesis Structure

This thesis describes the development of III-V QD material systems in an attempt to create high-efficiency QD IBSCs. The work involves the design, epitaxial growth, fabrication and characterisation of these solar cells. Epitaxial growth is done by molecular beam epitaxy (MBE) with six types of III-V element sources; indium, gallium, aluminium, arsenic, phosphorous and antimony. Variations of quantum dots structures incorporated into the intrinsic region of *p-i-n* GaAs solar cell structures were investigated.

Chapter 2 presents a theoretical background to solar cells. A concise outline of the physics of solar cells is presented along with a brief look at the solar resource. This is followed by a closer look at the IBSC concept and a detailed discussion on QD IBSCs. The challenges and implementation criteria for QD IBSC are also outlined.

Chapter 3 discusses the experimental methods involved in this project. The chapter begins with an introduction to MBE growth. The in-situ monitoring technique known as reflection high-energy electron diffraction (RHEED) is discussed, followed by a look at the growth mechanism of QDs. After that,

techniques of material quality characterisation such as atomic force microscopy (AFM) and transmission electron microscopy (TEM) are briefly explained. A discussion on III-V processing methods and the fabrication of solar cells is then presented. Lastly, photoluminescence (PL) and electrical characterisation methods such as external quantum efficiency (EQE) and current – voltage (IV) measurements are briefly discussed.

Chapter 4 outlines and compares the results of InAs/InGaAs dot-in-well (DWELL) solar cells grown under different temperature conditions. Firstly, the details of the MBE growth and device fabrication for the cells are outlined. The characterisation and analysis of the QDSC structures by TEM, AFM and PL are then presented. Subsequently, the performances of the solar cells are determined by EQE and light IV measurements.

The enhancement of the open-circuit voltage of InAs/GaAs QDSCs by an AlAs cap layer is demonstrated in Chapter 5. After the details of MBE growth and device fabrication are outlined, TEM, AFM and PL are presented to characterise the material quality of the solar cell structures. EQE, light IV and dark IV plots are discussed in the analysis of the solar cell performances. The chapter is concluded with a discussion on the implications of the achieved results for the design QD IBSCs.

An antimony-mediated growth approach was used to increase QD density, enhancing the short-circuit current of a QDSC, and this is discussed in Chapter 6. The chapter starts with a look at the optimisation of the growth temperature and InAs amount for the growth of high-density QDs. AFM and PL results of the growth study conducted are presented. Afterwards, the solar cell device characterisations by EQE, light IV and dark IV are discussed.

Concluding remarks, as well as ongoing work on QD IBSCs are presented in Chapter 7. The chapter highlights the most important aspects of the thesis. The final section of this chapter presents some suggestions for future work.

Bibliography

[1] US Energy Information Administration, "International Energy Outlook, 2010," Energy Information Administration, 2010.

[2] S. Solomon, D. Qin, M. Manning, M. Marquis, K. Averyt, M. B. Tignor, and H. L. Miller, "Climate change 2007: The Physical Science Basis," Apr. 2007.

[3] B. Metz, O. Davidson, P. Bosch, R. Dave, and L. Meyer, "Climate change 2007-Mitigation of climate change," 2007.

[4] US National Academy of Engineering, "Grand Challenges for Engineering," 2008.

[5] European Photovoltaic Industry Association, "Solar Generation 6: Solar Photovoltaic Electricity Empowering the World," 2011.

[6] J. Neslon, *The Physics of Solar Cells*. Imperial College Press, 2003.

[7] B. E. Hardin, H. J. Snaith, and M. D. McGehee, "The renaissance of dye-sensitized solar cells," *Nat. Photonics*, vol. 6, no. 3, pp. 162–169, Feb. 2012.

[8] International Energy Agency, "Technology Roadmap: Solar Photovoltaic Energy," 2010.

[9] European Photovoltaic Industry Association, "Global Market Outlook for Photovoltaics Until 2016," 2012.

[10] M. A. Green, K. Emery, Y. Hishikawa, and W. Warta, "Solar cell efficiency tables (version 36)," *Prog. Photovoltaics Res. Appl.*, vol. 18, no. 5, pp. 346–352, Jun. 2010.

[11] W. Guter, J. Schone, S. P. Philipps, M. Steiner, G. Siefer, A. Wekkeli, E. Welser, E. Oliva, A. W. Bett, and F. Dimroth, "Current-matched triple-junction solar cell reaching 41.1% conversion efficiency under concentrated sunlight," *Appl. Phys. Lett.*, vol. 94, no. 22, p. 223504, 2009.

[12] R. T. Ross and A. J. Nozik, "Efficiency of hot-carrier solar energy converters," *J. Appl. Phys.*, vol. 53, no. 5, p. 3813, 1982.

[13] A. Luque and A. Marti, "Increasing the Efficiency of Ideal Solar Cells by Photon Induced Transitions at Intermediate Levels," *Phys. Rev. Lett.*, vol. 78, no. 26, pp. 5014–5017, Jun. 1997.

[14] I. Fraunhofer, "World Record: 41.1 per cent efficiency reached for multi-junction solar cells," *Press release*, 2009.

[15] N. J. Ekins-Daukes, "Solar energy for heat and electricity : the potential for mitigating climate change," 2009.

[16] J. Olea, M. Toledano-Luque, D. Pastor, G. González-Díaz, and I. Mártil, "Titanium doped silicon layers with very high concentration," *J. Appl. Phys.*, vol. 104, no. 1, p. 016105, 2008.

[17] A. Luque, "Photovoltaics: Towards the intermediate band," *Nat. Photonics*, vol. 2, no. March, p. 166, Jan. 2011.

[18] A. Marti, E. Antolin, E. Canovas, N. Lopez, P. Linares, A. Luque, C. R. Stanley, and C. D. Farmer, "Elements of the design and analysis of quantum-dot intermediate band solar cells," *Thin Solid Films*, vol. 516, no. 20, pp. 6716–6722, Aug. 2008.

Chapter 2

Physics of Solar Cells

A comprehensive understanding of solar cells will require an understanding of the interaction between light and semiconductors. This chapter describes the photovoltaic energy conversion and sunlight which is the primary energy source and the solar cell itself. A brief discussion on solar irradiance is presented in the next section, and then a discussion on solar cell operation is presented. The IBSC concept is also discussed followed by a detailed look at QD IBSCs.

2.1 The Solar Resource

Sunlight is composed of radiation with a range of wavelengths that extends from the ultraviolet, through the visible to the infrared section of the electromagnetic spectrum. Solar irradiance is highest at the visible wavelengths, 300 – 800 nm. The solar irradiance reaching the Earth varies throughout the year due to its elliptical orbit around the sun and also because the Sun's emitted power is not constant. The solar spectrum may also vary according to the time of day, location and local atmospheric conditions. Hence, standard solar spectra have been defined by the photovoltaic research community and the American Society for Testing and Materials (ASTM) to

serve as a benchmark, allowing the comparison of solar cells from different manufacturers and laboratories. The spectra are based on air mass (AM); a parameter which gives an indication of how much of the atmosphere the spectrum has had to travel through. Simply put, air mass quantifies the solar spectrum's attenuation by the atmosphere. Air mass is defined by the secant of the zenith angle (Θ_z) at which a solar cell is operated. Figure 2.1 illustrates this.

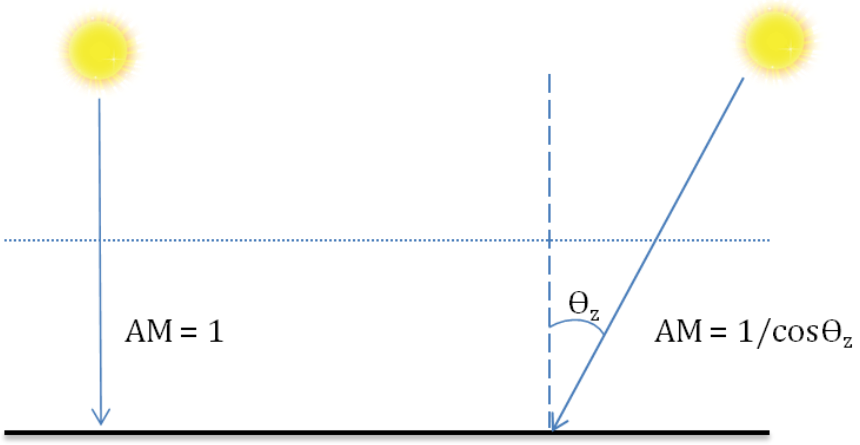

Figure 2.1 The schematic of Air Mass.

At a temperature of about 6000 K, the surface of the sun produces a power density of 6.2 *x* 10^7 Wm^{-2}, and this is reduced to 1353 Wm^{-2} just outside the Earth's atmosphere [1]. The standard for this extra-terrestrial spectrum is referred to as AM0 and it is the standard defined for space solar cell applications. The solar irradiation of AM0 corresponds to the radiation from a black-body at approximately 6000 K. Due to atmospheric effects such as Rayleigh scattering, scattering by dust and aerosols, and absorption by gases such as oxygen, ozone and water vapour, only 70% of the extra-terrestrial spectrum (AM0) reaches the Earth's surface. For terrestrial applications two standards (ASTM G173) are defined, AM1.5 Global for flat panel modules and AM1.5 Direct for solar concentrator applications. The air mass of 1.5 is given at a zenith angle of 48.2°. AM1.5 Global is defined as the total spectrum

incident on a horizontal plane including diffused components and albedo effects. As a result of atmospheric attenuation, the AM1.5 Global spectrum has a power density around 900 Wm^{-2}. However, for convenience, the standard value agreed upon for the power density of AM1.5 Global is 1000 Wm^{-2} at 25° C [1]. AM1.5 Direct is composed of only the direct normal component that contributes to the total global spectrum and its standard integrated power density is 900 Wm^{-2}. Figure 2.2 shows the standard solar spectra. In laboratory testing, a solar simulator is used to mimic AM0 and AM1.5 spectra.

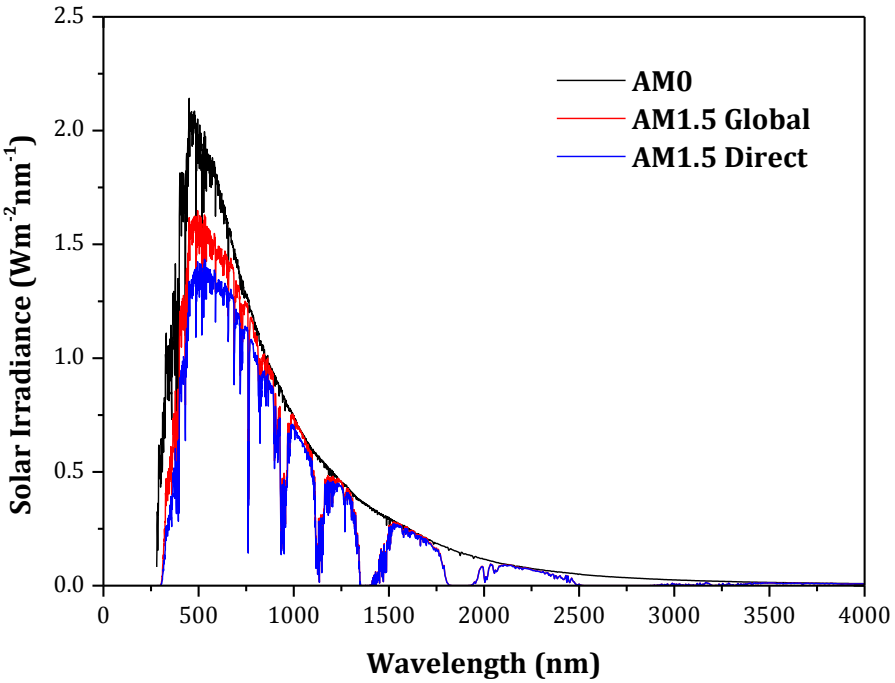

Figure 2.2 The extra-terrestrial spectrum (AM0) and the terrestrial spectra (AM1.5g and AM1.5d).

2.2 Basics of Semiconductors

When a semiconductor material is exposed to light, photons with energy (E_{ph}) greater than or equal to the bandgap (E_g) of the material will be absorbed. The absorbed energy breaks up covalent bonds and in the process creates electron-hole (E-H) pairs. The creation of these E-H pairs is the basis of photovoltaic energy production. Photons with energy less than the

bandgap pass through the semiconductor as though it was transparent. Photons with energy greater than the bandgap will dissipate the excess energy as heat in the lattice structure. Absorption is essentially the movement of electrons from the valence band (VB) into the conduction band (CB). If the electrons and holes created by absorption process remain within the semiconductor material long enough, they will recombine into bonds again. This process of recombination is enhanced by defects and impurities within or at the surface of the semiconductor.

High energy photons are absorbed at shallow depths of semiconductors and lower energy photons are absorbed at deeper depths of a semiconductor material. The generation rate (G) is the number of E-H pairs created per unit volume and it is given by

$$G(x) = \alpha N e^{-\alpha x} \qquad 2.1$$

where N is the photon flux (photons per unit area per second) at the surface, α is the absorption coefficient and x is the distance into the semiconductor material. The absorption coefficient is a measure of the depth at which photons of a particular energy are absorbed in a semiconductor material.

The most common semiconductor solar cell material is Si but solar cells are also fabricated from II-VI compounds such as CdTe and III-V compounds such as GaAs and GaInP. The choice of material is based on its optical characteristics, how well it matches the solar spectrum and cost of fabrication. Table 2.1 shows some of the elements used to produce solar cell materials.

II	III	IV	V	VI
	B	C	N	O
	Al	Si	P	S
Zn	Ga	Ge	As	Se
Cd	In	Sn	Sb	Te

Table 2.1 Groups II - VI of the periodic table of elements.

Figure 2.3 shows a plot of the absorption versus wavelength for Si and GaAs. Since Si is an indirect bandgap material, an extra particle (phonon) is involved in the absorption process. As a result, the probability of light absorption is less than in the case of direct bandgap materials. Hence Si has a lower absorption coefficient when compared to GaAs which is a direct bandgap material. This makes GaAs and other direct bandgap materials attractive for optical devices such as solar cells, photodiodes and lasers.

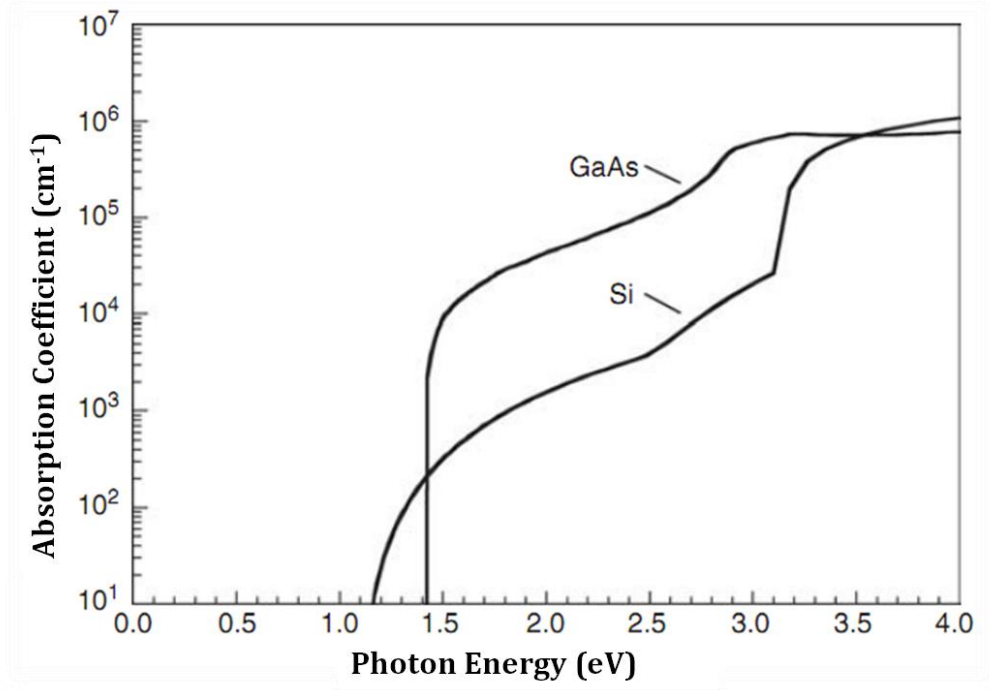

Figure 2.3 Absorption Coefficient as a function of photon energy for Si and GaAs at 300K [2].

2.3 P-N Junction

The *p*-*n* junction forms a basis for most solar cells and it is also integral to electronic devices like lasers, light emitting didoes (LEDs), photodiodes and transistors. A *p*-*n* junction is formed by the joining of an *n*-type and *p*-type crystalline semiconductor materials. A depletion region is formed at the boundary by the diffusion of electrons from the *n*-type into the *p*-type and holes from the *p*-type into the *n*-type. Therefore an electric field builds up across the junction that prohibits further diffusion across the junction.

Voltage applied to the junction can either reduce the electric field promoting a diffusion current flow (forward bias), or increase the electric field leading to a bigger barrier to current flow (reverse bias). The diode equation describing the flow of current through a *p*-*n* junction as a function of voltage was derived by Shockley [3]. In deriving this equation it was assumed that the junction is abrupt and there is no generation or recombination in the depletion region. Equation 2.2 gives the Shockley current which in relation to solar cells it is referred to as the dark current density, J_D as

$$J_D = J_0\left(e^{\frac{qV}{nkT}} - 1\right) \qquad 2.2$$

where J_0 is the dark saturation current (leakage current in the absent of light), V is the applied voltage, q is the charge of an electron, k is Boltzmann's constant, T is temperature and n is the ideality factor. An ideal diode has an ideality factor, n = 1. This ideality factor is based on the assumption that all recombination is radiative and occurs in the bulk of the device. In practice, recombination does occur in other parts of the device and this recombination could be non-radiative. In this case, the ideality factor typically lies between 1 and 2. Figure 2.4 summarises the absorption and loss mechanisms in a *p*-*n* junction.

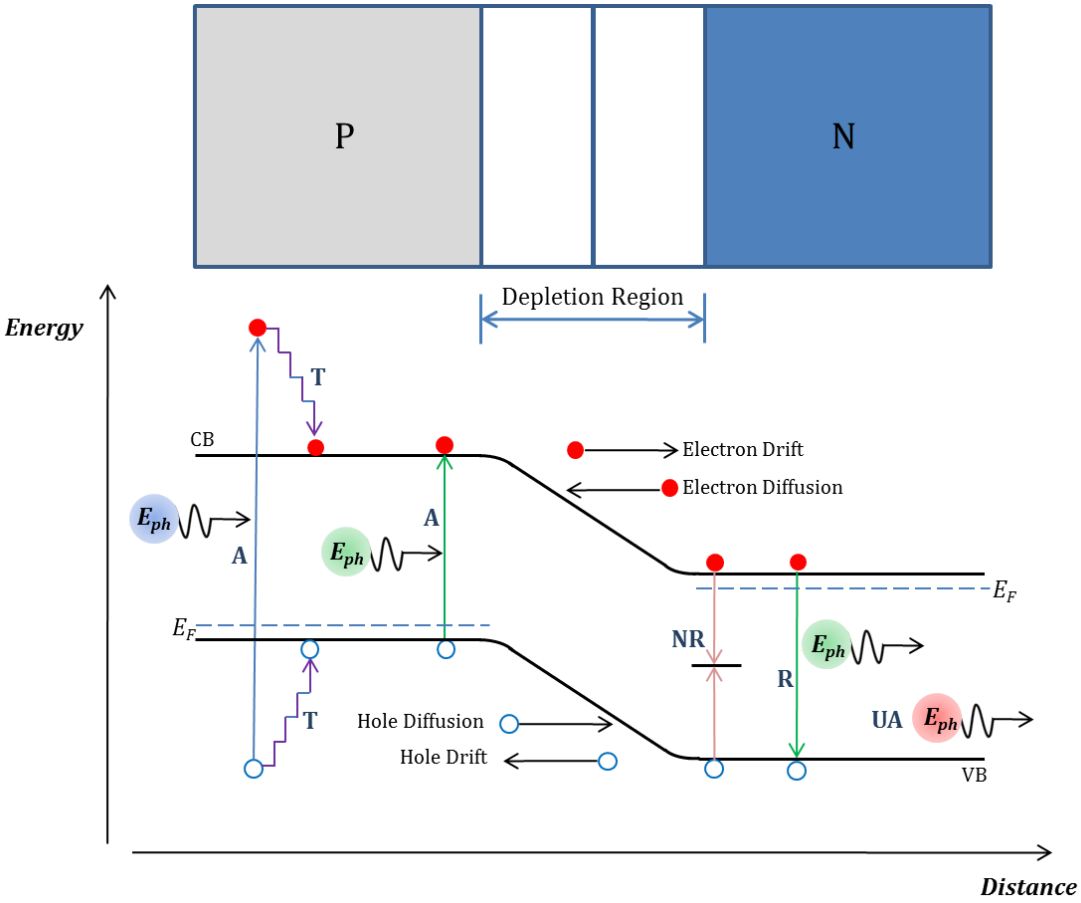

Figure 2.4 P-N Junction: Absorption (A), Thermalisation (T), Non-radiative recombination (NR), Radiative recombination (R), Unabsorbed radiation (UA). The Fermi levels are denoted by E_F.

2.4 Solar Cell Operation

2.4.1 Ideal Solar Cells

In a *p-n* junction solar cell, the basic steps of operation can be identified as follows: the generation of charge carriers (E-H pairs), the collection of the carriers driven by the built-in electric field in the depletion region, the generation of voltage across the solar cell and the dissipation of power in an external load. Light-generated current is produced by the generation and collection of light-generated carriers. Collection probability is enhanced if charge carriers are generated within a diffusion length of the *p-n* junction. Equation 2.3 gives the light-generated current as

$$J_L = q \int_0^W G(x) CP(x)\, dx \qquad 2.3$$

where J_L is the light-generated current density, W is the thickness of the device and $CP(x)$ is the collection probability at a depth of x into the material.

In order to generate power, a solar cell must generate both a voltage and a current. The photovoltaic effect is the process by which a voltage is created in the solar cell. Collection of light-generated carriers causes electrons to move to the *n*-type and holes to move to the *p*-type. This drift current is the light-generated current J_L and it flows in the opposite direction to the diffusion diode current. Under short-circuit current conditions; the voltage across the solar cell is zero because there is no build-up of charge due to the carriers exiting the device as light-generated current. If a load is placed across the solar cell, there is a build-up of electrons in the *n*-type and holes in the *p*-type. This separation of charge causes a decrease in the net electric field across the *p*-*n* junction resulting in an increase in the diffusion diode current. A new equilibrium is achieved in which a voltage exists across the junction and a current also flows through the solar cell. This current is equal to the difference between the diffusion diode current (i.e. the dark current) and the light-generated current, and can be written as

$$J_D = J_0 \left(e^{\frac{qV}{nkT}} - 1 \right) - J_L \qquad 2.4$$

The current density – voltage behaviour of a solar cell, as shown in Figure (a) is essentially the superposition of the solar cell's dark current with the light-generated current [4]. The *J*-*V* curve is moved down into the fourth quadrant where power can be extracted. Figure 2.5(b) shows the equivalent circuit of a solar cell, which is a current source in parallel with a rectifying diode. The current source represents the photo-generation of current and the diode represents the radiative recombination within the cell. The ideality factor and the dark saturation current can be increased to account for non-radiative recombination in a non-ideal solar cell. Under open-circuit conditions, the

diffusion diode current and the light-generated current cancel each other out and hence no current flows.

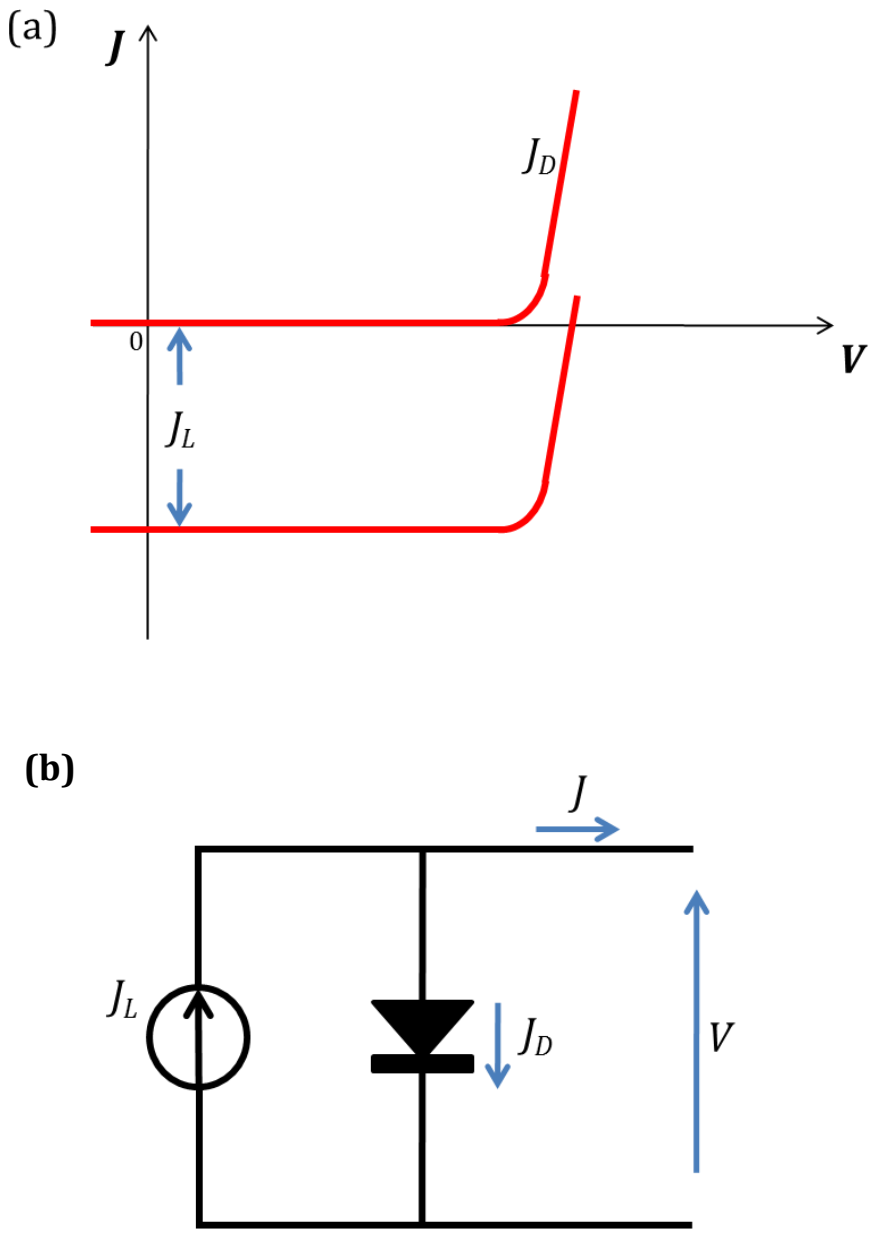

Figure 2.5 (a) *J-V* curve of a solar cell and (b) the equivalent circuit of a solar cell.

2.4.2 Losses in Solar Cells

Real solar cells have non-ideal characteristics due to losses that occur in the solar cell. Figure 2.6 shows a diagram that classifies the losses into optical and electrical components. Sub-bandgap losses result in a reduction in output current and lattice thermalisation results in a reduction in output voltage. These two optical losses alone account for more than 50% of the losses in a single bandgap solar cell [5]. Recombination losses also lead to a reduction in output voltage.

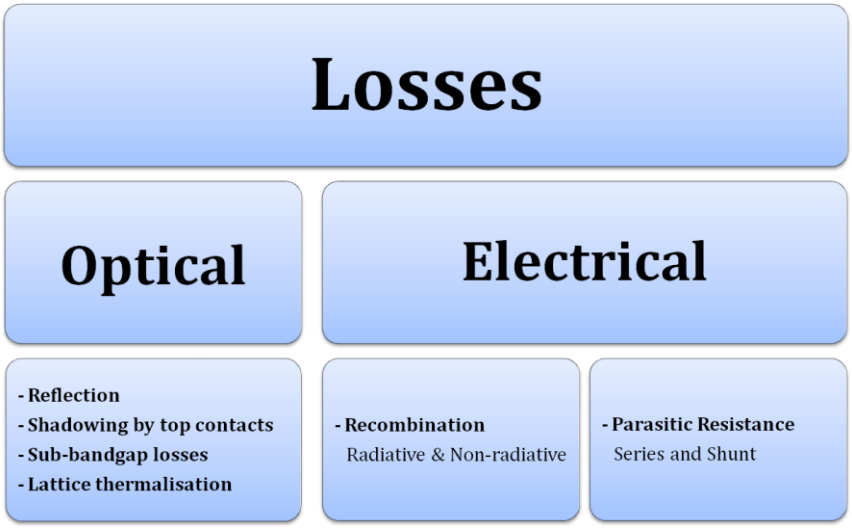

Figure 2.6 Losses in a solar cell

2.4.3 Solar Cell Performance Parameters

Quantum Efficiency

Quantum efficiency (QE) is the ratio of the number of carriers collected by a solar cell to the number of incident photons at a given wavelength. If all photons of a particular wavelength are absorbed and carriers collected, then the QE at that wavelength is 1. This is true for an ideal solar cell at all wavelengths. QE depends on the absorbing properties of the solar cell material and the carrier transport processes within it. For real solar cell structures, the QE might be reduced by surface recombination at short

wavelengths and bulk recombination at long wavelengths. The QE for an ideal and a practical solar cell is shown in Figure 2.7.

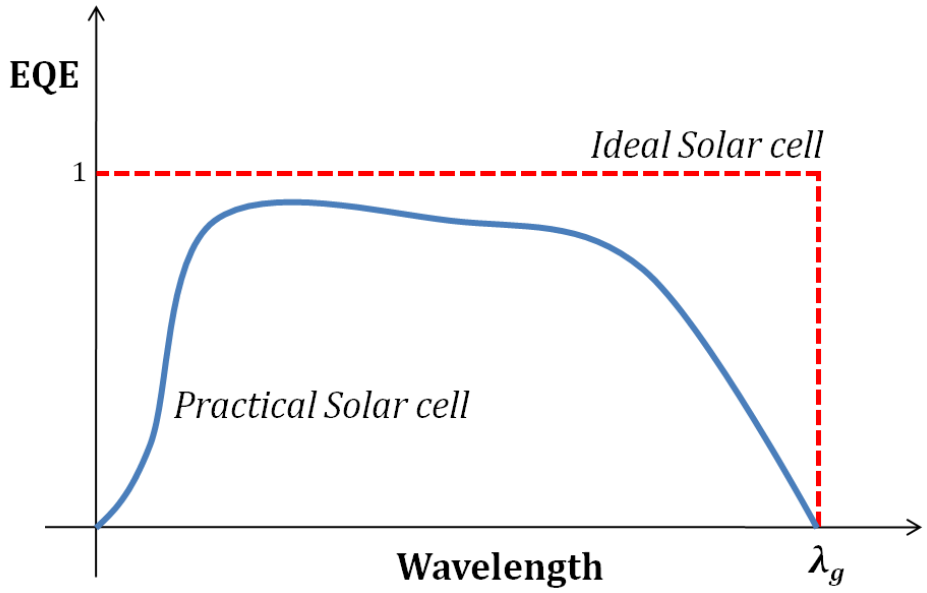

Figure 2.7 Quantum Efficiency of an ideal solar cell and a practical solar cell.

The external quantum efficiency (EQE) of a solar cell includes the effects of transmission and reflection. The internal quantum efficiency (IQE) can be determined from the external quantum efficiency by measuring the transmission and reflection.

J-V Curve

The *J-V* curve of a solar cell is, perhaps the most important piece of information in characterising solar cells. The short-circuit current density (J_{SC}), the open-circuit voltage (V_{OC}), the fill factor (*FF*) and the efficiency (η) can be determined from the *J-V* curve. It is the convention to invert the current density axis of the *J-V* curve, bringing it into the first quadrant as shown in Figure 2.8.

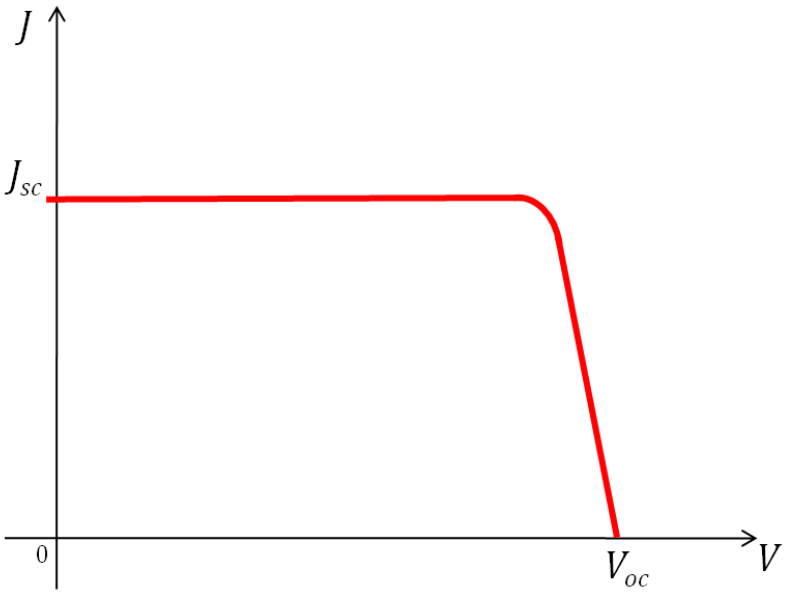

Figure 2.8 *J-V* curve of a solar cell, showing the short-circuit current density (J_{SC}) and the open-circuit voltage (V_{OC}).

Short-Circuit Current

The short-circuit current density J_{SC} is the maximum current that can be drawn from a solar cell and it is achieved at zero voltage. For an ideal solar cell, $J_{SC} = J_L$. The short-circuit current density J_{SC} depends on the QE and the intensity and spectrum of the incident light. This dependency is shown as

$$J_L = q \int_0^{\infty} F(\lambda) QE(\lambda)\, d\lambda \qquad 2.5$$

where $F(\lambda)$ is the photon flux ($m^{-2}s^{-1}nm^{-1}$)

Open-Circuit Voltage

The open-circuit voltage (V_{OC}) is the maximum voltage available from a solar cell and it is achieved at zero current. V_{OC} depends on J_{SC} and J_0. J_{SC} typically has small variation whereas J_0 may vary by orders of magnitude. Since J_0 depends on recombination, V_{OC} can be seen as a measure of the recombination in the solar cell. The V_{OC} is given by

$$V_{OC} = \frac{nkT}{q} \ln\left(\frac{J_{SC}}{J_O} + 1\right) \quad \textbf{2.6}$$

Fill Factor

The fill factor (*FF*) is the ratio of the maximum power that can be extracted from a solar cell to the product of the J_{SC} and V_{OC} as shown by

$$FF = \frac{J_m V_m}{J_{SC} V_{OC}} \quad \textbf{2.7}$$

where J_m and V_m refer to the current density and the voltage at the maximum power point.

The fill factor is a measure of the *p-n* junction quality and series resistance of a solar cell. The maximum power point is also an important parameter and it is graphically represented in Figure 2.9. The maximum power density (P_m) that can be extracted from a solar cell can then be calculated by

$$P_m = J_{SC} V_{OC}\, FF \quad \textbf{2.8}$$

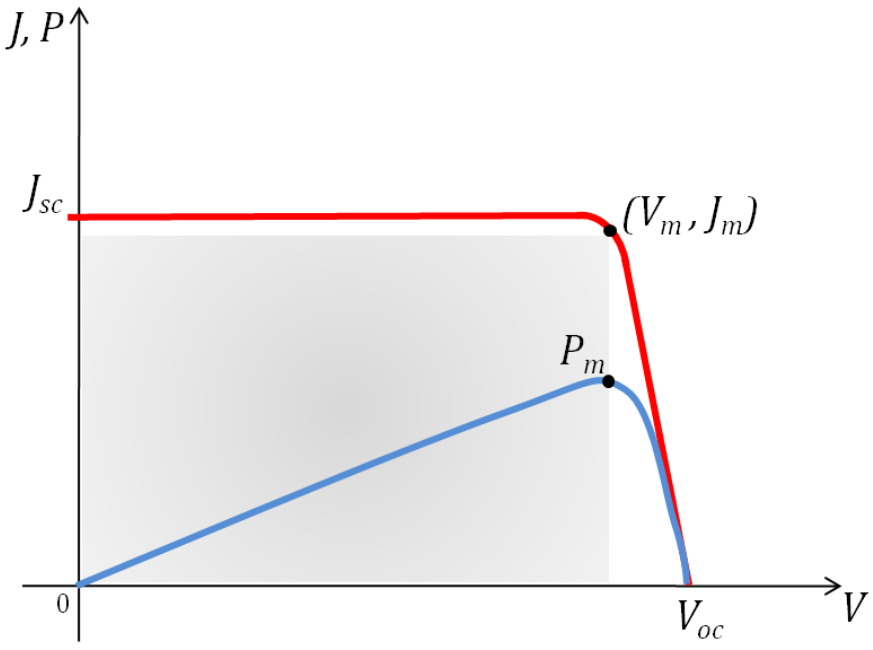

Figure 2.9 *J-V* curve showing the maximum power point.

Efficiency

Efficiency (η) is defined as the ratio of energy output from a solar cell to the input incident solar energy. It is perhaps the most commonly used parameter for a solar cell. Measurements of efficiency for terrestrial cells are usually done with the AM1.5 Global solar spectrum at 25^{o} C. The efficiency can be described as

$$\eta = \frac{J_{SC} V_{OC} FF}{P_{IN}} \qquad 2.9$$

where P_{IN} is the input power density which is 1000 Wm^{-2} for the AM1.5 Global spectrum.

The best laboratory efficiency value for a crystalline GaAs solar cell under global AM1.5 is 28% [6]. Solar cells fabricated with low bandgap semiconductor materials will absorb more low energy photons leading to an increase in J_{SC}. However, this is will result in an increase in the dark current due to a rise in the dark saturation current, as demonstrated by

$$J_O \propto e^{-\frac{E_g}{kT}} \qquad 2.10$$

The increase in dark current means a decrease in V_{OC}. On the other hand, solar cells with a high bandgap will have a lower J_{SC} due to lower energy photons not being absorbed. The V_{OC} will however be greater due to a lower dark current value. Since the product of J_{SC} and V_{OC} are related to the efficiency of a solar cell, it follows that there will be an optimum bandgap at which efficiency is highest. The limiting efficiency of singe bandgap cells as a function of bandgap for the AM1.5 Global spectrum is shown in Figure 2.10 with some semiconductor materials highlighted. The maximum efficiency occurs at about 1.37 eV which is close to the bandgap of GaAs (1.43 eV).

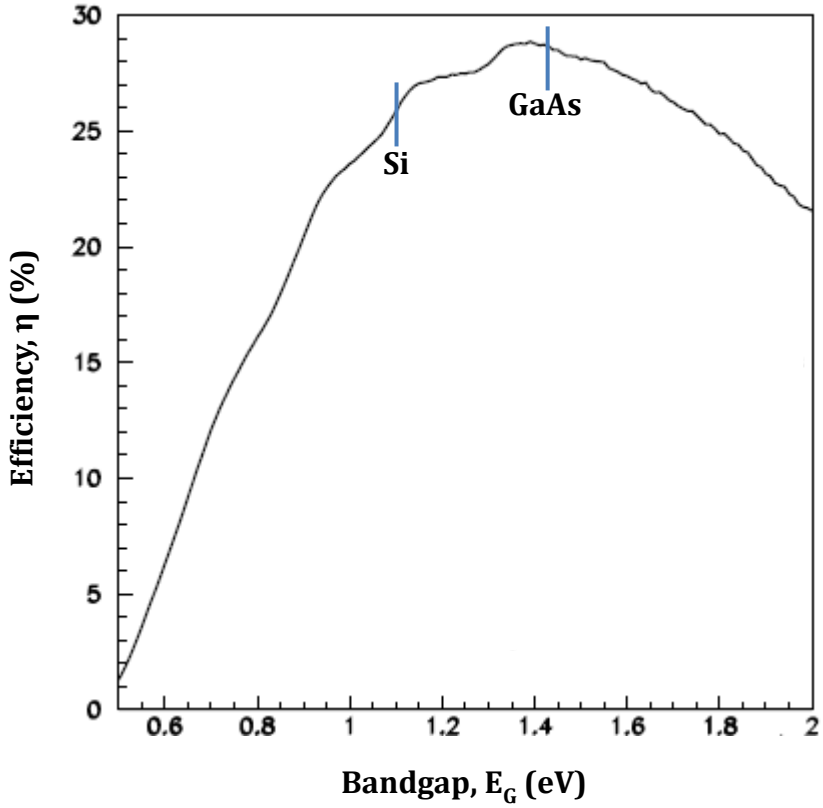

Figure 2.10 Limiting efficiency for single bandgap solar cells as a function of bandgap under the AM1.5 global spectrum (adapted from [7]).

2.4.4 Resistive Effects

Solar cells typically have parasitic resistances that reduce their efficiency by dissipating power in these resistances. These resistances are the series and shunt resistances. Figure 2.11 includes these resistances to present a more complete and realistic diagram of the solar cell equivalent circuit.

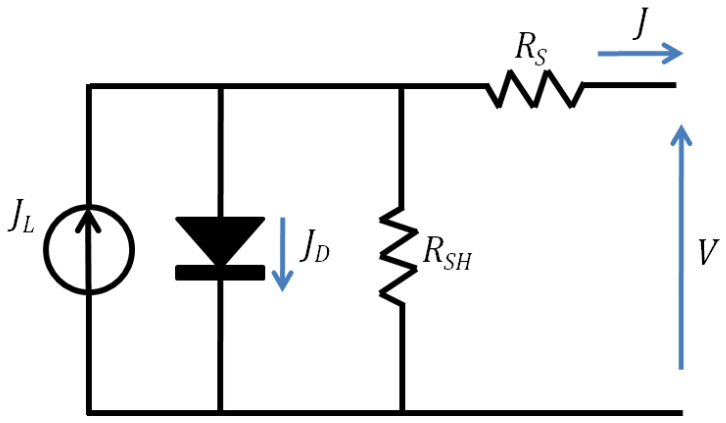

Figure 2.11 Solar cell equivalent circuit showing parasitic series and shunt resistances.

The **series resistance** (R_S) is caused by the bulk resistance of the semiconductor material, the resistance of the metallic contacts and the contact resistance between the metallic contacts and the semiconductor. Ideally, the R_S should be zero. The immediate effect of the R_S is to reduce the fill factor and hence the efficiency. For very large R_S, J_{SC} is reduced. R_S does not affect V_{OC} since at V_{OC} there is no current through the solar cell. To estimate the R_S, the slope of the *J-V* curve near to the V_{OC} can be calculated. The effects of the series resistance are shown in Figure 2.12.

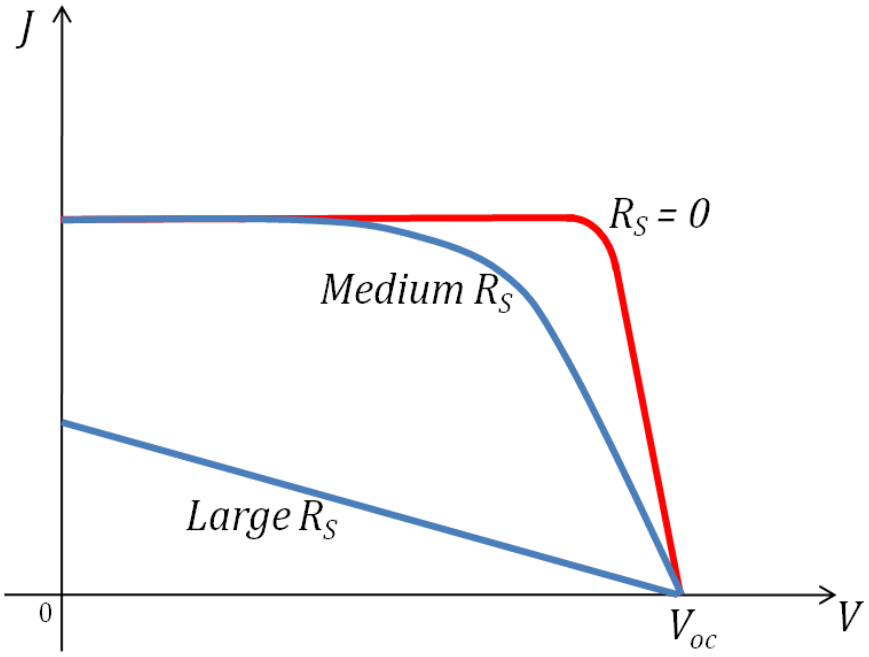

Figure 2.12 Effects of series resistance on the *J-V* characteristics

The **shunt resistance** (R_{SH}) is mostly caused by fabrication defects such as the partial shorting of the *p-n* junction particularly near the edge of the solar cell. A shunt resistance will create an alternative path for the light-generated current J_L leading to a reduction in the current through the solar cell and hence a drop in voltage across the solar cell. R_{SH} does not affect J_{SC} because at J_{SC} current does not flow through the R_{SH}. The effects of R_{SH} are shown in Figure 2.13.

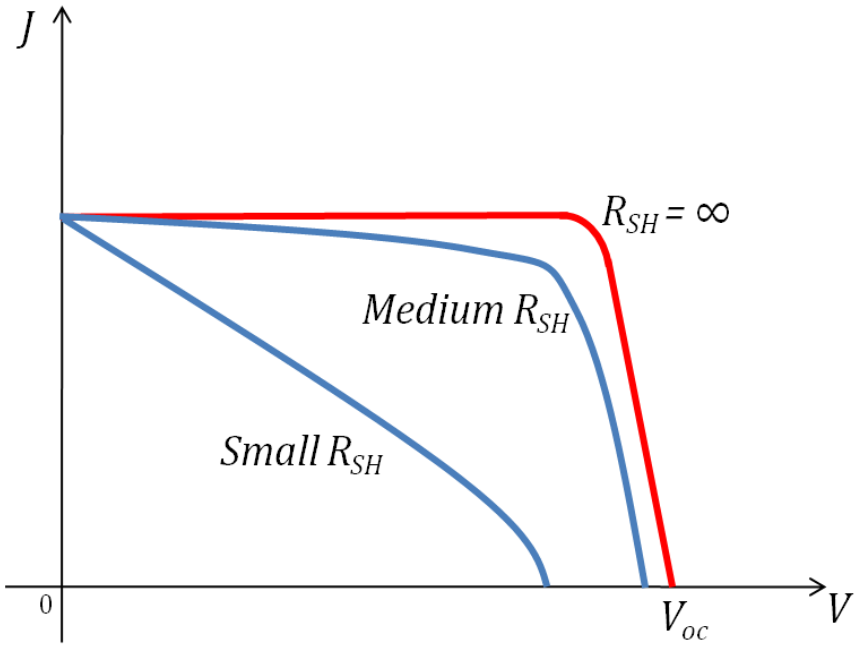

Figure 2.13 Effects of shunt resistance of the *J-V* characteristics

When both parasitic resistances are present in a solar cell, the *J-V* curve is given by

$$J = J_L - J_0\left(e^{\frac{qV}{nkT}} - 1\right) - \frac{V + JR_SA}{R_{SH}} \qquad 2.11$$

where A is the area of the solar cell.

2.4.5 Effects of Temperature and Light Intensity

The efficiency of a solar cell at any particular time is affected by its operating temperature. The temperature at which a cell operates might be affected by the concentrating of the incident sunlight and other factors. An increase in temperature will result in a decrease in bandgap, leading to slight increase in J_{SC}. However, this is accompanied by a significant drop in V_{OC} and hence the fill factor and efficiency are reduced.

The intensity of incident sunlight on a solar cell affects its parameters. Light intensity is delineated in suns, where 1 sun refers to the standard

illumination of AM1.5 and 10 suns to a tenfold concentration of the spectrum. J_{SC} is linearly dependent on light intensity whereas V_{OC} is logarithmically dependent on J_{SC} such that

$$V_{OC} = \frac{nkT}{q} \ln\left(\frac{XJ_{SC}}{J_O} + 1\right) \qquad 2.12$$

where X is the concentration of sunlight. Therefore, an increase in efficiency is attained under concentration.

Efficiency gains by concentration will still be reduced by parasitic resistance losses and also by the increased operating temperature of the solar cell. In addition to the potential for higher efficiencies, concentrator solar cells could also lower cost due to the small device area required.

2.4.6 Real Solar Cell Structures

As already mentioned, real solar cells tend to stray from the ideal, partly due to optical losses and recombination caused by defects in the semiconductor crystalline structure. There are also physical and inherent constraints that limit the performance of a solar cell. Taking into account the non-radiative recombination and parasitic resistances, a more accurate expression for the current produced by real solar cells is given by Equation 2.13.

$$J = J_L - J_{01}\left(e^{\frac{qV}{kT}} - 1\right) - J_{02}\left(e^{\frac{qV}{2kT}} - 1\right) - \frac{V + JR_SA}{R_{SH}} \qquad 2.13$$

where J_{01} and J_{02} are the dark saturation currents for the radiative and non-radiative currents respectively.

The corresponding equivalent circuit is shown in Figure 2.14.

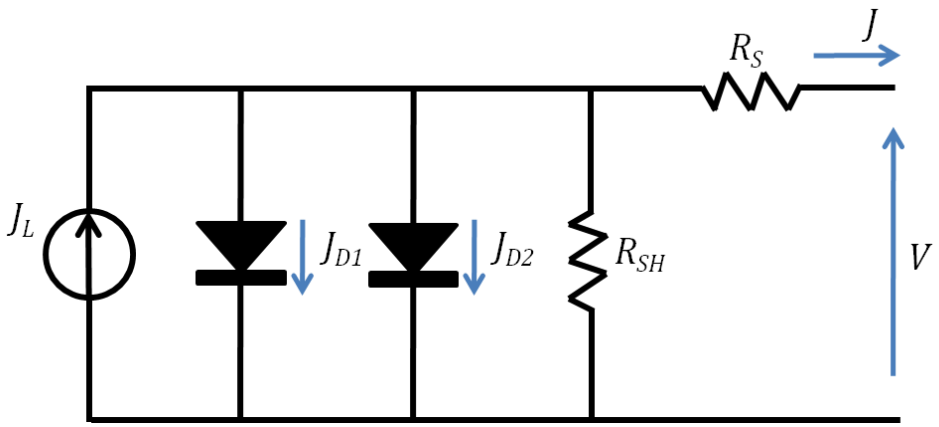

Figure 2.14 The equivalent circuit for a practical solar cell. (J_{D1} and J_{D2} represent the dark currents).

Specific features can be engineered into a solar cell structure to alleviate optical and recombination losses in order to improve the performance. A few of these techniques are highlighted below.

• **Window Layer**: Minority carriers created near the front surface of a solar cell have a high probability of being lost to surface recombination. To prevent this from occurring, a thin layer of high bandgap material placed at the front surface is used to create a barrier, referred to as the window layer. The window bounces back minority carriers towards the depletion region where they can be collected and contribute to the solar cell's power output. In most III-V solar cell, AlGaAs or AlInP is used as the window layer. A capping layer is placed on top of the window to protect it from oxidising and it is also highly doped to provide a low resistance contact to the front of the cell.

• **Back surface fields:** The back surface field is similar to the window layer, but it is employed at the base of the solar cell close to the bottom contact. It reflects minority carriers away from the back surface of the solar cell towards the depletion region. The back surface field is implemented by either a very highly doped layer or by a high bandgap material such as AlGaAs or GaInP.

• **Front Contacts:** Metallic contacts are needed on the top and bottom of a solar cell to carry the light-generated current to the external circuit. The bottom contact is completely metallised and so it is not a problem. The top metallic contact, however, has to collect current from all areas of the surface and at the same time allow light through to the solar cell. A good top contact design will optimise current collection while reducing series resistance and cell shadowing. It has been shown that tapered busbar and fingers present lower losses as compared to busbars with constant width [8]. Fabricated by photolithographic processes, the front metallic contacts are made of a combination of alloys that may consist of Au, Zn, Ti, Ni, Ge and other metals.

• **Anti-reflection coating (ARC):** To combat reflection at the surface of a solar cell, an ARC can be applied. After the deposition of the top metallic contacts, the capping layer is etched away until the window layer is reach. Then a dielectric layer can be deposited as the ARC. Silicon nitride (Si_3N_4) and magnesium fluoride (MgF_2) are usually used for this purpose.

2.5 Multi-Junction Solar Cells

Multi-junction solar cells (MJSC) also referred to as tandem cells, are currently the most efficient of all solar cells. Originally developed for space applications, MJSCs have now found acceptance for terrestrial applications when used with concentrators to make them cost effective [9]. They owe their high efficiency to a design that allows the solar cell to selectively absorb in different parts of the solar spectrum. A MJSC consists of *p-n* junction solar cells that are connected in series, with the largest bandgap solar cell placed at the top and the smallest at the bottom. As shown by Figure 2.15(b), the individual cells are connected by a tunnel junction.

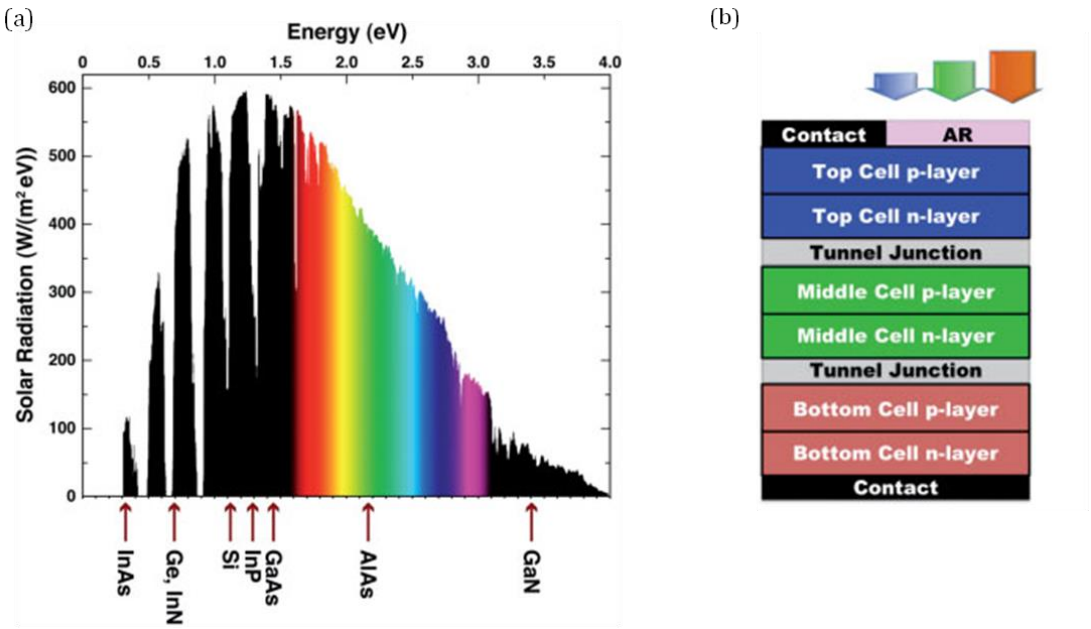

Figure 2.15 Bandgaps of semiconductors shown on the AM1.5 spectrum (a) and a schematic of the multi-junction solar cell structure (b) [10].

The effective allocation and distribution of bandgaps in the MJSC is vital in achieving high efficiencies. A wide range of bandgaps is available by alloying different III-V compound semiconductors (shown in Figure 2.15(a)). Since the lowest current-producing cell in the MJSC will set the current for the whole cell, it is important to ensure excess current is not wasted. The race is on to find a 1.0-eV bandgap material that can be place in the current limiting region of a MJSC such as InGaP/GaAs/Ge to enhance the short-current and the efficiency. Detailed balance calculations have shown that spectral tuning of MJSC by quantum dots could lead to an increase in efficiency [11].

2.6 Intermediate Band Solar Cells

The intermediate band solar cell (IBSC) can exceed the Shockley-Quiesser efficiency limit of 30% [12] for a single junction solar cell by a more effective use of the solar spectrum. As already mentioned, one of the major losses in single bandgap solar cell are the sub-bandgap photon losses. Given that a considerable amount of the solar spectrum is in the low energy infrared

region, it is necessary to harness these low energy photons if the efficiencies of solar cells are to be improved. Figure 2.16 illustrates the IBSC concept. The intermediate band (IB) within the semiconductor bandgap enables the absorption of sub-bandgap photons. In addition to the usual absorption of photons by electron transitions between the VB and the CB, there is a two photon absorption process with transitions between the VB and the IB, and then between the IB and the CB. A quasi Fermi level will be associated with each bands (E_{FV}, E_{FV}, E_{FI}) due to the fact that carrier relaxation between bands is slower than within bands [13].

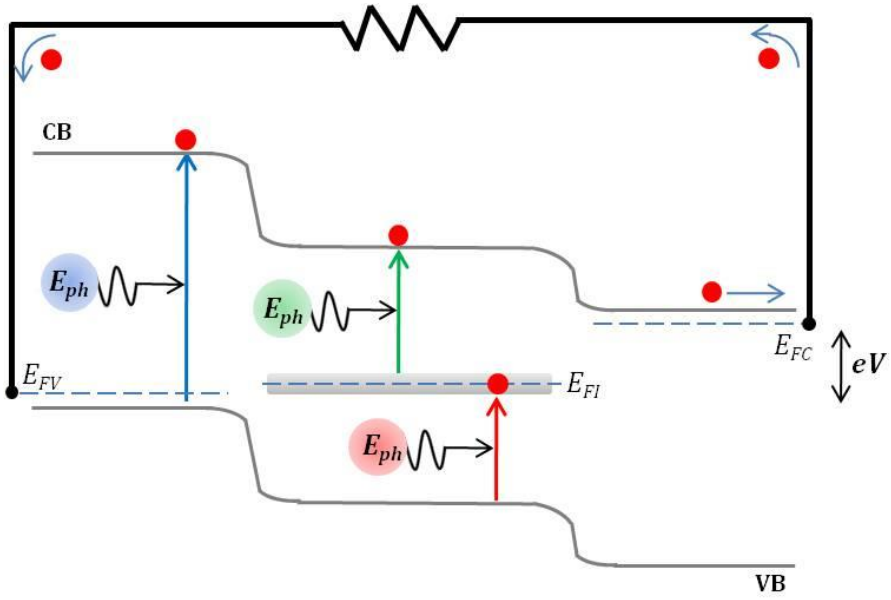

Figure 2.16 The absorption of photons in an intermediate band solar cell.

In order to attain an increase in efficiency by the IBSC concept, the photocurrent should be increased by the additional photon absorptions, without a reduction in the output voltage. Individual quasi Fermi levels for the energy bands are essential for this to happen. The voltage extracted from the IBSC is the difference between the quasi-Fermi levels for electrons (E_{FC}) in the CB and holes (E_{FV}) in the VB, divided by the electron charge.

Figure 2.17 shows the calculated limiting efficiency as a function of the lowest bandgap for an IBSC and a two-terminal tandem solar cell by Luque *et al*. The full concentration blackbody spectrum limiting efficiency of the IBSC is found to be 63 %, which is greater than that of a two junction tandem cell and the single bandgap cell. From Figure 2.17 it is clear that the optimum bandgaps for the implementation of an IBSC are E_{CV} = 1.93 eV, E_{VI} =1.23 eV and E_{IC} =0.7 eV. These calculations assume that non-radiative recombination is suppressed, there are no ohmic losses, the cell is at 300 K and the illumination is from an isotropic gas of photons at 6000 K.

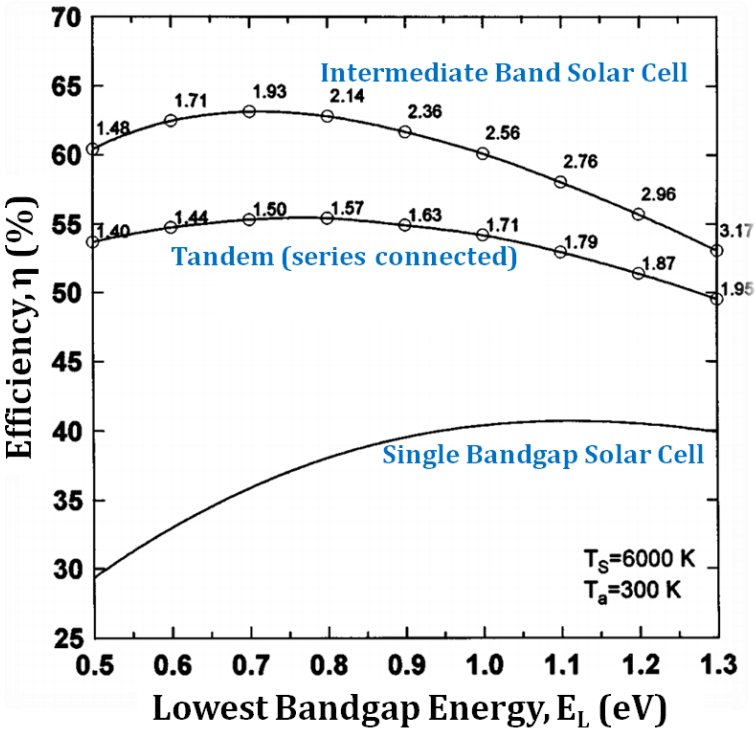

Figure 2.17 Limiting efficiency for an intermediate band solar cells and a double junction tandem solar cell as a function of the lowest bandgap energy. The limiting efficiency of a single bandgap solar cell is also included for comparison. The numbers on the plot represent the highest bandgap in the intermediate band and tandem cells (adapted from [14]).

The equivalent circuit for an IBSC is shown in Figure 2.18. The two additional current sources represent the absorption of sub-bandgap photons and the two additional diodes represent the new paths for carrier recombination. Modelling suggests that at high illumination concentrations, IBSCs will have a

higher efficiency than single bandgap cells because at high current densities, recombination from the CB to the VB (J_{CV}) is more dominant than the recombination through the IB (J_{CI} and J_{IV}) [15].

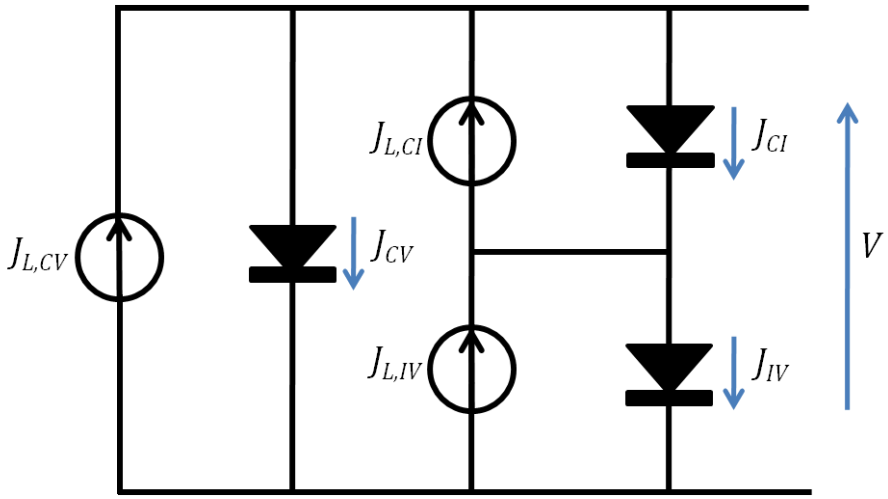

Figure 2.18 Equivalent circuit of the intermediate band solar cell

As already mentioned, both the MJSC and the IBSC are third generation approaches that aim to increase efficiency by absorbing more of the solar spectrum. The equivalent circuit of the MJSC will consist of individual of cells (current source and diode) connected in series. It is interesting to note that the equivalent circuit of the IBSC also consists of individual cells; two connected in series and then connected in parallel with a third.

2.7 Quantum Dot Intermediate Band Solar Cells

A number of IB materials have been proposed for the implementation of the IBSC. Among these are $Ti_xGa_{1-x}P$ [16], transition meta-doped chalcopyrite-type semiconductors [17] and Cr-doped II-VI compounds [18]. However, to date the most promising path to the implementation of the IBSC has been by the use of QDs. QDs are nano-sized clusters of semiconductor material that confine carriers in all three dimensions. The QDs are usually embedded in a

barrier material of higher bandgap and placed in the intrinsic region of a *p-i-n* solar cell structure. In QD IBSCs, the intermediate states are created by the confined electron levels within the potential well formed as a result of the conduction band offset between the barrier and the dots. This is illustrated in Figure 2.19.

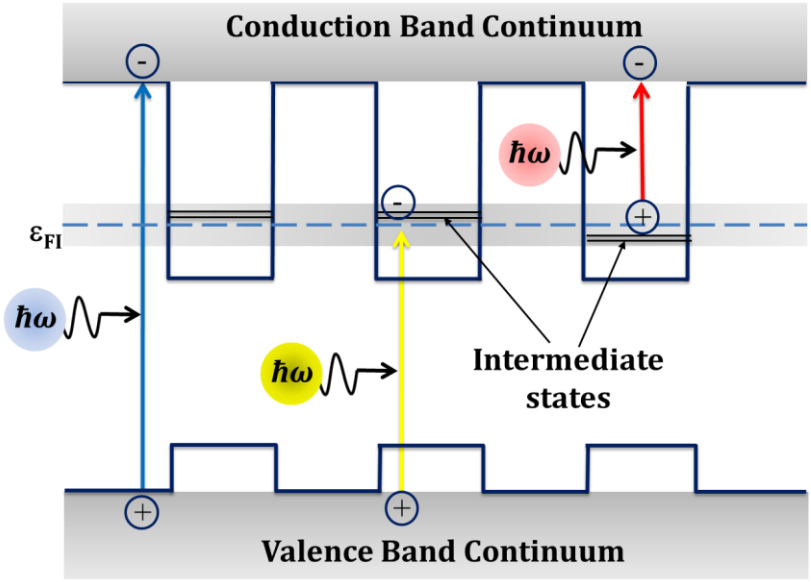

Figure 2.19 Simplified bandgap diagram of a QD IBSC

QDs are preferred, as opposed to other low-dimensional structures such as quantum well or wires because they have a delta-function-like density of states due to the complete size quantization of electronic levels in the QDs [19]. These discrete density of states can generate a zero density of states between the IB and the CB, supporting the formation of individual quasi-Fermi levels [20]. The key operating principles of QD IBSC have been demonstrated by material systems such as In(Ga)As/GaAs [21]–[25], InAs/GaNAs [26] and GaSb/GaAs [27]. But there are challenges in realising IBSCs by these material systems. Figure 2.20 shows a simple diagram of an InAs/GaAs QD IBSC.

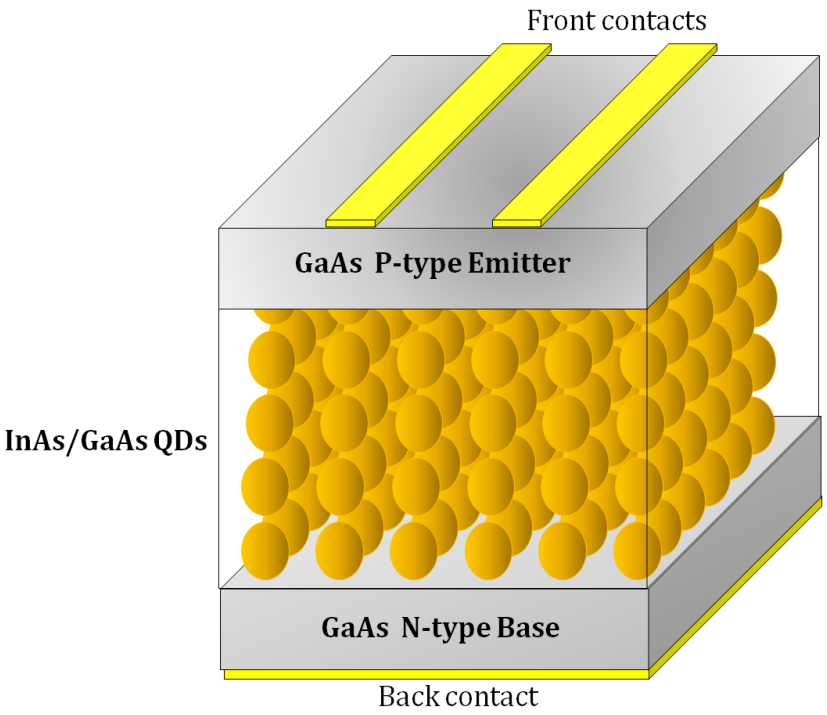

Figure 2.20 Quantum dot intermediate band solar cell structure.

2.7.1 Criteria for Implementation

The IBSC aims to increase the current of solar cells while at the same time maintaining the output voltage, hence producing a cell with efficiency greater that the Shockley-Quiesser efficiency limit. The conditions necessary for the realisation of a good QD IBSC has been outlined in a number of publications [20] [21]. The major ones are discussed below.

- **High QD Density with narrow size distribution**

A highly dense array of QD is required not only to increase the absorption of sub-bandgap photons but also to ensure the overlap of wavefunctions of the confined states. This wavefunction overlap leads to the formation of a band of states as opposed to localised energy levels. The size uniformity of dots affects cell performance. Excessive non-uniformities in the QD size will result in a collection of multilevels instead of an IB [28]. A broad QD size dispersion also localises the electron wavefunction, decreasing the radiative

recombination rates. Marti *et al.* give a rough estimate of the tolerance limit of size dispersion to be about 10% [29].

- **Three distinct quasi-Fermi levels**

Apart from the quasi-Fermi levels for the VB and CB, a third quasi-Fermi level that describes the carrier population in the IB is required. This implies that the IB will be electrically isolated but optically coupled to the VB and the CB. This is perhaps the most defining characteristic of an IB material. Any electrical coupling between the IB and the VB or CB will cause the cell to cease to act properly as an IBSC, leading to a decrease in open-circuit voltage and efficiency. Luminescence emissions from an IB material is expected to have three peaks corresponding to the three energy transitions, which serve as a signature for an IB material [30].

- **Partial filling of IB**

In order to achieve strong absorption in transitions from the IB to the CB, it is necessary that the IB is partially filled. A partially filled IB allows for empty states that can receive electrons from the VB and electron-filled states that can excite electrons to the CB. To achieve this partial filling, it has been proposed that the barrier material of the QD system be n-doped, providing the some electrons for the IB. Delta (δ) doping within the inter-dot layers has also been proposed as the means to achieve this goal [15].

- **Photon Selectivity**

The IBSC has three electronic transitions that are associated with it. All three electronic transitions, (VB to CB, VB to IB and IB to CB) have absorption coefficients associated with each; α_{CV}, α_{VI} and α_{IC} respectively. The proposed ideal model for the IBSC [14], assumes that there is no absorption coefficient overlap. That means that for a given photon energy, only one of the three electronic transitions is possible. However, this is not the case in practice. Figure 2.21 illustrates these absorption coefficient configurations.

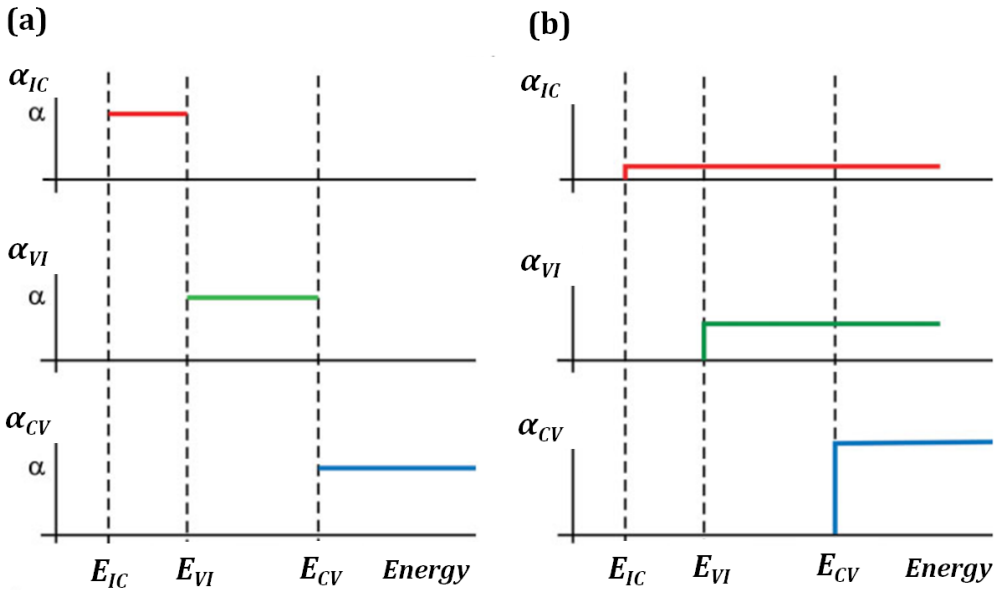

Figure 2.21 Absorption coefficients for IBSCs in the case of no overlap (a) and overlap (b) [13].

An overlap of absorption coefficients in an IBSC will lead to inefficient absorption of photons, with photons of energy greater than E_{CV} being absorbed by the VB-IB transition instead of the VB-CB transition. In this case, photons generated by radiative recombination can be reabsorbed by a band other than the one that created them. Cuadra *et al*. have shown that the effects of absorption coefficient overlap can be minimised if $\alpha_{CV} >> \alpha_{VI}$ [31].

2.7.2 Proof of Intermediate Band Solar Cell Concept with Quantum Dots

There is already ample experimental proof of sub-bandgap photocurrent in IBSCs. Figure 2.22 shows the QE measurements for a single junction GaAs cell and an InAs QD IBSC. It can be seen that the reference cell absorbs only above the bandgap of GaAs while the IBSC absorbs photons below the GaAs bandgap.

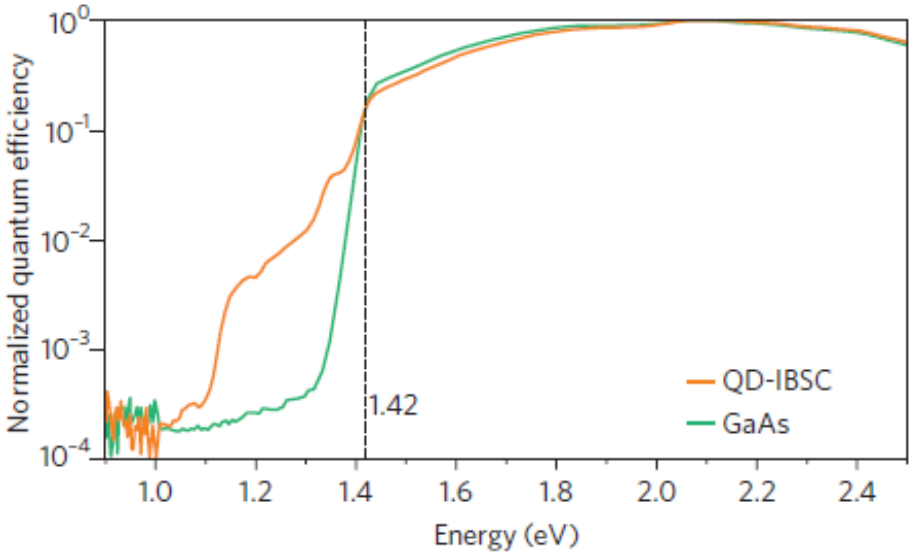

Figure 2.22 Comparison of the normalised quantum efficiency of a GaAs solar cell and a QD IBSC [32].

In current InAs/GaAs QD IBSCs, it has been shown that the sub-bandgap photon absorption is mainly due to the photon excitation of electrons from the VB to the IB. The IB-CB transition occurs by thermal escape and tunneling mechanisms [33]. This is not compatible with the IBSC model and hence cannot lead to the high efficiencies predicted. A second sub-bandgap photon transition is required to provide the energy necessary to preserve the output voltage. Two sub-bandgap photon transitions (VB-IB and IB-CB) in an IBSC at a temperature of 6K have been demonstrated [34]. The low temperature is used to in order to minimise thermal escape.

While two-photon absorption was first only observed at low temperatures for most QD IBSC, a recent study has presented evidence of two-photon absorption at room temperature for an InAs/GaNAs QD IBSC.[35] These encouraging results were achieved by the direct Si-doping of the QDs in the QDSC structure instead of δ-doping the inter-dot layer.

2.7.3 InAs/GaAs QD Solar Cells

In many ways, the InAs/ GaAs QD material system has been adopted as a test subject to prove the operating principles of QD IBSC. The InAs/GaAs QD material system have been used not because it has the optimal band alignments for the best operation of an intermediate band solar cell, but simply because it is relatively well understood. With that being said, lessons learnt with this material system can be applied to others.

Despite the lack of ideal bandgaps in these solar cells, calculations show that high concentration of illumination results in efficiencies higher than that of a single junction solar cell. This is because recombination increases slower through the IB than through the CB - VB transition [15]. The position of the intermediate band will depend on the size, shape and material combination of the quantum dots. The width of the IB depends on the size distribution of the QD and also on the distance between layers of dots [28]. The photoluminescence for these solar cell structures often show two narrowly separated peaks; one corresponding to VB-CB transition and the other the VB-IB transition. The absence of a third peak, as is expected from the luminescence signature of intermediate band materials shows that the second sub-bandgap transition (IB-CB) is not taking place optically.

The wetting layer under the QDs in an InAs/GaAs material system, results in the appearance of an energy level below the CB, which forms a continuum with it and shrinks the effective bandgap of the solar cell. Since the effective mass of holes is greater than that of electrons, confined levels in the VB are tightly spaced, forming a quasi-continuum of states [28]. This VB offset in addition to the wetting layer, limits the total bandgap of the InAs/GaAs solar cell to about 1.3eV. Another concern then becomes the energy separation between the IB and the CB, which in this case is ~ 0.3eV [36]. This low energy gap makes it easy for electrons to thermalise into the CB instead of being promoted there by photons. The energy diagram for this material system is shown in Figure 2.23.

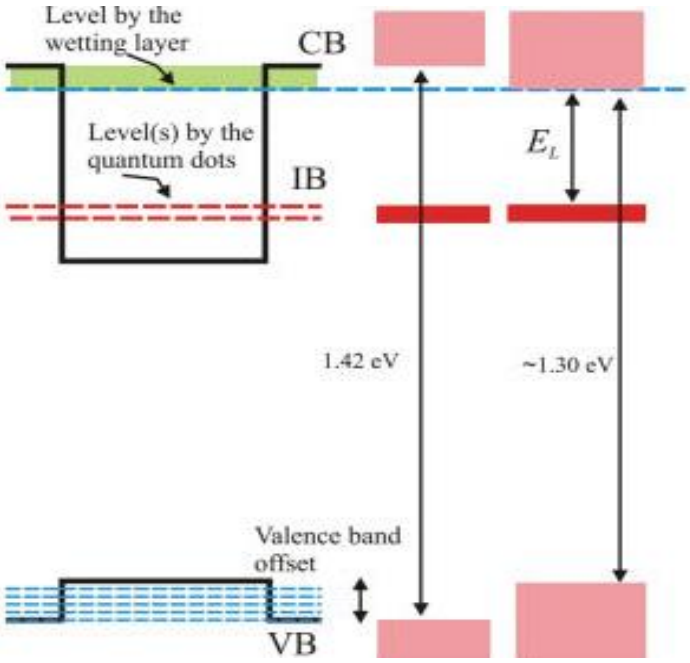

Figure 2.23 An illustration of the reduction in the bandgap of an InAs/GaAs QD IBSC due to the wetting layer and the valence band offset. [13]

2.7.4 Challenges: Current and Voltage

The discussion above on InAs/GaAs QD solar cells has brought to bear some of the challenges of implementing a QD IBSC. As already mentioned, the IBSC seeks to increase current of the cell while preserving the output voltage. Therefore, a detailed examination of the challenges of QD IBSCs is presented below along with proposed solutions in terms of the current and the voltage.

- **Current**

QD IBSCs fabricated until now have performed far from the ideal in term of the current generated. The contribution from the QDs to the photocurrent has not been significant due to relatively low QD densities. QD densities of 5 x 10^{10}cm^{-2} per layer have been achieved for InAs/GaAs QDs. In a QD IBSC, this relatively small density is not enough to significantly enhance the photogenerated current. The total contribution to short-circuit current by QDs is very small (typically 1%) [13]. Therefore, for significant absorption of sub-bandgap photons, it is necessary to increase the volume of QDs within the QD IB solar cells by increasing the number of dots per layer or by using

multilayers of QDs. The lattice mismatch necessary for the formation of QDs also introduces strain, such that the stacking of QD layers increases the accumulated stress within the QD layers, resulting in dislocations and nonradiative recombination centres. It has been shown by Marti *et al.* that dislocations within the QD region can propagate into the emitter of the solar cell [37]. High density InAs QDs per layer can be grown at a low growth temperature and a high growth rate. However, this results in the coalescence of neighbouring dots and a broad distribution of QD sizes.

Strain compensation techniques have proved promising as a way to reduce accumulated stress and allow for the growth of a high number of stacked QD layers. GaP [38] and GaNAs [39] have been used as strain compensation in previous work. As an added bonus strain compensation by GaP has been shown to increase the thermal stability of solar cells by increasing the thermal activation energy [40].

Another challenge for QD IBSCs is the short carrier lifetime in the QDs. The carrier lifetime in the QDs is generally shorter than in bulk materials and this presents a problem to all minority carriers that have to traverse the QD region in order to be collected either in the base or emitter [40]. In a type I band structure such as InAs/GaAs QD system the electrons and holes are confined in QDs, hence the radiative recombination lifetime is shorter than in a bulk material due to the significant spatial overlap of electrons and hole wavefunctions. Type I band alignment has a radiative recombination lifetime of approximately 1 ns [41]. In the type II alignment, electrons are confined in the QDs and the holes are located in the surrounding material. As a result there is small overlap between electron and hole wavefunctions and hence a longer radiative lifetime is achieved. A radiative recombination lifetime of 65 ns has been achieved with InAs QDs capped by $GaAs_{0.78}Sb_{0.22}$ [42]. This feature will also enhance the collection of carriers and hence the short-circuit current.

- **Voltage**

In order for an IB solar cell to lead to an increase in efficiency, the increase in short-circuit current must not be accompanied by a reduction in the open-circuit voltage. Unfortunately, published results for QD IBSCs to date show a reduction in open-circuit voltage mainly due to the wetting layer and valence band offsets.

It appears that for QD material systems with a typical type-I band structure, the VB offset might always be an issue. It has been shown that the VB offset can be mitigated by a negligible band offset QD system [43] or avoided altogether by a type-II band structure QD system [27]. As already mentioned, a type-II QD system also has the added benefit of a relatively long radiative lifetime due to the spatial separation of confined electrons and holes [44].

In order to encourage the all-important second sub-bandgap absorption in a QD IBSC and to avoid the thermalisation of carriers from the IB into the CB, it is advantageous to have a larger energy separation between the IB and the CB. This could be achieved by embedding the QDs in a high bandgap material such as AlGaAs [45]. Since AlGaAs is an indirect bandgap material, better results might be achieved with a direct and high bandgap material such as InGaP.

2.7.5 Optimal Material Triad Systems

Optimal bandgaps of for IB solar cells have previously been calculated to be E_{CV} = 1.93eV, E_{IV} = 1.23eV and E_{IC} = 0.7eV for a full concentration blackbody radiation [14]. However, recent limiting efficiency calculations have shown that under the terrestrial AM1.5 spectrum, a broader range of bandgaps with $E_{IC} \sim$ 0.57eV can lead to efficiencies higher than 40% under 1 sun and higher than 50% under moderate concentration [46]. This is encouraging because it shows that there is a larger design space for IBSC than previously thought. Figure 2.24 shows the efficiency contours of an IBSC under 1 sun AM1.5.

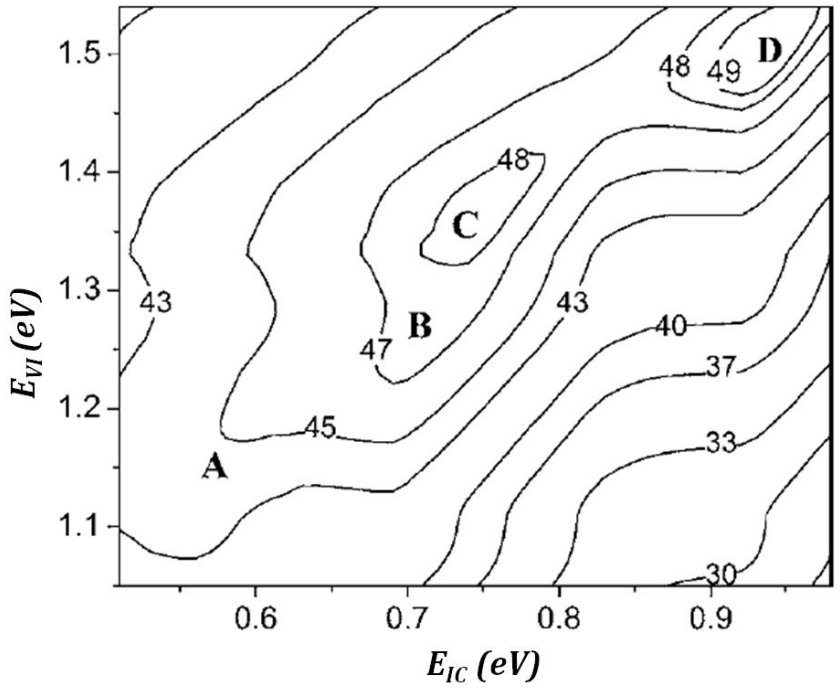

Figure 2.24 Efficiency contours for an IBSC under 1 sun AM1.5 spectrum [46].

As already mentioned, the VB offset leads to the reduction of the effective bandgap of the QD solar cell and so a negligible VB offset is desirable as a design rule. Using this as a criteria, along with considerations for optimal bandgaps a number of material systems have been proposed [47]. Dahal *et al.* also identified a number of direct bandgap III-V binary and ternary compounds with optimal bandgaps and negligible VB offsets, the most promising of which is the InAsP/AlInAs QD solar cell grown on GaAs, with a predicted efficiency of 48% [48].

The InAs/GaAsSb QD material system is another system that could be engineered to exhibit a low VB offset. Previous work with this system has shown it to have good optical performance [49]. Liu et al. have shown that an InAs/GaAs QD system with a GaAsSb capping layer becomes type-II at a Sb composition above 14% [50]. It has further been confirmed that the transition from type-I energy band structure to a type-II is achieved for Sb composition between 13% and 15% [50], [51]. This means that InAs QDs in a $GaAs_{0.86}$ $Sb_{0.14}$ barrier material will have minimal or no VB offset. It has also

been shown that doping the barrier of the QDs can ensure that more carriers are kept in the QDs due to an enhanced Coulomb attraction which leads to an increase in thermal activation energy at room temperature [52]. A low VB offset could also be achieved by a novel material system such as InP/GaAsP [47].

The growth of GaAsSb is a challenge because it is a III-V-V compound. Group V elements are more volatile compared to Group III elements and hence the mole fractions are not only determined by the growth fluxes but also by the growth temperatures due to their temperature dependant sticking coefficients. However despite these challenges, it has been possible to grow GaAsSb by precise control of flux ratio and temperature [50]. It has been shown that improvements in composition control of III-V-V compounds can be achieved by a digital growth method [53].

In conclusion, it is worth mentioning that one of the best published results so far for a QD IBSC is an InAs/GaAs QD solar cell with an efficiency of 18.3% [21]. This is still below the reference GaAs solar cell with which it was compared. The realization of QD IBSC has come a long way over recent years; however there still remain some significant improvements to be made.

Bibliography

[1] J. Neslon, *The Physics of Solar Cells*. Imperial College Press, 2003.

[2] A. Luque and S. Hegedus, *Handbook of Photovoltaic Science and Engineering*. John Wiley and Sons, 2011.

[3] W. Shockley, "The theory of pn junctions in semiconductors and pn junction transistors," *Bell Syst. Tech. J*, 1949.

[4] F. A. Lindholm, J. G. Fossum, and E. L. Burgess, "Application of the superposition principle to solar-cell analysis," *IEEE Trans. Electron Devices*, vol. 26, no. 3, pp. 165–171, Mar. 1979.

[5] L. C. Hirst and N. J. Ekins-Daukes, "Fundamental losses in solar cells," *Prog. Photovoltaics Res. Appl.*, vol. 19, no. 3, pp. 286–293, 2010.

[6] M. A. Green, K. Emery, Y. Hishikawa, W. Warta, and E. D. Dunlop, "Solar cell efficiency tables (version 41)," no. version 41, pp. 1–11, 2013.

[7] N. J. Ekins-Daukes, "An investigation into the efficiency of strained and strain-balanced quantum well solar cells," Imperial College of Science, Technology and Medicine, 1999.

[8] S. R. Wenham, M. A. Green, M. E. Watt, and R. Corkish, *Applied Photovoltaics*. STYLUS PUB LLC, 2007.

[9] R. McConnell and V. Fthenakis, "Concentrated Photovoltaics," in in *Third Generation Photovoltaics*, V. Fthenakis, Ed. InTech, 2012.

[10] G. F. Brown and J. Wu, "Third generation photovoltaics," *Laser Photonics Rev.*, vol. 3, no. 4, pp. 394–405, Jul. 2009.

[11] R. P. Raffaelle, S. Sinharoy, J. Andersen, D. M. Wilt, and S. G. Bailey, "Multi-junction solar cell spectral tuning with quantum dots," in *Photovoltaic Energy Conversion, Conference Record of the 2006 IEEE 4th World Conference on*, 2006, vol. 1, pp. 162–166.

[12] W. Shockley and H. J. Queisser, "Detailed Balance Limit of Efficiency of p-n Junction Solar Cells," *J. Appl. Phys.*, vol. 32, no. 3, p. 510, 1961.

[13] A. Luque and A. Marti, "The intermediate band solar cell: progress toward the realization of an attractive concept.," *Adv. Mater.*, vol. 22, no. 2, pp. 160–174, Jan. 2010.

[14] A. Luque and A. Marti, "Increasing the Efficiency of Ideal Solar Cells by Photon Induced Transitions at Intermediate Levels," *Phys. Rev. Lett.*, vol. 78, no. 26, pp. 5014–5017, Jun. 1997.

[15] A. Marti, E. Antolin, E. Canovas, N. Lopez, P. Linares, A. Luque, C. R. Stanley, and C. D. Farmer, "Elements of the design and analysis of quantum-dot intermediate band solar cells," *Thin Solid Films*, vol. 516, no. 20, pp. 6716–6722, Aug. 2008.

[16] P. Palacios, J. Fernandez, K. Sanchez, J. Conesa, and P. Wahnon, "First-principles investigation of isolated band formation in half-metallic Ti(x)Ga(1−x)P (x=0.3125–0.25)," *Phys. Rev. B*, vol. 73, no. 8, pp. 1–8, Feb. 2006.

[17] P. Palacios, K. Sanchez, J. C. Conesa, and P. Wahnon, "First principles calculation of isolated intermediate bands formation in a transition metal-doped chalcopyrite-type semiconductor," *Phys. status solidi*, vol. 203, no. 6, pp. 1395–1401, May 2006.

[18] C. Tablero, "Optoelectronic properties of Cr-substituted II–VI semiconductors," *Comput. Mater. Sci.*, vol. 37, no. 4, pp. 483–490, Oct. 2006.

[19] A. Zrenner, "A close look on single quantum dots," *J. Chem. Phys.*, vol. 112, no. 18, p. 7790, 2000.

[20] A. Marti, L. Cuadra, and A. Luque, "Partial filling of a quantum dot intermediate band for solar cells," *IEEE Trans. Electron Devices*, vol. 48, no. 10, pp. 2394–2399, 2001.

[21] S. A. Blokhin, A. V. Sakharov, A. M. Nadtochy, A. S. Pauysov, M. V. Maximov, N. N. Ledentsov, A. R. Kovsh, S. S. Mikhrin, V. M. Lantratov, S. A. Mintairov, N. A. Kaluzhniy, and M. Z. Shvarts, "AlGaAs/GaAs photovoltaic cells with an array of InGaAs QDs," *Semiconductors*, vol. 43, no. 4, pp. 514–518, Apr. 2009.

[22] C. G. Bailey, D. V. Forbes, R. P. Raffaelle, and S. M. Hubbard, "Near 1 V open circuit voltage InAs/GaAs quantum dot solar cells," *Appl. Phys. Lett.*, vol. 98, no. 16, p. 163105, 2011.

[23] D. Guimard, R. Morihara, D. Bordel, K. Tanabe, Y. Wakayama, M. Nishioka, and Y. Arakawa, "Fabrication of InAs/GaAs quantum dot solar cells with enhanced photocurrent and without degradation of open circuit voltage," *Appl. Phys. Lett.*, vol. 96, no. 20, p. 203507, 2010.

[24] K. A. Sablon, J. W. Little, V. Mitin, A. Sergeev, and N. Vagidov, "Strong Enhancement of Solar Cell Efficiency Due to Quantum Dots," *Nano Lett.*, vol. 11, no. 6, pp. 2311–2317, 2011.

[25] D. Zhou, G. Sharma, S. F. Thomassen, T. W. Reenaas, and B. O. Fimland, "Optimization towards high density quantum dots for intermediate

band solar cells grown by molecular beam epitaxy," *Appl. Phys. Lett.*, vol. 96, no. 6, pp. 061913–3, 2010.

[26] R. Oshima, A. Takata, and Y. Okada, "Strain-compensated InAs/GaNAs quantum dots for use in high-efficiency solar cells," *Appl. Phys. Lett.*, vol. 93, no. 8, p. 083111, 2008.

[27] R. B. Laghumavarapu, A. Moscho, A. Khoshakhlagh, M. El-Emawy, L. F. Lester, and D. L. Huffaker, "GaSb/GaAs type II quantum dot solar cells for enhanced infrared spectral response," *Appl. Phys. Lett.*, vol. 90, no. 17, p. 173125, 2007.

[28] S. Tomić, T. S. Jones, and N. M. Harrison, "Absorption characteristics of a quantum dot array induced intermediate band: Implications for solar cell design," *Appl. Phys. Lett.*, vol. 93, no. 26, p. 263105, 2008.

[29] A. Marti, L. Cuadra, and A. Luque, "Design constraints of the quantum-dot intermediate band solar cell," *Phys. E Low-dimensional Syst. Nanostructures*, vol. 14, no. 1–2, pp. 150–157, 2002.

[30] N. J. Ekins-Daukes, C. B. Honsberg, and M. Yamaguchi, "Signature of intermediate band materials from luminescence measurements," in *31st IEEE Photovoltaic Specialists Conference, 2005. Conference*, 2005, pp. 49–54.

[31] L. Cuadra, A. Marti, and A. Luque, "Influence of the Overlap Between the Absorption Coefficients on the Efficiency of the Intermediate Band Solar Cell," *IEEE Trans. Electron Devices*, vol. 51, no. 6, pp. 1002–1007, Jun. 2004.

[32] A. Luque, A. Martí, and C. Stanley, "Understanding intermediate-band solar cells," *Nat. Photonics*, no. Focus| Progress Article, pp. 1–7, 2012.

[33] A. Luque, A. Martí, E. Antolín, P. G. Linares, I. Tobías, and I. Ramiro, "Radiative thermal escape in intermediate band solar cells," *AIP Adv.*, vol. 1, no. 2, p. 022125, 2011.

[34] E. Antolin, A. Marti, C. R. Stanley, C. D. Farmer, E. Cánovas, N. Lopez, P. G. Linares, and A. Luque, "Low temperature characterization of the photocurrent produced by two-photon transitions in a quantum dot intermediate band solar cell," *Thin Solid Films*, vol. 516, no. 20, pp. 6919 – 6923, 2008.

[35] Y. Okada, T. Morioka, K. Yoshida, R. Oshima, Y. Shoji, T. Inoue, and T. Kita, "Increase in photocurrent by optical transitions via intermediate quantum states in direct-doped InAs/GaNAs strain-compensated quantum dot solar cell," *J. Appl. Phys.*, vol. 109, no. 2, p. 024301, 2011.

[36] A. Marti, N. Lopez, E. Antolin, E. Canovas, C. Stanley, C. D. Farmer, L. Cuadra, and A. Luque, "Novel semiconductor solar cell structures: The quantum dot intermediate band solar cell," in *Symposium F on Thin Film and Nanostructured Materials for Photovoltaics*, 2006, vol. 511–512, pp. 638–644.

[37] A. Marti, N. Lopez, E. Antolin, E. Canovas, A. Luque, C. R. Stanley, C. D. Farmer, and P. Diaz, "Emitter degradation in quantum dot intermediate band solar cells," *Appl. Phys. Lett.*, vol. 90, no. 23, p. 233510, 2007.

[38] S. M. Hubbard, C. D. Cress, C. G. Bailey, R. P. Raffaelle, S. G. Bailey, and D. M. Wilt, "Effect of strain compensation on quantum dot enhanced GaAs solar cells," *Appl. Phys. Lett.*, vol. 92, no. 12, p. 123512, 2008.

[39] R. Oshima, T. Hashimoto, H. Shigekawa, and Y. Okada, "Multiple stacking of self-assembled InAs quantum dots embedded by GaNAs strain compensating layers," *J. Appl. Phys.*, vol. 100, no. 8, p. 083110, 2006.

[40] D. Alonso-Alvarez, A. G. Taboada, J. M. Ripalda, B. Alen, Y. Gonzalez, L. Gonzalez, J. M. Garcia, F. Briones, A. Marti, A. Luque, A. M. Sanchez, and S. I. Molina, "Carrier recombination effects in strain compensated quantum dot stacks embedded in solar cells," *Appl. Phys. Lett.*, vol. 93, no. 12, p. 123114, 2008.

[41] H. Yu, S. Lycett, C. Roberts, and R. Murray, "Time resolved study of self-assembled InAs quantum dots," *Appl. Phys. Lett.*, vol. 69, no. 26, p. 4087, 1996.

[42] Y. D. Jang, T. J. Badcock, D. J. Mowbray, M. S. Skolnick, J. Park, D. Lee, H. Y. Liu, M. J. Steer, and M. Hopkinson, "Carrier lifetimes in type-II InAs quantum dots capped with a GaAsSb strain reducing layer," *Appl. Phys. Lett.*, vol. 92, no. 25, p. 251905, 2008.

[43] M. Y. Levy, C. B. Honsberg, A. Marti, and A. Luque, "Quantum dot intermediate band solar cell material systems with negligible valence band offsets," in *31st IEEE Photovoltaics Specialist Conference*, 2005, pp. 90–93.

[44] C.-K. Sun, G. Wang, J. E. Bowers, B. Brar, H.-R. Blank, H. Kroemer, and M. H. Pilkuhn, "Optical investigations of the dynamic behavior of GaSb/GaAs quantum dots," *Appl. Phys. Lett.*, vol. 68, no. 11, p. 1543, 1996.

[45] P. G. Linares, A. Marti, E. Antolin, and A. Luque, "III-V compound semiconductor screening for implementing quantum dot intermediate band solar cells," *J. Appl. Phys.*, vol. 109, no. 1, p. 014313, 2011.

[46] S. P. Bremner, M. Y. Levy, and C. B. Honsberg, "Limiting efficiency of an intermediate band solar cell under a terrestrial spectrum," *Appl. Phys. Lett.*, vol. 92, no. 17, p. 171110, 2008.

[47] M. Y. Levy and C. B. Honsberg, "Nanostructured Absorbers for Multiple Transition Solar Cells," *IEEE Trans. Electron Devices*, vol. 55, no. 3, pp. 706–711, Mar. 2008.

[48] S. N. Dahal, S. P. Bremner, and C. B. Honsberg, "Identification of candidate material systems for quantum dot solar cells including the effect of strain," *Prog. Photovoltaics Res. Appl.*, vol. 18, no. 4, pp. 233–239, 2010.

[49] K. Akahane, N. Yamamoto, S. Gozu, and N. Ohtani, "Strong photoluminescence and laser operation of InAs quantum dots covered by a GaAsSb strain-reducing layer," *Phys. E Low-dimensional Syst. Nanostructures*, vol. 26, no. 1–4, pp. 395–399, Feb. 2005.

[50] H. Y. Liu, M. J. Steer, T. J. Badcock, D. J. Mowbray, M. S. Skolnick, P. Navaretti, K. M. Groom, M. Hopkinson, and R. a. Hogg, "Long-wavelength light emission and lasing from InAs/GaAs quantum dots covered by a GaAsSb strain-reducing layer," *Appl. Phys. Lett.*, vol. 86, no. 14, p. 143108, 2005.

[51] K. Y. Ban, W. Hong, S. P. Bremner, S. N. Dahal, H. McFelea, and C. B. Honsberg, "Controllability of the subband occupation of InAs quantum dots on a delta-doped GaAsSb barrier," *J. Appl. Phys.*, vol. 109, no. 1, p. 014312, 2011.

[52] Y. D. Jang, J. Park, D. Lee, D. J. Mowbray, M. S. Skolnick, H. Y. Liu, M. Hopkinson, and R. A. Hogg, "Enhanced room-temperature quantum-dot effects in modulation-doped InAs/GaAs quantum dots," *Appl. Phys. Lett.*, vol. 95, no. 2009, p. 171902, 2009.

[53] E. Hall, H. Kroemer, and L. A. Coldren, "Improved composition control of digitally grown AlAsSb lattice-matched to InP," *J. Cryst. Growth*, vol. 203, no. 3, pp. 447–449, Jun. 1999.

Chapter 3

Experimental Methods

This research project involves epitaxial growth, device processing and characterisation. The solar cell epitaxial structures reported in this thesis were designed and grown at UCL, using the Veeco Gen930 solid-source molecular beam epitaxy facility at the Department of Electronic and Electrical Engineering. Device fabrication facilities at the London Centre for Nanotechnology (LCN) were used to develop test solar cell devices. The solar cells discussed in Chapter 4 were processed and partly characterised at Sharp Europe Laboratories. All other solar cells discussed in this thesis were processed at the Research Centre for Advanced Science and Technology (RCAST), The University of Tokyo. Measurements of light-IV, dark-IV and external quantum efficiency were also conducted at RCAST. Photoluminescence (PL) measurements were performed at UCL.

This chapter outlines the experimental work associated with the project. It begins with a discussion on epitaxial growth by molecular beam epitaxy and more specifically quantum dot growth. An overview of the device processing methods used in this project is presented, and then followed by a discussion on the optical and electrical characterisation methods of solar cells.

3.1 Epitaxial Growth

3.1.1 Introduction

Epitaxial growth is the deposition of crystalline films on a substrate in order to create novel semiconductor structures. The term 'epitaxy', coined by Louis Royer in the 1920s, is a combination of the Greek words *epi*, meaning 'upon' and *taxis*, meaning 'order', to communicate the fact that the new crystal grown has an orientation determined by the crystalline substrate. The development of modern epitaxial growth techniques began in the 1960s. The rise in epitaxial growth study was spurred on by the idea that epitaxial structures with new electronic and optical characteristics could be developed. Over the years, advances in epitaxial growth technology have made atomic-scale control of growth layers a matter of routine. Today, there are two main epitaxial growth techniques that are used to produce high quality III-V compound heterostructures. These are metal-organic vapour phase epitaxy (MOVPE) and molecular beam epitaxy (MBE). The main difference between these techniques is in the method of deposition. In MBE, the growth materials are delivered to the substrate as molecular beams under very high vacuum pressures, whereas in MOVPE, the growth materials are delivered by gas phase and surface chemical reactions at moderate vacuum pressures. Even though MBE has relatively slower growth rates, it has an advantage over MOVPE in terms of its precision and its ability to apply *in situ* surface analytical techniques to monitor the growth process in real time.

3.1.2 Molecular Beam Epitaxy

Molecular beam epitaxy (MBE) is an ultra-high vacuum (UHV) epitaxial growth technique that operates by beaming atoms and molecules onto a heated crystalline substrate surface [1]–[3]. The significant developments in III-V compound semiconductor growth by MBE were attained by Al Cho and John Arthur at Bell Telephone Laboratories in New Jersey, U.S.A. Variations of MBE have been developed, such as the Gas-Source MBE, which uses hydrides

like arsine (AsH_3) as a group-V source, and metal-organic MBE which uses metal-organic compounds like triethylgallium (TEGa) as a group-III source. In Solid-Source MBE growth, elemental source materials in high purity crucibles in cells, known as Knudsen cells or effusion cells are heated to evaporate the growth materials.

This forms beams of homoatomic molecules (e.g. atomic Ga, As_2, As_4, atomic Si etc.) that are directed towards the substrate, which is heated and rotated for uniform deposition. The flux rates of the collision-free molecular beams depend on the temperature of the effusion cells. The flux rates are determined by an ion gauge. The morphology of the growing surface is determined by the migration of the deposited species. The migration and hence morphology depends on the flux rates, substrate temperature, the surface material and its crystallographic orientation [4].

A schematic diagram of an MBE growth chamber is shown in Figure 3.1.The growth chamber of an MBE is kept at pressures in the region of 10^{-11} Torr in order to reduce the background pressure of contaminants. In order to ensure this UHV condition during growth, the chamber is fitted with a liquid nitrogen cooled shroud. The effusion cells have mechanical stutters with fast actuation times (typically < 0.1s), which are used to ensure an abrupt change of composition and also to deposit less than a monolayer of material.

During the growth, Reflection High Energy Electron Diffraction (RHEED) can be used to monitor and study the evolution of the growing surface. A RHEED set-up consists of an electron gun (10-20 keV) that fires electrons onto the substrate being grown at a glancing angle (~0.5^o- 3.0^o) [4] and a fluorescent screen that displays the diffracted pattern of electrons. A camera is usually used to video the fluorescent screen and displays it on a computer screen. These diffraction patterns have been studied and are well-known, so qualitative information about the surface roughness can be acquired.

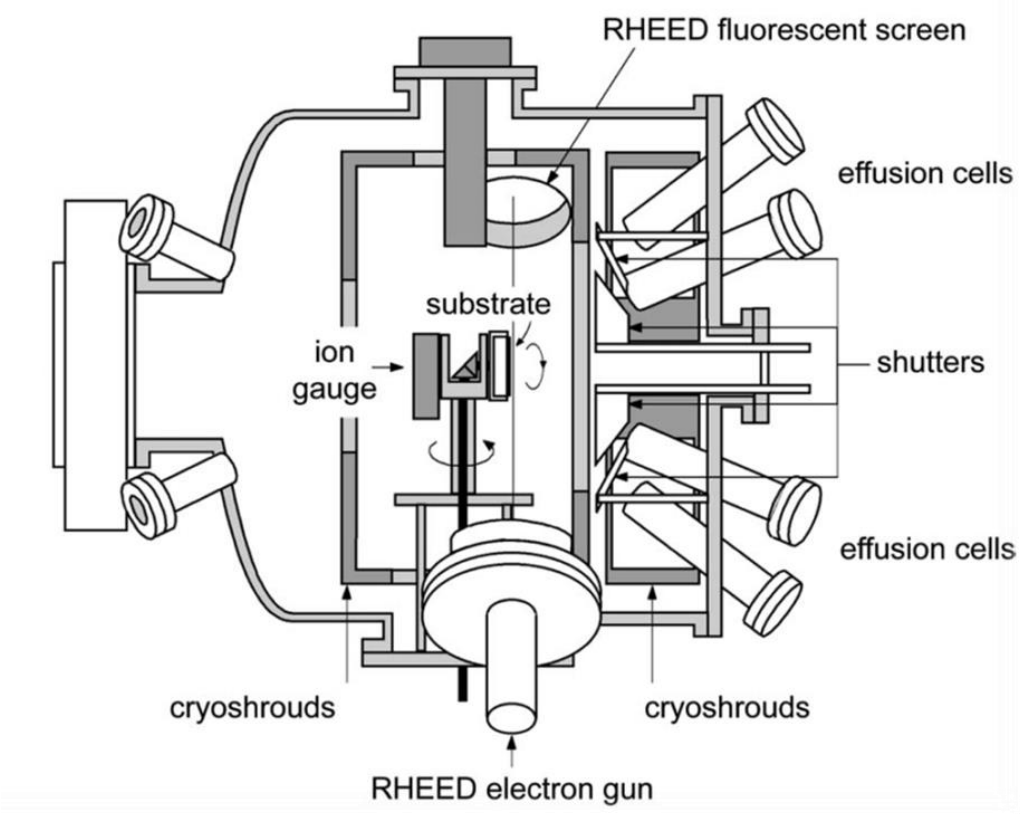

Figure 3.1 Schematic of diagram of an MBE growth chamber [5].

From the symmetry of the RHEED pattern, the crystallographic symmetry can be ascertained and the extent of the long-range order of the growth surface can be determined from the sharpness of the pattern. The constructive and destructive interference of the diffracted electrons resulting from the MBE growth of an epitaxial GaAs layer on a GaAs substrate is shown in Figure 3.2. It has been shown by Cho experimentally that the streaky pattern corresponds to an atomically flat surface [6]. There are different surface arrangements of atoms on semiconductor surfaces during growth. These surface reconstructions occur in order to lower surface energy by minimising the number of dangling bonds [7].

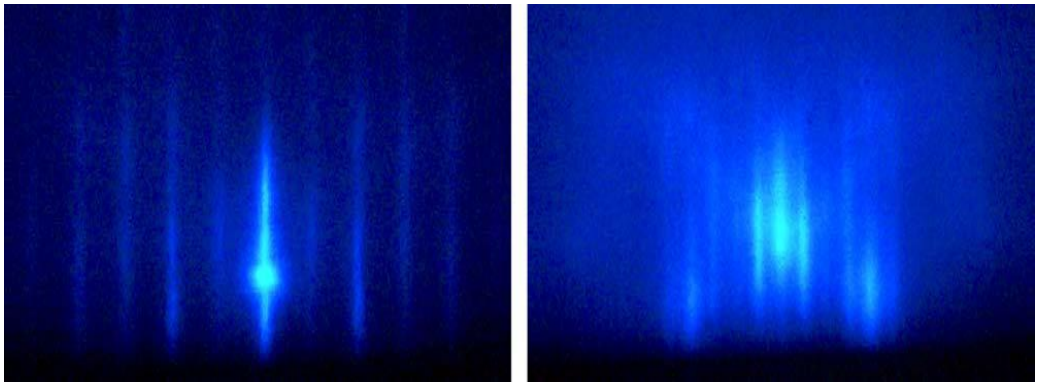

Figure 3.2 RHEED patterns during the growth of a GaAs epilayer on a GaAs (100) substrate [5].

RHEED also gives information on the time it takes to grow a monolayer of material. At the beginning of growth in two-dimensional (2D) growth mode when the surface is flat, the RHEED intensity is high. 2D islands begin to form and as growth continues, RHEED intensity decreases until it reaches a minimum. As the islands coalesce, the atomic steps decrease and the RHEED intensity increases until it reaches a maximum when a monolayer is complete. This process is illustrated in Figure 3.3.

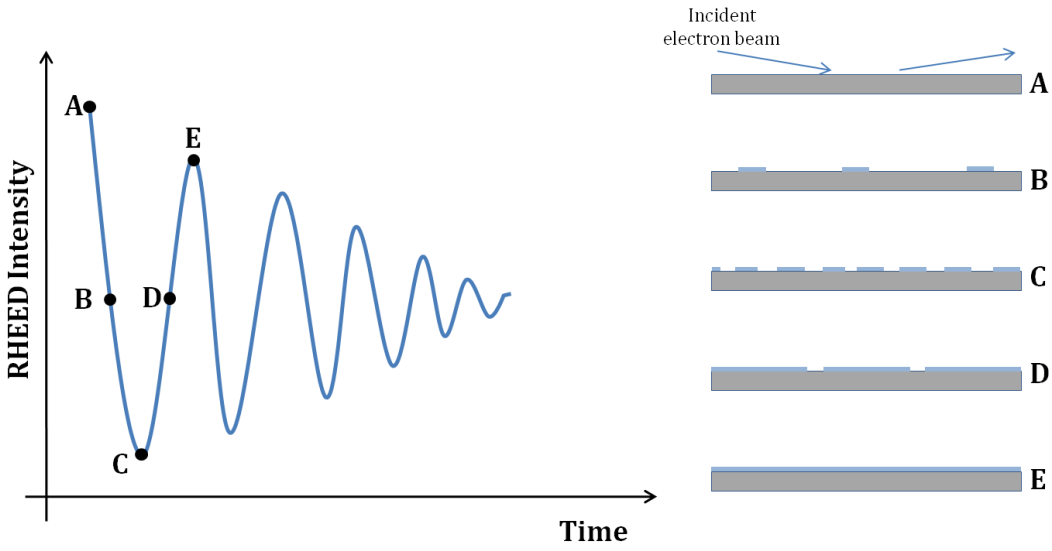

Figure 3.3 RHEED intensity oscillation at different stages of the growth of a monolayer. (Adapted from [5]**)**

The period of the oscillation is the time it takes to complete a monolayer of growth. The decaying envelope of the oscillation is due to the fact that 2D growth is imperfect, with upper growth layers beginning to form before lower ones are fully completed. As already mentioned, for growth of a single monolayer, the operation time of the shutters should be faster than the time needed to grow one monolayer (typically 1 – 5s). MBE machines are also equipped with mass spectrometers to analyse the chemical composition of the residual atmosphere.

3.1.3 MBE Growth Mechanisms

The study of the MBE growth mechanisms of III-V semiconductors has revealed that group-III (cations) species are chemisorbed onto the growing surface before they migrate to find a suitable lattice site at which they are incorporated [8]. On the other hand group-V (anions) species, which reach the growth surface as dimers or tetramers, have been shown to be physisorbed to the growing surface as it migrates before dissociating and incorporating by bonding to a cation [9]. This is because at typical growth temperatures, Cho *et al.* found that group-III elements have unity sticking coefficients to the substrate surfaces, whereas group-V elements do not stick to the surface in the absence of group-III atoms [1]. For this reason, excess group-V atoms are desorbed from the surface and hence, the growth rate of III-V compounds is solely governed by the rate of the group-III flux.

There are two major epitaxial growth modes associated with the growth of III-V semiconductors by MBE; two-dimensional (2D) growth and three-dimensional (3D) growth. 2D growth occurs when group-III cations favour incorporation at the edge of existing islands instead of on top of them. The growth mode described by Figure is known as a layer-by-layer 2D growth. The decay of the RHEED intensity envelope suggests that the layer-by-layer growth is imperfect; new islands begin to form on layers that are not yet completed. This is because in this case, the surface migration length is shorter than the mean distance between islands. There is another 2D growth

mode in which, the surface migration length is longer than the mean distance between islands. In that case, growth precedes by the flow of the edges of existing islands, hence the name, step-flow 2D growth. This growth mode will have a constant RHEED intensity value throughout the growth. As already mentioned, the difference between these two 2D growth modes is the migration length, which is dependent on the growth temperature. At low growth temperatures, migration length is short and the probability of having uncompleted lower layers is high. However, at higher growth temperatures, the increased migration length might lead to vacancies in lower layers. Therefore, there exists an optimum material dependent growth temperature, at which there is a smooth interface. Techniques such as Migration Enhanced Epitaxy (MEE) and Atomic Layer MBE (ALMBE) have been developed for growth of smooth interfaces at low temperatures [10].

The growth of a lattice-mismatched heteroepitaxial structure begins in 2D layer-by-layer growth mode. The epilayer is forced to fit the lattice constant of the growing surface. This leads to a build-up of a misfit strain in a layer known as the wetting layer. As the thickness of the wetting layer increases, eventually there is a relaxation of the strain leading to the formation of 3D islands. The 2D-to-3D transition occurs when the critical coverage of the growth material is exceeded. At the point of transition, the RHEED pattern shows a chevron-like pattern (Figure 3.4) that is typical of 3D island formation. The critical coverage is dependent on the lattice mismatch, as well as growth conditions such as growth temperature and growth rate [11]. This growth of 3D islands is known as Stranski-Krastanow growth [12]. This is the mechanism by which self-assembled quantum dots (QD) are grown, and its implications and applications will be discussed in section 3.1.4. The Volmer-Weber morphology is another 3D growth mode that leaves part of the substrate exposed (i.e. no wetting layer) and it is based on lattice-matched systems.

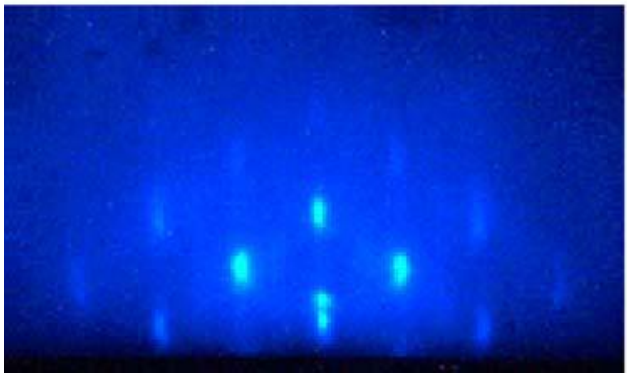

Figure 3.4 RHEED screen showing the chevron-like patterns at the point to 2D to 3D transition[5].

At this point it is clear that depending on the structure being grown, a lattice-mismatch can be either advantageous or not. In cases where 2D growth is required even though there is a lattice mismatch between the substrate and the epilayer, a lattice matched metamorphic buffer layer can be used. Metamorphic growth involves compositionally grading a buffer layer to change the crystal lattice constant from that of the substrate to a virtual substrate. This localises defects and misfits away from the active layers of a device. Figure 3.5 compares the lattice constants of various III-V and II-VI compounds.

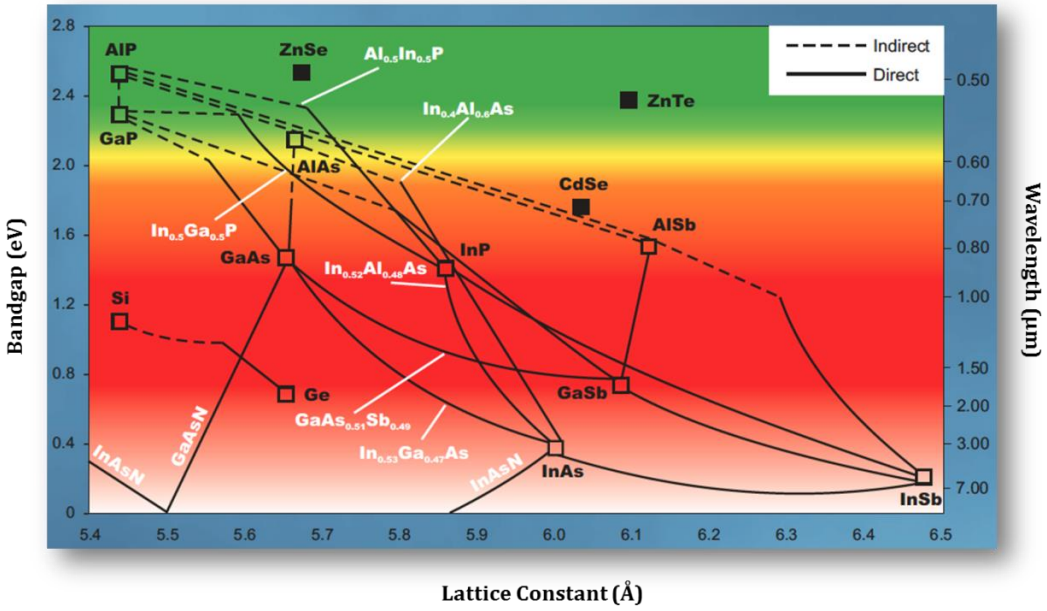

Figure 3.5 Bandgap versus lattice constant for III-V alloys and some II-VI alloys [13].

3.1.4 Self-Assembled Quantum Dots

Quantum dots (QDs) are nano-sized crystals of semiconductor material that confine carriers in all three dimensions. This is achieved when self-assembled 3D islands grown by Stranski-Krastanow growth mode are placed within a matrix of a higher bandgap material. Three-dimensional quantum confinement occurs when both the mean free path and the de Broglie wavelength of carriers is greater than the critical size of nanostructures.[5] III-V QDs mismatched heteroepitaxial systems such as InAs/GaAs [14], InAsSb/GaAs [15], InAs/GaAsSb [16] and InP/GaAs [17] have been grown. As already explained, the formation of QDs is due to the relaxation of the elastic strain that is built up within the mismatched epilayers. The shapes of the QDs have been observed to be elongated truncated pyramids, with typical base diameters and heights in the order of few tens of nanometres and few nanometres, respectively.

With a lattice-mismatch of 7%, InAs QDs on GaAs is the most studied QD system to date. The total critical layer thickness for surface elastic relaxation of InAs islands on GaAs is 1.50ML [18]. After the formation of quantum dots, a few seconds of growth interruption improves the dot size uniformity [19]. It has been shown that a low growth rate and a high arsenic pressure lead to the formation of high quality InAs QDs. As illustrated in Figure 3.6 the InAs wetting layer conforms to the lattice constant of the GaAs, but the QD above will have a distorted lattice plane with a high surface energy.

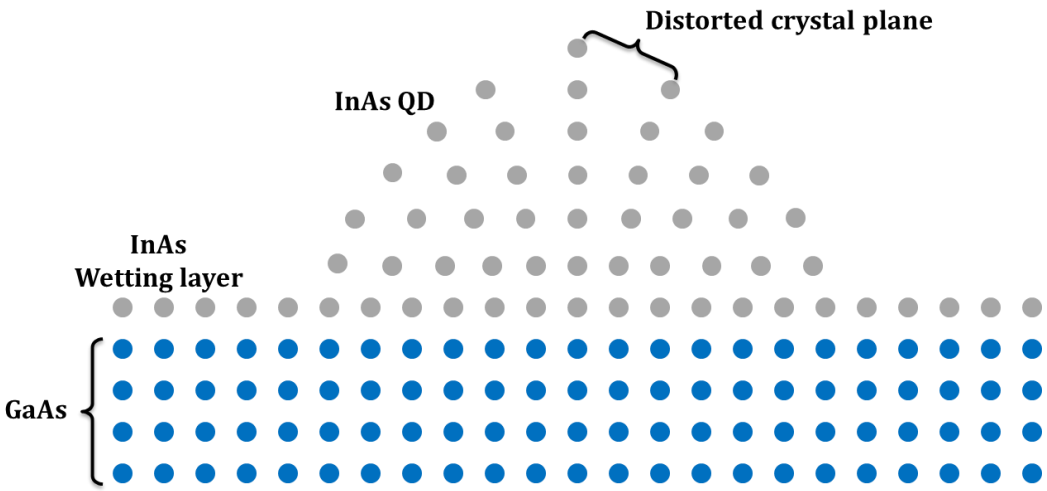

Figure 3.6 Schematic showing lattice distortion in an InAs/GaAs self-assembled quantum dot.

When layers of QDs are grown on top of each other, the lattice distortion of the dots and the interdiffusion of species between the dots and the surrounding barrier material, result in a change in the morphology and the composition of the dots. Stacking of QD layers has to be separated by a spacer layer that is thick enough to ensure that the strain field induced by the dots in a layer do not affect the formation of dots in upper layers.

The primary advantage of using QDs in electronic and optical device is the ability to precisely control the bandgap by its size. In addition to this, QDs structures have been shown to suppress the lateral migration of carriers, making QD devices less susceptible to edge or surface recombination [20]. Another advantage is their insensitivity to temperature [21] which has proved promising for laser and concentrator solar cell applications. Cress et al. have also shown that QD solar cells have an enhancement in radiation tolerance compared to bulk solar cells, which could be useful for space applications where end-of-life performance is critical [22].

3.1.5 Atomic Force Microscopy

The atomic force microscope (AFM) is a scanning technique that is used to study, at the nano-scale level, the topography of surfaces of a variety of materials. AFM was first proposed as a high resolution imaging technique, as an alternative to scanning tunnel microscope (STM) which is able to image only conductive surfaces [23]. An AFM set up typically consists of a probing tip at the end of flexible microcantilever arm, a laser source and a photodiode. As the probe scans the surface of interest, the force between the probe and the sample surface causes a deflection of the laser beam. The deflection of the laser beam off the microcantilever is monitored by the photodiode. This information can then be used to generate high resolution images, two- and three-dimension, of the surface.

AFM has been the main technique used to analyse the density and size distribution of uncapped QDs. Figure 3.7 shows AFM images of InAs QDs on InGaAs grown by MBE at UCL. The areal density of the uncapped QDs is approximately 4.6 x 10^{10} cm^{-2}. The height of the QDs is between 5 nm and 10 nm, and the diameter is between 30 nm and 50 nm.

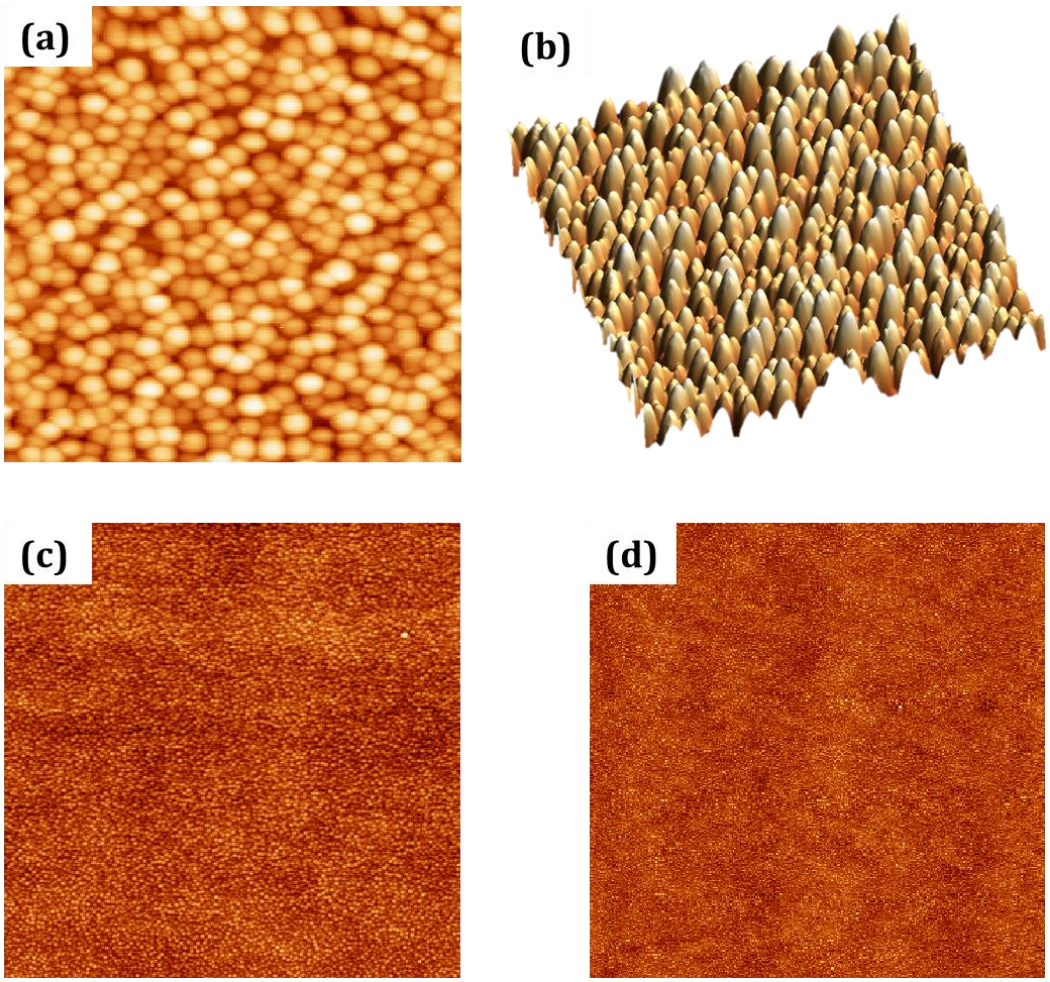

Figure 3.7 AFM image of InAs QDs on InGaAs. (a) and (b) are the 1 *x* 1 μm² images of the quantum dots in two- and three-dimensions, (c) and (d) are the 5 *x* 5 μm² and 9 *x* 9 μm² images.

3.1.6 Transmission Electron Microscopy

A high resolution microscopy technique such as Transmission Electron Microscopy (TEM) is widely used to study the cross-section characteristics of stacked QD layers. TEM involves the transmission of electrons through a sample. The interaction between the electrons and the sample is then used to generate an image that is magnified and focus unto an imaging device. Figure 3.8 shows typical TEM images of QD structures.

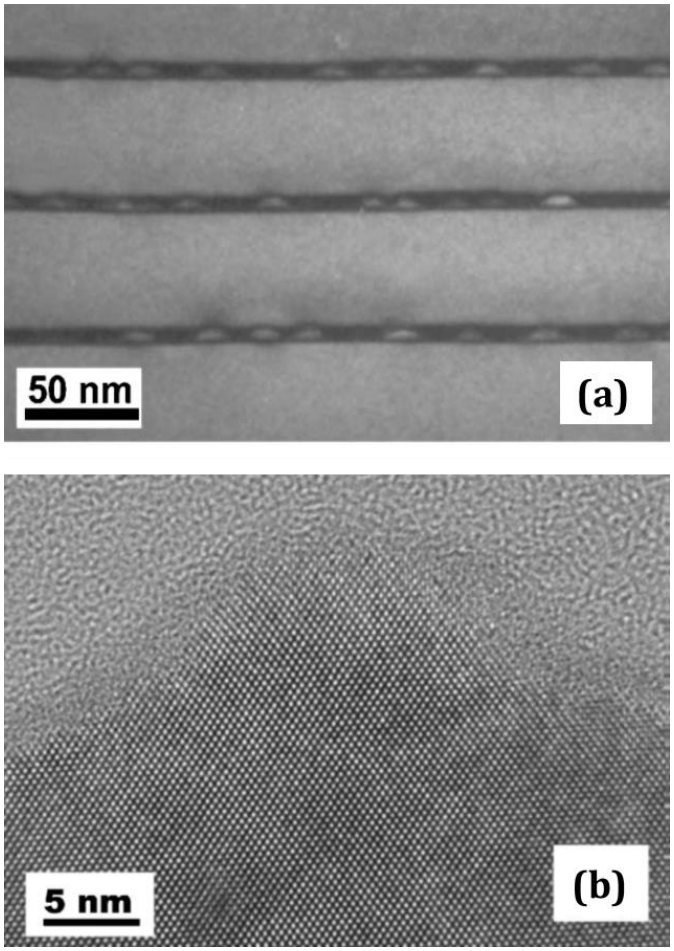

Figure 3.8 (a) TEM image of a multi-layer stack of InAs QDs in an InGaAs quantum well (b) High-resolution TEM image of a single InAs QD. [24]

3.2 Device Processing

3.2.1 Introduction

After epitaxial growth is complete, a semiconductor wafer leaving the MBE, might have all the semiconductor layers necessary to make a solar cell, but it cannot operate as such until it has gone through processing. The device fabrication stage is where metal contacts are deposited on the solar cell structure to allow the extraction of current and voltage. The standard semiconductor lithography method for the fabrication of GaAs solar cells typically involves five major steps; cleaning, photolithography, wet etching, metallisation and annealing. An outline of this device fabrication process is shown as a flow chart in Figure 3.9.

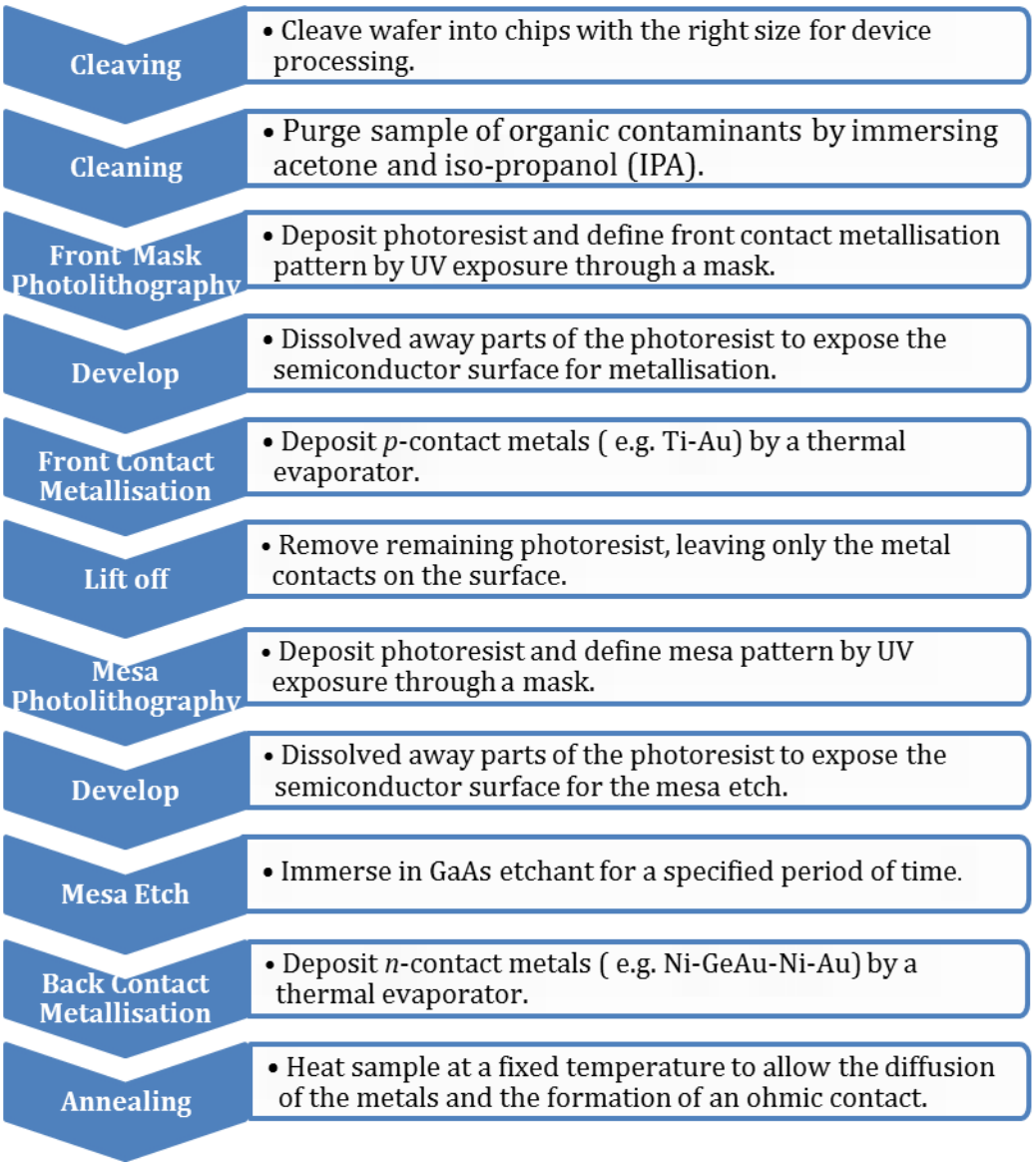

Figure 3.9 Flow chart of device fabrication process from wafer to solar cell device.

A brief overview of each of the five major steps is presented to highlight the fundamentals of GaAs processing methods. At the initial stages of the project, the photolithography method was used, to fabricate test solar cells at the LCN. However, the poor ohmic contact results achieved meant that a proper working device could not be attained. Fortunately, another device processing method using a thin metal mask, instead of photolithography, simplified the fabrication and yielded better ohmic contacts. This method is subsequently outlined.

3.2.2 Cleaning

To achieve high quality reproducible devices, the fabrication process must be free of contaminants. As a first step, the cleaning process ensures unwanted materials are removed before subsequent processes are carried out. Organic solvents such as acetone and isopropyl alcohol (IPA) are good at removing oils and organic materials. The cleaved wafers were placed in acetone and then IPA, and each time in an ultra-sonic bath for 5 minutes. The lack of cleanliness at the start will result in problems with metal adhesion and wet etching. During the whole device fabrication process, the level of cleanliness must be maintained by proper handling. The minutest traces of contaminants on tweezers and sample holders can compromise the quality of the device.

3.2.3 Photolithography

Photolithography is the dominant technique for defining patterns for metallisation during semiconductor processing. Light sensitive chemicals called photoresists are spin-coated onto a sample and then selectively exposed to UV light through an optical mask. In GaAs processing the deposition of the photoresist is usually followed immediately by a soft bake that removes water and solvents and hardens the photoresist film to improve adhesion. The development stage that follows will remove the exposed resist in the case of a positive resist or remove the unexposed resist in the case of a negative resist. The desired metal alloys can then deposited by a thermal evaporator. The metal on the photoresist is then "lifted off" by a solvent leaving behind the metal on the sample. The multilevel resist technique is used to implement an undercut for successful lift-off. In developing the test solar cell devices, two positive photoresists, Lift-Off Resist (LOR10B) and then Shipley S1818 were used. First, LOR10B was spin-coated onto the sample at 4000 rpm for 30 seconds. The sample was then baked at 190 ^{o}C for 10 minutes. After cooling, Shipley S1818 was also spin-coated onto the sample at 4000 rpm for 30 seconds, followed by a bake at 105 ^{o}C for 1 minute. After a 5 seconds exposure under UV light, 45 seconds in the MF319

developer (dilute ammonium hydroxide) defined the mask profile. Before metallisation it is useful to remove oxides on the GaAs surface. This was done in a solution of HCl : H_2O (1:1) for 10 seconds. After the deposition of the front metal contacts, acetone was used to achieve lift-off (i.e. removal of Shipley S1818). This was followed by a soak in MF319 to remove LOR10B. The lift-off and the multilevel resist techniques are illustrated in Figure 3.10.

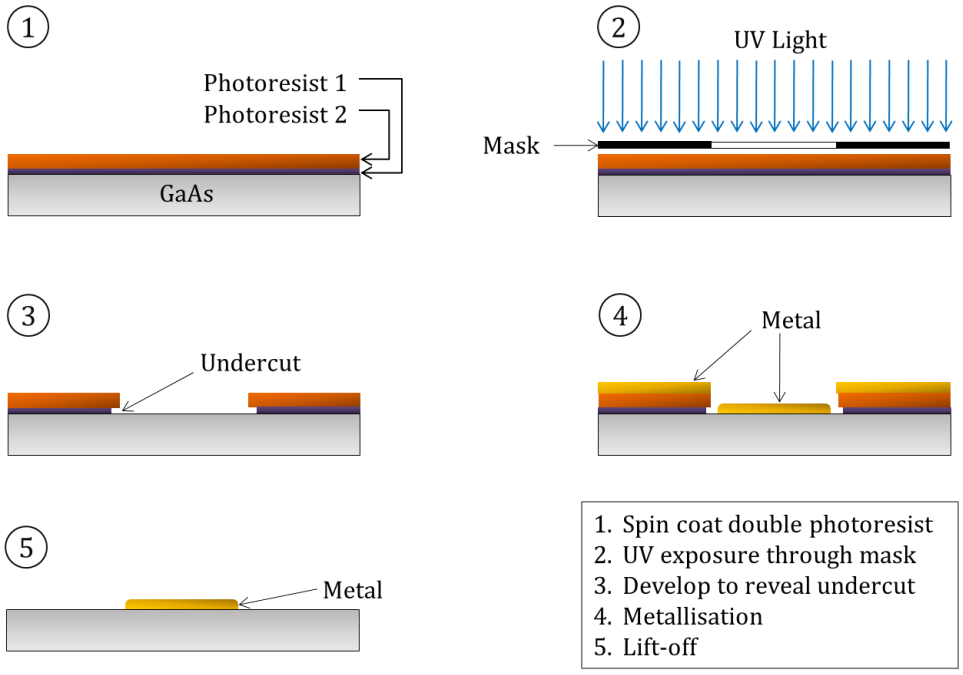

Figure 3.10 Lift-off procedure.

3.2.4 Wet Etching

After the deposition of top metal contacts, it is necessary to isolate devices on the sample to ensure current and optical confinement. A wet etching procedure is used to create a mesa that serves this purpose. Another photolithography process is required to produce a mesa pattern to protect the active device area. GaAs etchants operate in two steps. First they oxidise the surface and then dissolve the oxide, eradicating some Ga and As atoms in the process [25]. Mesa etch was carried out by immersing samples in a solution of H_3PO_3: H_2O_2: H_2O (1:1:3). The etch depth is checked using a Dektak profiler. Based on the typical etch rate of 0.3μm per minute, the etch time is determined for the desired depth.

3.2.5 Metallisation

A thermal evaporator is used to deposit the desired metals onto a sample to create an ohmic contact. An ohmic contact is a thin Schottky barrier that allows conduction across the metal-semiconductor junction by tunneling. It is required that the surface layer of the sample being processed be highly doped. For *n*-type, systems such as Au-Ge, Au-Ge-Ni and InGe-Au are typical. And for *p*-type, Zn/Au and AuBe-Au have been shown to produce ohmic contacts with a contact resistance of 10^{-5} Ωcm^2. However, these materials are not tightly adhered to the epilayer. Cr/Au contacts to *p*-type GaAs has been shown to have relatively low contact resistance ($\sim 2x10^{-6}$ Ωcm^2) and good adhesion [26]. For the test solar cell sample, Ti/Au (5nm/200nm) was used for the *p*-type contact and Ni/GeAu/Ni/Au (5nm/125nm/20nm/200nm) was used for the *n*-contact. A multi-source evaporator system was used with a film thickness monitor ensuring the correct layer thicknesses were deposited.

3.2.6 Annealing

The annealing of the sample is the final step after the metallisation. Annealing is basically heating the sample at a fixed temperature for duration of time. This process aids the formation of an ohmic contact. The test samples were annealed in a rapid thermal annealer by ramping up to 400 ^oC for 30 seconds, and then cooling in N_2 atmosphere.

3.2.7 Device Processing of Solar Cells using metal mask

A thin metal mask can be used to define patterns for metallisation instead of an optical mask, as in the photolithography technique. In this case, metal contacts are deposited directly through the metal mask and onto the wafer sample. In skipping photolithography with the metal mask method, the dimensions of the front contact grid patterns are bigger which takes up a lot more wafer; however, the fabrication of solar cells is simpler. The steps that were used for solar cell processing with this method are listed below.

i. Cleave the right sized wafers for the mask. For the mask that was used, a wafer sample of 1×1 cm^2 is able to accommodate 4 solar cells. The mask grid pattern is shown in Figure 3.11(a).

ii. As previously mentioned, acetone and then IPA, were used to clean the wafers in an ultra-sonic bath, each time for 5 minutes. Samples were then rinsed in de-ionized (DI) water and blown dry with N_2.

iii. The surface oxide was etched using in a solution of HCl : H_2O (1:1) for 10 seconds. After that, samples were rinsed in 10 changes of DI water, and then blown dry.

iv. The *n*-type back contact metal, AuGe/Au (250 nm/650 nm) was then deposited using a thermal evaporator.

v. After that the *p*-type front contact AuZn/Au (250 nm/650 nm) was deposited also with a thermal evaporator. Care was taken in aligning and securing the edge of the wafer sample to the pattern of the metal mask.

vi. Using a knife-edge and a pair of tweezers, individual solar cells were separated by careful and precise cleaving.

Figure 3.11(b) shows a complete processed cell. The solar cells discussed in Chapters 5 and 6 were fabricated using the method described above, using a 100μm thick stainless steel mask. The usual step of etching the GaAs contact layer and depositing an anti-reflective coating was not applied in both cases.

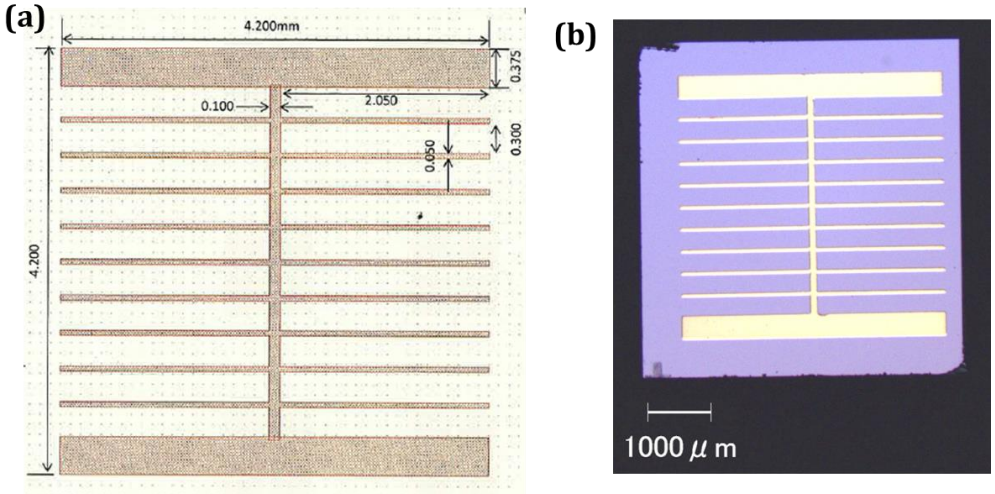

Figure 3.11 (a) Metal mask grid pattern (b) Solar cell processed with metal mask

3.3 Characterisation

3.3.1 Introduction

After device fabrication of solar cells, an evaluation method is employed to characterise the sample. This section presents the techniques used to characterise the optical and electrical properties of solar cells.

3.3.2 Photoluminescence

Photoluminescence (PL) is an optical technique that has proved very popular for the characterisation of silicon, germanium, epitaxially grown II-VI and III-V compound semiconductor structures. It is a non-destructive technique that allows defects and impurities in a sample to be studied [27]. PL is also an excellent method for analysing the band structures of nanostructures such as quantum well and quantum dots.

PL is basically the optical excitation of a semiconductor sample, creating electron-hole pairs and then collecting and detecting the radiation emitted (due to radiative recombination) by the sample at various wavelengths. PL is typically taken at room temperature and also at lower temperatures up to 10K. Low temperature PL is useful because it reduces the effect of thermally activated non-radiative recombination and also places carriers in their ground state limiting their interaction with excited states.

The PL measurements in this thesis were carried out by a 532nm continuous wave diode-pumped solid-state (DPSS) laser. The optical intensity (measured in arbitrary units) at various wavelengths is detected using a 0.25m monochromator and a TE-cooled Ge photodetector. A close-cycle He cryostat is used to cool samples to acquire low temperature PL measurements. Lenses are used to focus the laser beam more sharply onto the sample and also to focus the radiated emission from the sample into the detector slit. Figure 3.12 shows a diagram of the set up used to take temperature dependent PL measurements. Chopping the PL radiation going into the monochromator allows the lock-in radiometer to reject noise, enhancing the accuracy of measurements.

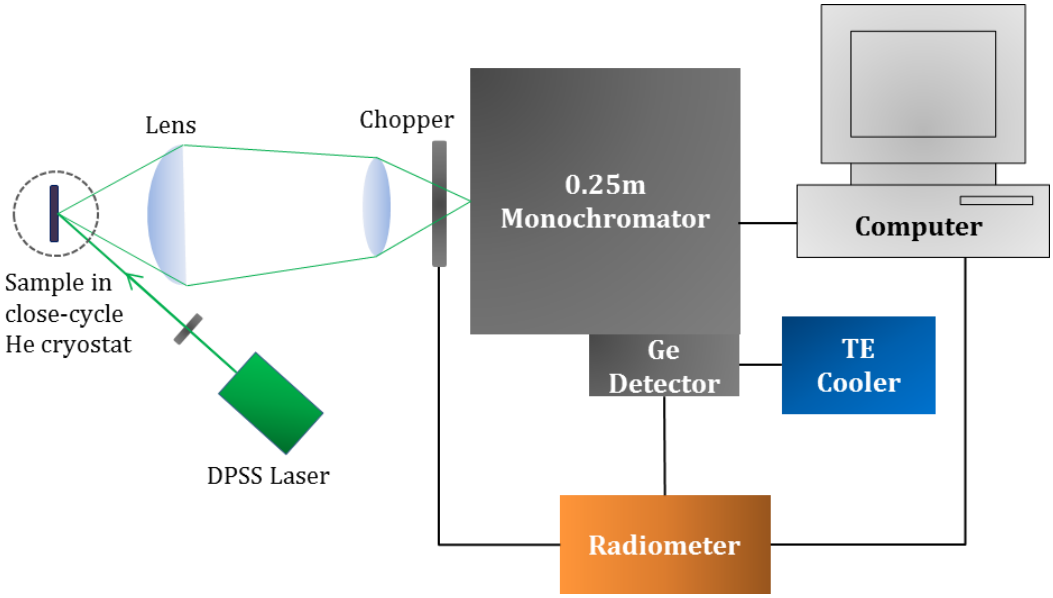

Figure 3.12 Photoluminescence equipment set up.

Generally, a strong PL intensity signifies more radiative recombination and less non-radiative recombination, hence a good structural quality. With regard to nanostructures such as QDs, the position of the PL peak and its linewidth informs of the size and the size distribution of dots in the sample. As the temperature is increased, the PL peak is redshifted. The redshift of PL peak energy with increasing temperature is evident of a temperature-induced bandgap change. The temperature dependence of the bandgap energy of a semiconductor, induced by the dilation of the lattice and other effects, is explained by a semi-empirical relationship, the Varshni equation [28]. Figure 3.13 shows some PL measurements taken with the PL set up above.

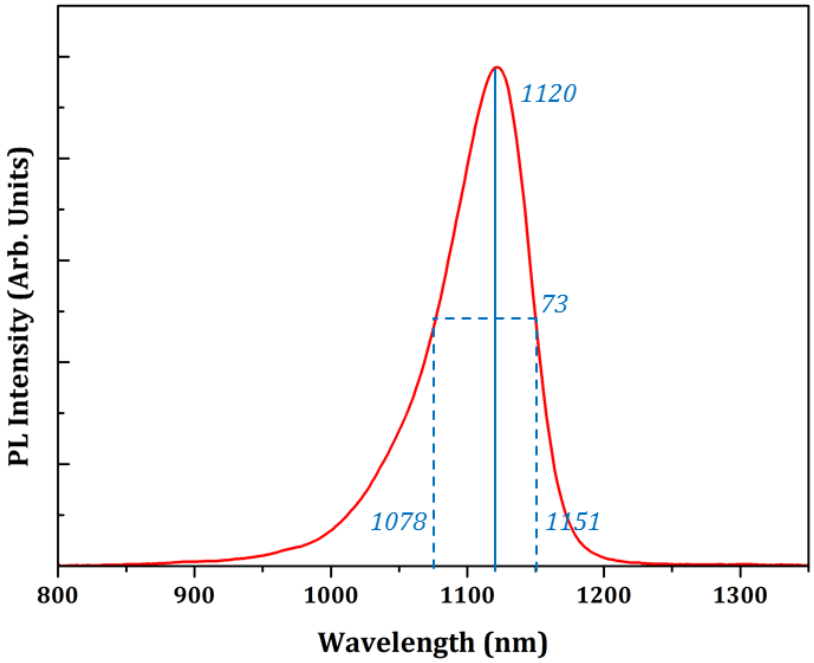

Figure 3.13 PL spectrum for InAs QDs on GaAs and capped by GaAsSb

3.3.3 Electrical Characterisation

For solar cell devices, the dark current gives the first hint of the quality of the device. A Keithley source-measure unit (SMU) is used to apply a small forward bias to the device and the current flowing through the device is measured in the dark. Light *J-V* curves can be obtained using the same equipment as the dark current but in this case the measurements are carried out under a solar simulator. The solar simulator system used was a Class AAA simulator with a xenon lamp, an AM1.5 Global filter adjusted to a power density of 1000 W/m^2. The parameters of the measurements were adjusted through a software provided by the system manufacturer. The measurement results are then stored in a text file. To ensure accurate measurements under the light source a temperature controlled copper stage was used to maintain the temperature of the solar cell at room temperature. EQE measurements were performed by measuring the spectral response of the device under test, as a beam of light from a monochromator scans through a wavelength range (typically 400 – 1300 nm). The light source was a 100 W quartz halogen bulb coupled through a chopper into the monochromator.

Bibliography

[1] A. Y. Cho and J. R. Arthur, "Molecular beam epitaxy," *Prog. Solid-State Chem.*, vol. 10, pp. 157–191, 1975.

[2] A. Y. Cho, "How molecular beam epitaxy (MBE) began and its projection into the future," *J. Cryst. Growth*, vol. 201–202, pp. 1–7, May 1999.

[3] J. R. Arthur, "Molecular beam epitaxy," *Surf. Sci.*, vol. 500, no. 1–3, pp. 189–217, Mar. 2002.

[4] K. Barnham and D. Vvedensky, *Low-Dimensional Semiconductor Structures: Fundamentals and Device Applications*. Cambridge University Press, 2008.

[5] S. Franchi, G. Trevisi, L. Seravalli, and P. Frigeri, "Quantum dot nanostructures and molecular beam epitaxy," *Prog. Cryst. Growth Charact. Mater.*, vol. 47, no. 2–3, pp. 166–195, 2003.

[6] A. Y. Cho, "Film Deposition by Molecular-Beam Techniques," *J. Vac. Sci. Technol.*, vol. 8, no. 5, p. S31, Sep. 1971.

[7] G. Qian, R. Martin, and D. Chadi, "First-principles study of the atomic reconstructions and energies of Ga-and As-stabilized GaAs (100) surfaces," *Phys. Rev. B*, vol. 38, no. 11, 1988.

[8] J. R. Arthur, "Interaction of Ga and AS2 Molecular Beams with GaAs Surfaces," *J. Appl. Phys.*, vol. 39, no. 8, p. 4032, 1968.

[9] C. T. Foxon and B. A. Joyce, "Interaction kinetics of As2 and Ga on {100} GaAs surfaces," *Surf. Sci.*, vol. 64, no. 1, pp. 293–304, 1977.

[10] Y. Horikoshi, "Advanced epitaxial growth techniques: atomic layer epitaxy and migration-enhanced epitaxy," *J. Cryst. Growth*, vol. 201–202, no. 3, pp. 150–158, May 1999.

[11] C. Heyn, "Critical coverage for strain-induced formation of InAs quantum dots," *Phys. Rev. B*, vol. 64, no. 16, pp. 1–7, Oct. 2001.

[12] I. N. Stranski and L. Krastanow, "Sitzungsber. Akad. Wiss. Wien," *Math.-Naturwiss. Kl., Abt. 2B*, vol. 146, p. 797, 1938.

[13] "Lattice Parameter & Bandgap Data," 2013. [Online]. Available: http://www.veeco.com/promos/lattice-parameter-and-bandgap-data.aspx. [Accessed: 01-Nov-2013].

[14] H. Y. Liu, B. Xu, Y. H. Chen, D. Ding, and Z. G. Wang, "Effects of seed layer on the realization of larger self-assembled coherent InAs/GaAs quantum dots," *J. Appl. Phys.*, vol. 88, no. 9, p. 5433, 2000.

[15] M. Kudo, T. Nakaoka, S. Iwamoto, and Y. Arakawa, "InAsSb Quantum Dots Grown on GaAs Substrates by Molecular Beam Epitaxy," *Jpn. J. Appl. Phys.*, vol. 44, no. 1, pp. 45–47, 2005.

[16] S. P. Bremner, A. Pancholi, K. Ghosh, S. Dahal, G. M. Liu, K. Y. Ban, M. Y. Levy, and C. B. Honsberg, "Growth of InAs Quantum Dots on GaAsSb for the realisation of a quantum dot solar cells on GaAs," in *33rd IEEE Photovoltaic Specialists Conference*, 2008.

[17] M. P. F. de Godoy, M. K. K. Nakaema, F. Iikawa, M. J. S. P. Brasil, J. M. J. Lopes, J. R. R. Bortoleto, M. A. Cotta, R. Magalhaes-Paniago, M. J. Morschbacher, and P. F. P. Fichtner, "Structural and optical properties of InP quantum dots grown on GaAs(001)," *J. Appl. Phys.*, vol. 101, no. 7, p. 073508, 2007.

[18] D. Leonard, K. Pond, and P. Petroff, "Critical layer thickness for self-assembled InAs islands on GaAs," *Phys. Rev. B*, vol. 50, no. 16, 1994.

[19] S. Kiravittaya, Y. Nakamura, and O. . Schmidt, "Photoluminescence linewidth narrowing of InAs/GaAs self-assembled quantum dots," *Phys. E Low-dimensional Syst. Nanostructures*, vol. 13, no. 2–4, pp. 224–228, Mar. 2002.

[20] D. P. Popescu, P. G. Eliseev, A. Stintz, and K. J. Malloy, "Carrier migration in structures with InAs quantum dots," *J. Appl. Phys.*, vol. 94, no. 4, p. 2454, 2003.

[21] M. Sugawara and M. Usami, "Quantum dot devices: Handling the heat," *Nat. Photonics*, vol. 3, no. 1, pp. 30–31, 2009.

[22] C. D. Cress, S. M. Hubbard, B. J. Landi, R. P. Raffaelle, and D. M. Wilt, "Quantum dot solar cell tolerance to alpha-particle irradiation," *Appl. Phys. Lett.*, vol. 91, no. 18, p. 183108, 2007.

[23] G. Binning, C. F. Quate, and C. Gerber, "Atomic force microscopy," *Phys. Rev. Lett.*, vol. 56, pp. 930–933, Sep. 1986.

[24] H. Y. Liu, C. M. Tey, I. R. Sellers, T. J. Badcock, D. J. Mowbray, M. S. Skolnick, R. Beanland, M. Hopkinson, and A. G. Cullis, "Mechanism for improvements of optical properties of 1.3-μm InAs/GaAs quantum dots by a combined InAlAs–InGaAs cap layer," *J. Appl. Phys.*, vol. 98, no. 8, p. 083516, 2005.

[25] R. Williams, *Modern GaAs processing methods*. Artech House, 1990.

[26] S. E. Aleksandrov, V. V. Volkov, and V. P. Ivanova, "Non-alloy Cr/Au Ohmic contacts in the technology of planar beam-lead GaAs pin diodes," *Tech. Phys. Lett.*, vol. 31, no. 7, pp. 581–583, 2005.

[27] K. Smith, "Photoluminescence of semiconductor materials," *Thin Solid Films*, vol. 84, no. 2, pp. 171–182, Oct. 1981.

[28] E. Grilli, M. Guzzi, R. Zamboni, and L. Pavesi, "High-precision determination of the temperature dependence of the fundamental energy gap in gallium arsenide.," *Phys. Rev. B. Condens. Matter*, vol. 45, no. 4, pp. 1638–1644, Jan. 1992.

Chapter 4

InAs/InGaAs dot-in-a-well Solar Cells with High-Growth Temperature Spacer Layer

The use of a dots-in-a-well (DWELL) structure for QD IBSCs has been shown to have many advantages. InAs quantum dots (QD) have been typically embedded within an InGaAs quantum well (QW) as an approach to create QD systems that emit at 1300 nm [1]. The insensitivity to edge recombination of the DWELL design for solar cells has been shown by Gu *et al* [2]. Not only does the InGaAs act as to reduce the strain between InAs and GaAs [3] but it has also been shown that growing InAs QDs on InGaAs rather than on GaAs leads to an increase in dot density. This increase in dot density is due to the incorporation of additional material from the InGaAs layer and reduced strained between InAs QDs and InGaAs buffer layer [4].

It has been well established that the growth temperature of GaAs spacer layers (SPLs) play an important role to minimize defect formation in 3- and 5-layer 1300-nm InAs/GaAs QDs with relatively thick GaAs SPLs (50 nm), in which the influence of strain fields from QD layers on subsequent QDs is trivial, and hence does not affect the performance of QD laser diodes [5]. In comparison with QD lasers, much more QD layers with thinner SPLs are required for QDSCs. Hence, it is necessary to study the growth conditions of the SPLs between the QD layers to maximise the QD volume density without

introducing the defects. The MBE growth, device fabrication and characterisation of 30 layer InAs/GaAs DWELL solar cells are discussed in the first section of this chapter. The influence of using a high-growth-temperature GaAs spacer layer (HGTSL) was investigated. In this work, it was shown that show that the defect formation in 30-layer InAs/GaAs QD structures can be significantly suppressed by the use of the HGTSL. The incorporation of the HGTSL results in a significant increase in the short-circuit current for a 30-layer InAs/GaAs QDSC with absorption at ~ 1.0 eV compared to the QDSC without HGTSL.

4.1 Experimental Work

4.1.1 Growth Details

The InAs/GaAs QDSC structures were grown by a Veeco Gen930 solid-source MBE system on *n*-type (100) GaAs substrate. An in-situ 15 keV RHEED system was used to monitor the growth process and the substrate temperature was measured by a pyrometer. Under As_2 rich conditions, the GaAs substrates were heated to a temperature of 610 ^{o}C for 8 minutes to deoxidise the surface. As explained in the previous chapter, group V atoms are easily desorbed, therefore deoxidation is done under As_2 rich conditions to ensure that there is a steady supply of As atoms on the substrate surfaces. The base pressure of the growth chamber was 10^{-9} Torr. Si and Be sources were used for *n*-type and *p*-type doping respectively.

The QDSCs contain 30-layer InAs/InGaAs DWELL structure which was inserted into the intrinsic region of a GaAs *p-i-n* cell. To enhance the absorption within the QD region, it is preferable to maximise the number of stacked QD layers without the introduction of defects. It was possible to grow 30 QD layers because of the advantage of reduced strain between the InAs and GaAs within the DWELL system. Each DWELL layer consists of 2.2 monolayers (ML) of InAs QDs grown on 2 nm of $In_{0.15}Ga_{0.85}As$ and capped by 4.5 nm $In_{0.15}Ga_{0.85}As$. Based on growth of test samples, it was observed that a combination of 2.2 MLs of InAs deposited at a temperature of 500 ^{o}C resulted

in a QD array that was uniform and of good structural quality. A 29 nm GaAs SPL separates the DWELLs, with an outer GaAs layer of 10 nm completing the *i*-region. This thickness of GaAs SPL is enough to ensure that strain fields from QD layers do not affect subsequent ones. Furthermore, it has been shown that electronic coupling is not required for the formation of an intermediate band with a separate Fermi level [6]. The *p*-type emitter and *n*-type base layer thickness are 400 nm and 3000 nm respectively. A 43nm AlGaAs window was grown underneath a 1000-nm GaAs *p*+ contact layer. A GaAs reference cell has been grown without QDs. Two InAs/InGaAs DWELL solar cells were grown, one with HGTSL and the other without. The HGTSL technique refers to increasing the growth temperature for part of the SPL. For the HGTSL sample, each DWELL was followed by an initial 3 nm of GaAs grown at 510 ^{o}C, and then the substrate temperature is increased to 580 ^{o}C for the remaining 26 nm GaAs, and then reduced back to 510 ^{o}C again for the growth of the next DWELL. In the case of the non-HGTSL devices, all of the GaAs SPL was deposited at 510 ^{o}C. A schematic diagram of the 30-layer InAs/GaAs DWELL solar cell is presented in Figure 4.1.

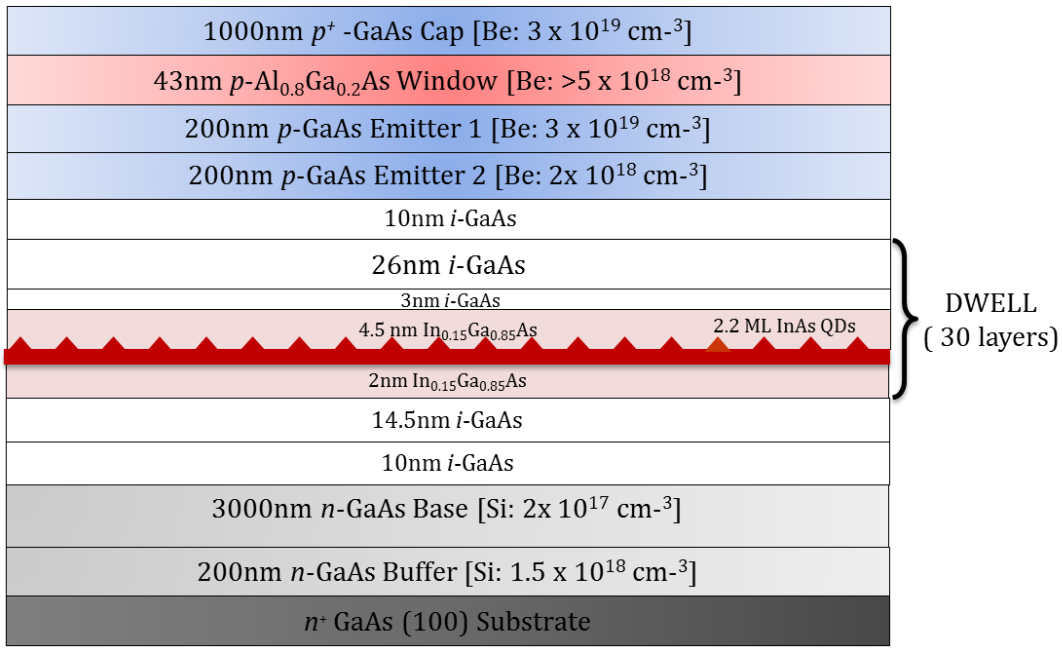

Figure 4.1 Schematic of the InAs/InGaAs DWELL solar cell structure

4.1.2 Device Fabrication and Characterisation

The solar cells were fabricated using standard III-V processing techniques. The contacts were Au-Zn-Au and InGe-Au for the *p* an *n* contacts, respectively. The current density – voltage (*J-V*) characteristics were measured using a solar simulator at room temperature under 1 sun AM1.5 illumination. The external quantum efficiency (EQE) was also obtained. Photoluminescence (PL) measurements were performed in a close-cycle helium cryostat under 532 nm excitation from a diode-pumped solid-state laser. The luminescence spectra were dispersed by a 0.25m monochromator and detected by a TE-cooled Ge detector. Temperature dependent PL measurements were taken from 10K to 300K at a laser power of 60 mW. For atomic force microscope (AFM) measurements, the growth was stopped after the formation of the InAs QDs and images were obtained using a Veeco diDimension AFM system.

4.2 Results and Discussion

4.2.1 Structural Characterisation

Figure 4.2 shows the cross-sectional transmission electron microscope (TEM) images for the 30-QD-layer QDSCs with and without HGTSL. The QDSC with HGTSL has a good structural quality with no defects as can be observed in Figure 4.2(a). The QDSC without HGTSL, as shown in Figure 4.2(b) on the other hand has a high-density of threading dislocations, which are formed from the fifth QD layer and above, and propagate through the QD layers. The InAs QDs in the QDSC with HGTSL, as shown in Figure 4.2(c) have a similar density in each layer whereas the QDSC without HGTSL (shown in Figure 4.2(d)) show a decrease in dot density accompanied by an increase in dot size distribution along the growth direction.

The defects observed in the case of the QD structure without HGTSL (Figure 4.2(b)) are due to the formation of incoherent (dislocated) InAs islands. The defects are initially generated around the incoherent islands to form stacked

defects. The threading dislocations originate from these stacked defects and extend through the QD region into the bulk region above.

AFM images from a similar GaAs spacer layer study by Liu *et al.* showed that the growth of GaAs at a low temperature resulted in pits and mounds with average depth and height of 3 ML and 4 ML respectively [5]. However, a higher temperature yielded large ridges with a height of 1 – 2 ML. In addition, a study by Joyce *et al*. showed a similar atomically smooth surface morphology for an annealed GaAs spacer layer and a GaAs buffer layer prior to QD growth [7].

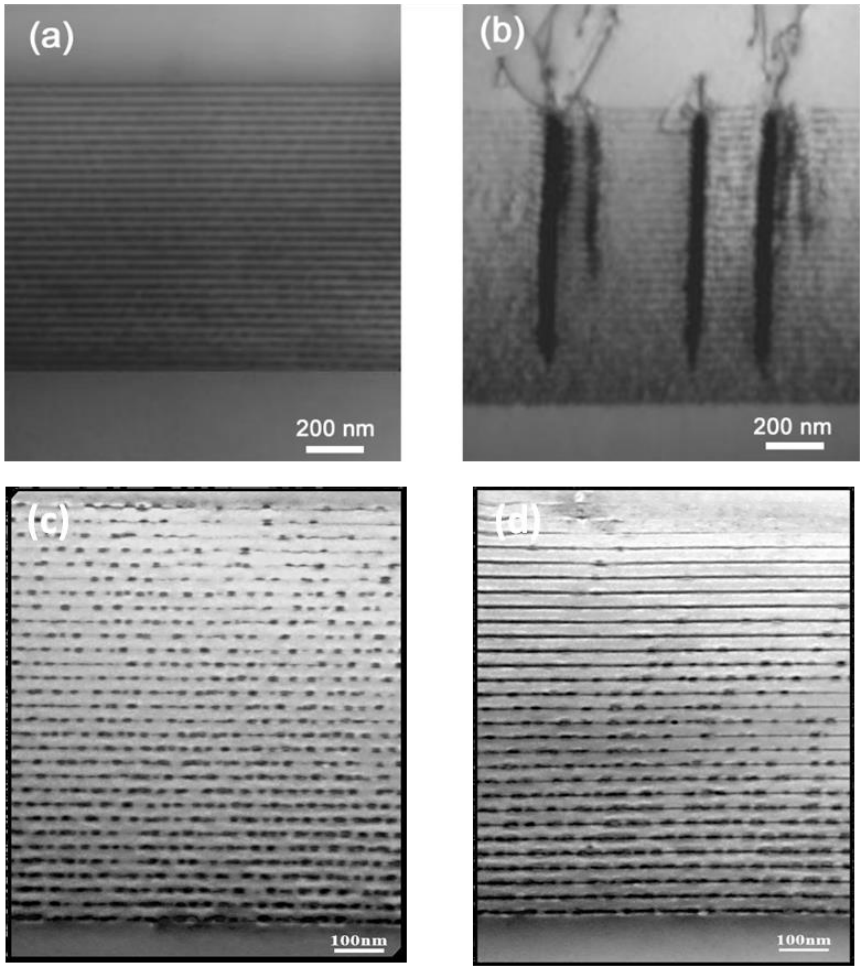

Figure 4.2 Dark field (200) cross-sectional TEM images of 30-layer InAs/GaAs QDSC structures with (a) and without HGTSL (b). Images (c) and (d) show the bright field images under 400BF conditions for the QDSC with and without HGTSL, respectively. The growth direction is in the vertical direction for these images.

The results presented in Figure 4.2 clearly indicate that the formation of threading dislocation in multilayer QD structures is suppressed by the use of HGTSL. This can be qualitatively explained as follows. The surface smoothness of GaAs spacer layer is influenced by the strain field of partly relaxed InAs islands and the mobility of Ga adatoms [8]. For thicker GaAs cap layers, the strain field caused by InAs dots can be negligible, nevertheless it will not be a totally planar surface. The rate of planarization of GaAs surfaces during growth is significantly increased by Ga mobility [9]. The growth of the GaAs spacer layer at high temperatures increases the mobility and migration of Ga adatoms, hence reducing the surface roughness of the GaAs spacer layer.

At lower temperatures, surface roughness will influence the nucleation of the InAs QDs in subsequent layers. Due to a lower local chemical potential, the InAs will begin to nucleate in the pits of the rough surface [9]. As the deposition of InAs continues, these islands grow in size reaching a critical size above which they may become incoherent. The rough GaAs surface in the case of the QD structure without HGTSL hence leads to the nucleation of large sized InAs islands.

It has been shown that the threading dislocations form around the incoherent islands. The threading dislocations then propagate to upper QD layers, and once they are present at the growth surface for QDs, they can act as nucleation sites attracting In atoms and leading to the formation of big incoherent islands. In addition, the strain fields from these large InAs islands can also influence the next QD layer by setting off the formation of another layer of large islands, providing the possibility for the formation of incoherent islands. The QD structure without HGTSL has both coherent and incoherent islands. Once formed, the incoherent islands will rapidly grow in size by attracting In atoms from smaller coherent dots, leading to the reduction in QD density in the QD layers with defected dots [5]. The combined effects of the propagation of the threading dislocation and strain

fields through the structure affects subsequent dot layers by forming vertically aligned incoherent InAs islands, as observed in Figure 4.2(b).

Figure 4.3 shows the 1 × 1 μm^2 AFM image for the uncapped test structure for the QDSC, revealing a QD density of ~ 5.5 × 10^{10} cm^{-2}. The base and height of the InAs QDs are ~25 nm and ~5 nm respectively.

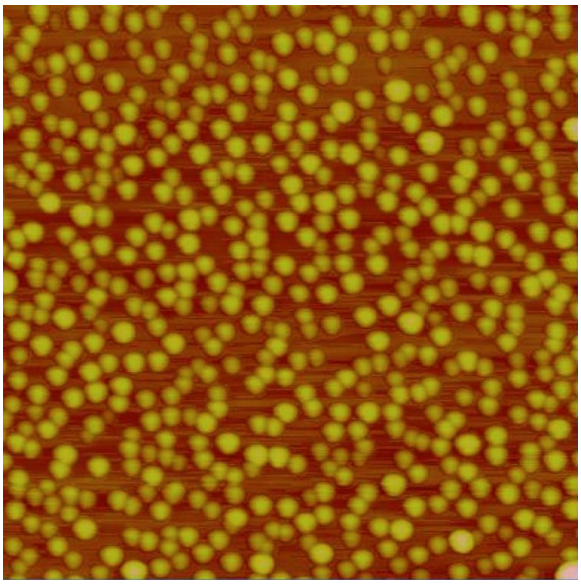

Figure 4.3 AFM image (1 × 1 μm^2) of an uncapped InAs/GaAs quantum-dot sample.

4.2.2 Optical Characterisation

The PL spectral for the 30-layer InAs/InGaAs DWELLs with HGTSL at room temperature (RT) and at 10K is shown in Figure 4.4. The figure also shows the PL for the 30-layer InAs/InGaAs DWELLs grown without HGTSL at 10K.

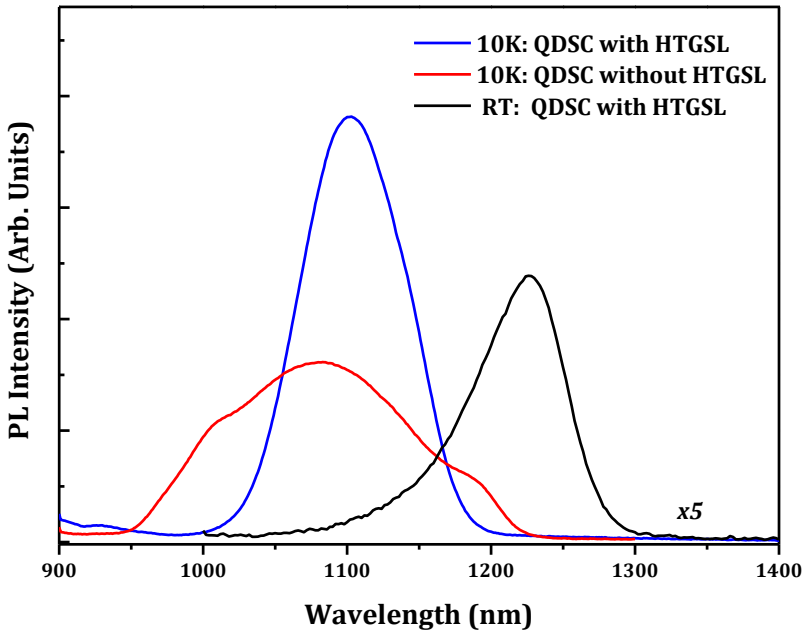

Figure 4.4 The RT and 10 K PL spectral of QDSC sample with HGSTL, and the 10K PL spectrum of QDSC without HGTSL.

At 10K, the PL peak intensity for the HGTSL sample is more than double that of the sample without HGTSL. The emission peak for the HGTSL sample occurs at 1100nm and 1230nm with a full width at half maximum (FWHM) of 90 meV and 60 meV at 10K and RT, respectively. The sample without HGTSL on the other hand has its emission peak at 1080nm with a broader FWHM of 180 meV at 10K. This broader linewidth could be attributed to the increased size distribution of the dots within the QD layer with defected islands. Figure 4.5 shows the temperature dependent PL for the QDSCs with and without HGTSL measured from 10K to 300K. As the temperature is increased, the PL intensity drops faster for the QDSC without HGTSL. There was also no PL emission observed for the QDSC without HGTSL at RT.

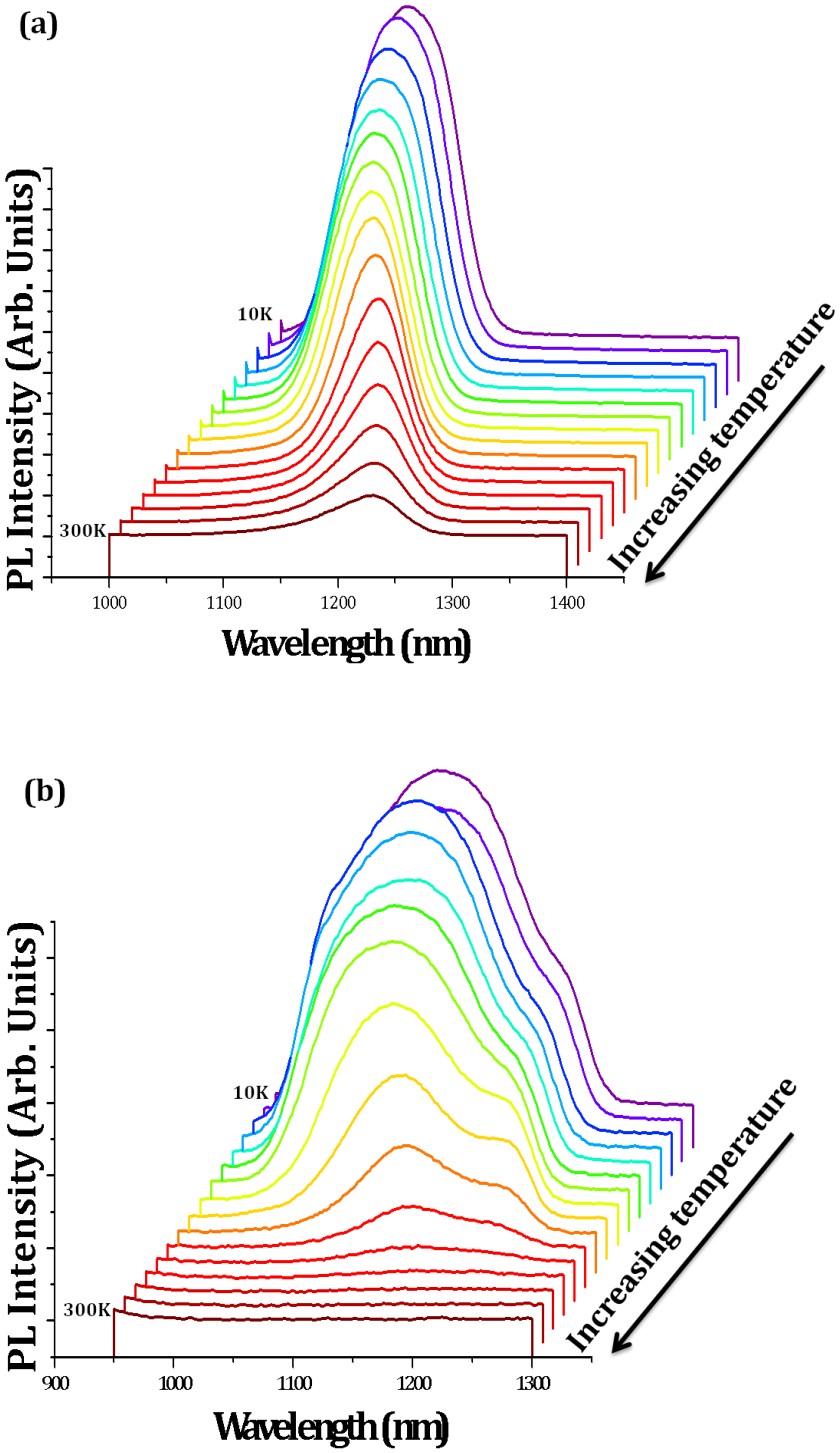

Figure 4.5 Temperature dependent PL for the samples with HGTSL (a) and without HGTSL (b) measured from 10K to 300K. (PL is taken at 10K and 20K. Then in increments of 20K to 300K)

The capture of carriers in the InAs/InGaAs DWELL structures occurs by a two-stage process. Since the PL measurements are nonresonant, carriers are photogenerated in the GaAs barrier. After relaxing to the GaAs band edge, carriers are captured into the InGaAs QW buffer/capping states and then from the InGaAs QW buffer/capping states into the QDs [10]. It has been shown that both the capture and relaxation of electrons to QD states occurs with a picosecond time scale (~ 2.5 ps) [11]. After the capture of carriers in QD states, they may radiatively recombine or escape. Escaped carriers can be nonradiatively recombined at defects sites. The lack of a detectable PL emission at RT for the QDSC without HGTSL, confirms the occurrence of nonradiative recombination due to defects as observed in Figure 4.2 (b).

To further investigate the effects of HGTSL on the optical properties of 30-layer InAs/GaAs QDs, the temperature dependent PL data was fitted to an Arrhenius equation (Equation 4.1). This empirical equation describes the relationship between PL intensity and temperature as: [12]

$$I = \frac{I_0}{1 + C_1 e^{-\frac{E_1}{kT}}} \qquad \textbf{4.1}$$

where I is PL intensity, I_0 is PL intensity at 0 K, E_1 is thermal activation energy, k is the Boltzmann constant, T is the temperature and C_1 is a fitting constant. The constant would account for the recombination rates and geometric dimensions of the QDs, in a physical model [13]. Figure 4.6 shows the PL intensity against inverse temperature. The slopes of the line at high temperatures (220 – 300 K) yield thermal activation energies of 194 ± 8 meV and 160 ± 11 meV for the QDSCs with and without HGTSL, respectively. The activation energy corresponds to the effective confinement energy for carriers in the QDs [14]. In the case of the InAs/InGaAs DWELL structure, these values for the thermal activation energy, refer to the energy separation between the QD ground state and InGaAs QW states [15]. Figure 4.6 also shows that the onset of thermal quenching in the QDSC without HGTSL begins at 120K as compared to 180K in the QDSC with HGTSL. At these quenching threshold temperatures, carrier thermal escape begins to play an

important role in carrier dynamics. It is then that carriers in the InAs QDs have enough energy to overcome the InGaAs QW barrier. Thermal escape of carriers also occurs by a two-stage process; from QD states into the InGaAs QW buffer/capping states and then into the GaAs barrier. Figure 4.7 presents a schematic band diagram of the InAs/InGaAs DWELL structure showing the capture and escape of carriers.

At temperatures below 80K, the processes of carrier thermal escape from the QD into the QW and from the QW into the GaAs layer are negligible [16]. As a result, the PL intensity in the low temperature range remains relatively constant. These results clearly show that the HGTSL technique, applied to the growth of solar cells can produce a cell that is more resilient to carrier thermal escape at high temperatures.

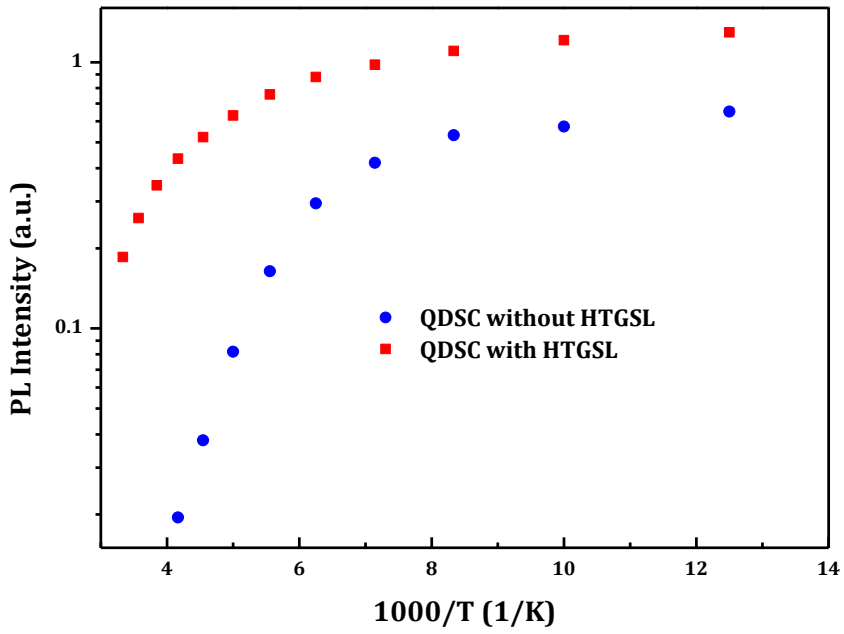

Figure 4.6 Arrhenius plots of temperature dependent PL for the QDSCs with and without HGTSL.

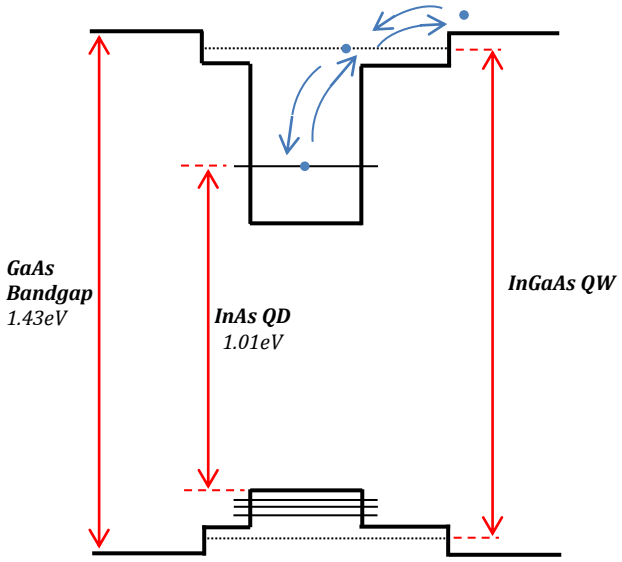

Figure 4.7 Schematic of energy band diagram of InAs/InGaAs DWELL structure

4.2.3 Solar Cell Performances

Figure 4.8 shows the 1 sun AM1.5 *J-V* characteristics of the QDSCs with and without HGTSL and the GaAs reference cell. Table 4.1 presents the short-circuit current density (J_{SC}), the open-circuit voltage (V_{OC}), the fill factor (*FF*) and the efficiency (η) of the three solar cells. The efficiency of both QDSCs is degraded compared to the reference GaAs SC. This reduction of efficiency in both cases of the QDSCs, with and without HGTSL, is likely due to the fact that carrier lifetime in QDs is smaller than in bulk GaAs [17]. The power generated by the QDSC without HGTSL is very small compared to the QDSC with HGTSL. The huge drop in V_{OC} and J_{SC} for QDSC without HGTSL can be attributed to the poor structural quality and hence the increase in non-radiative recombination as evident by Figure 4.2(b), in which threading dislocations run through the QD layers and into the p-doped GaAs emitter. The use of the HGTSL technique in the growth of the QDSC results in the V_{OC} increasing to 0.71 V and an increase in J_{SC} to 20.17 mA/cm^2, which is higher than that of the reference GaAs SC (19.53 mA/cm^2).

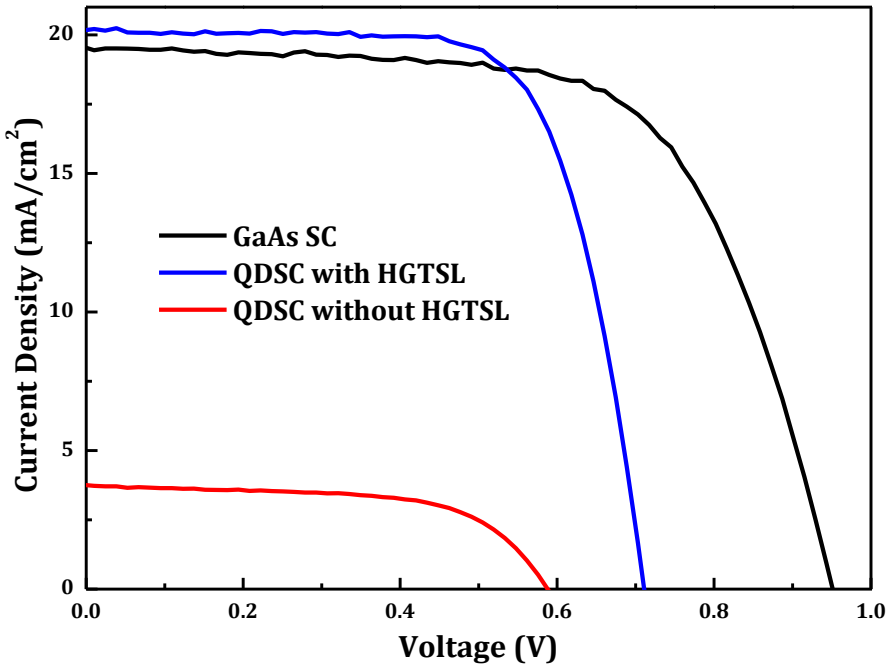

Figure 4.8 1 sun AM1.5 current density vs. voltage curves and InAs/GaAs QDSCs with and without HGTSL, and the reference GaAs solar cell.

Solar Cells	J_{SC} (mA/cm^2)	V_{OC} (V)	*FF* (%)	η (%)
GaAs Reference Cell	19.53	0.95	65	12.04
QDSC with HGTSL	20.17	0.71	71	10.12
QDSC without HGTSL	3.75	0.59	62	1.36

Table 4.1 Short-circuit current (*Jsc*), open-circuit voltage (*Voc*), fill factor (*FF*), and efficiency (η) for QDSC with and without HGTSL, and GaAs SC under 1 sun AM1.5 illumination.

In comparison with GaAs SC, the reduction in V_{OC} for QDSCs is not only due to an increase in minority carrier recombination caused by the QD region, but also due to the reduction of the effective bandgap of the solar cell with the introduction of InGaAs QWs. The EQE measurements shown in Figure 4.9 give further insight into the absorption qualities of the solar cells. It shows the GaAs SC with a drop at ~870 nm, indicating that absorption of photons is

taking place only above the bandgap of GaAs. The QDSCs absorbed photons with energies below the GaAs bandgap up to ~1240 nm due to the absorption of lower energy photons through the QDs. The QDSC without HGTSL shows a massive loss of quantum efficiency above the GaAs bandgap, which far outweighs the increase below the GaAs bandgap. The QDSC with HGTSL on the other hand did not show degradation of the EQE above the GaAs bandgap, hence leading to a higher J_{SC} than that of GaAs SC. Furthermore, the QDSC without HGTSL shows a greater absorption below the GaAs bandgap compared to the QDSC with HGTSL.

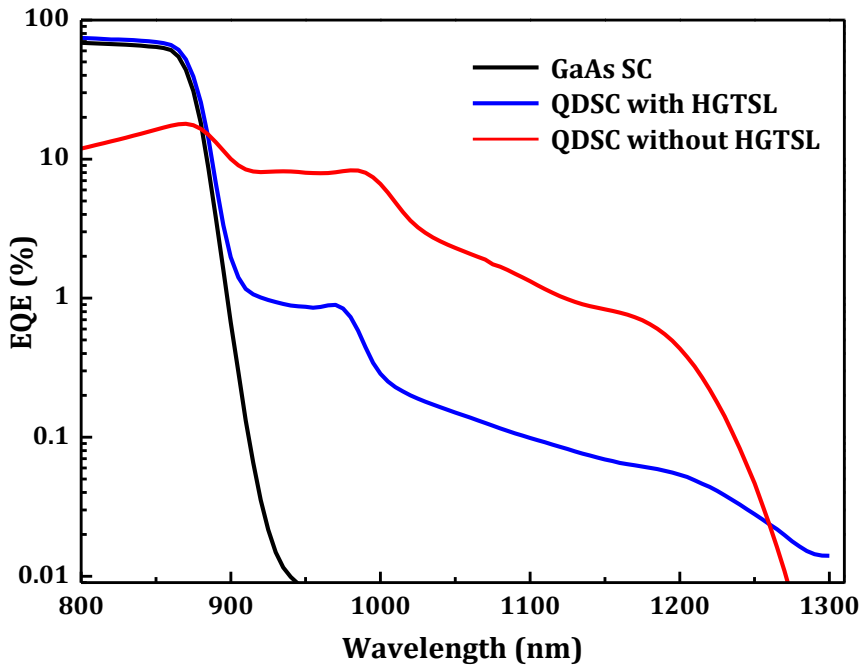

Figure 4.9 External quantum efficiency of InAs/GaAs QDSCs with and without the HGTSL, and the reference GaAs solar cell.

To investigate the fact that the QDSC without HGTSL has a greater absorption in the long-wavelength region (above 870nm) compared to the QDSC with HGTSL, temperature-dependent measurements of the 1-sun AM1.5 *J-V* characteristics and EQE of the QDSCs were performed. Figure 4.10 shows the *J-V* characteristics of the QDSCs as a function of temperature from 77K to 300K. As the temperature is increased, the V_{OC} of both of the QDSCs decrease.

An increase in temperature results in a reduction in the semiconductor bandgap due to thermal expansion of the crystal lattice. Since the V_{OC} of a solar cell is equal to the difference between quasi-Fermi levels of the valence band and the conduction band (divided by the electron charge), the reduction in the bandgap corresponds to a reduction in the V_{OC}. It is clear that the temperature effects of these two QDSCs are the same given that for increasing temperature the V_{OC} of both QDSCs decrease at the same rate.

Owing to the reduced semiconductor bandgap of the QDSC devices with increasing temperature, an increase in the J_{SC} is expected. This is because there will be an increase in photon absorption due to the smaller bandgap. The J_{SC} for the QDSC with HGTSL shows a slight increase with increasing temperature.

While the QDSC with HGTSL shows only small linear increases in J_{SC}, the QDSC without HGTSL on the other hand, shows a steady increase in J_{SC} at low temperatures, until ~ 200K after which there are significant large increases. This suggests that at a certain threshold temperature for the QDSCs without HGTSL, there is a release of trapped carriers that contributes to the photocurrent.

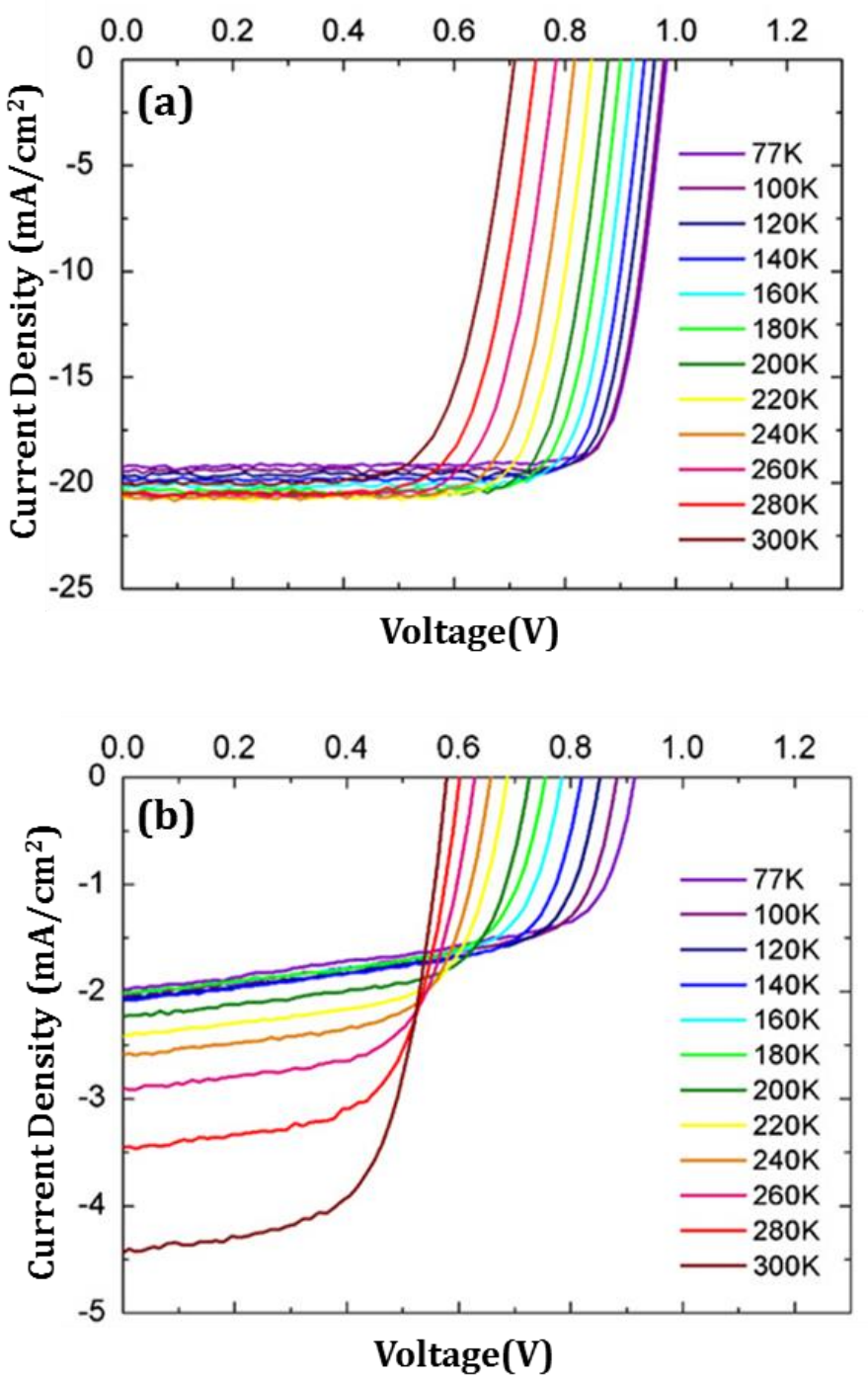

Figure 4.10 *J-V* characteristics as a function of temperature for (a) QDSC with HGTSL and (b) QDSC without HGTSL

Figure 4.11 shows the EQE as a function of the temperature for the QDSCs from 77K to 300K. Also shown in Figure 4.11 are the PL spectra at 77K for the QDSCs. The contributions of the GaAs barrier, InGaAs QW and the InAs QDs to the EQE and PL are also displayed.

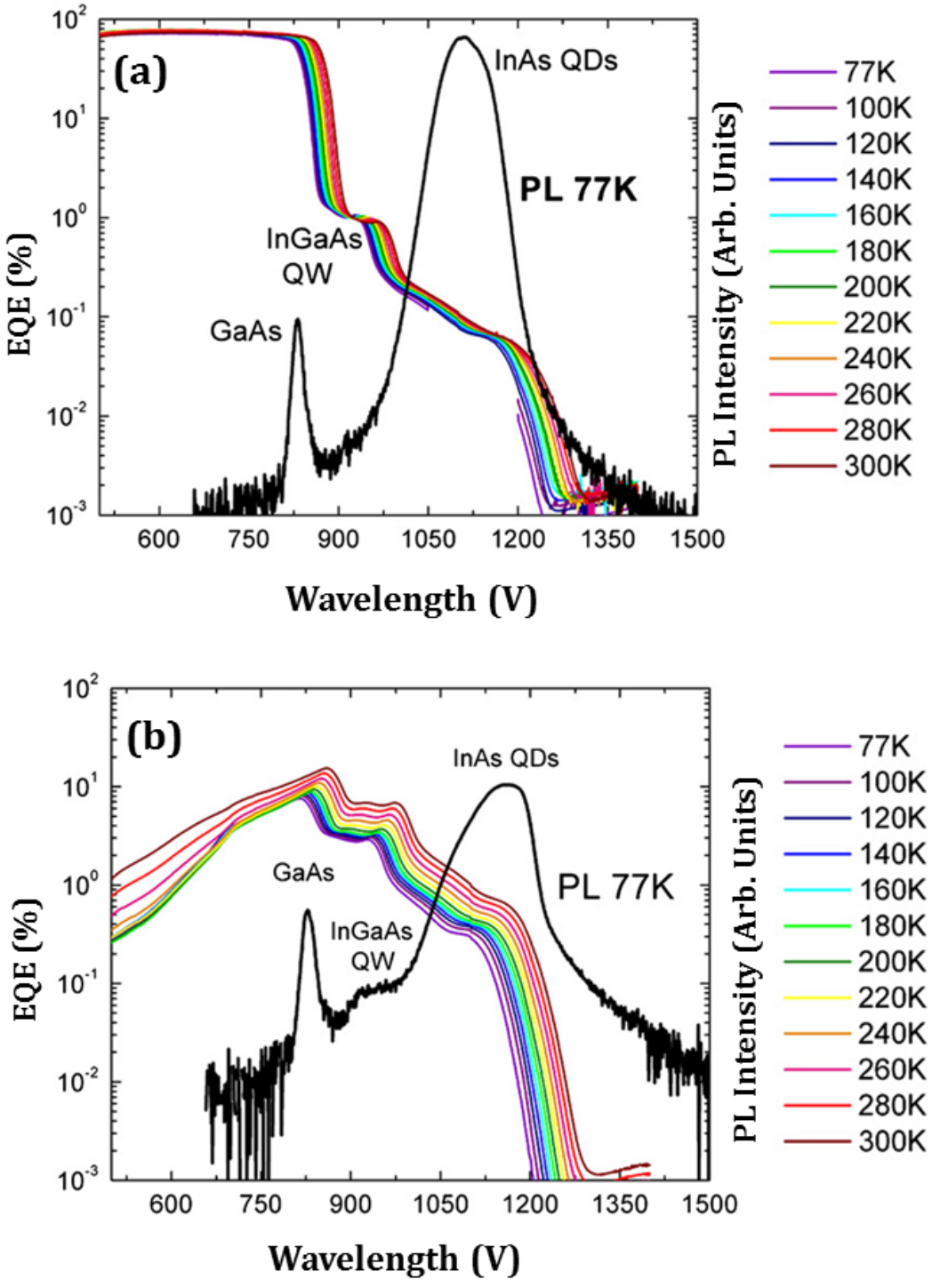

Figure 4.11 EQE as a function of temperature for (a) QDSC with HGTSL and (b) QDSC without HGTSL. Also shown are the PL spectra at 77K for the QDSCs.

As shown in Figure 4.11(a), for the QDSC with HGTSL, at wavelengths above the bandgap of GaAs, temperature has little effect on the EQE, however at sub-bandgap wavelengths there is a slight increase in EQE. In contrast, for the QDSC without HGTSL, there is a significant increase in the sub-bandgap EQE as temperature is increased. At shorter wavelengths, the QDSC without HGTSL only shows significant increases after ~220K. Again, this behaviour suggests that the dislocations and defects present in the QDSC without HGTSL aid the extraction of carriers from the QD states. The non-radiative recombination centres formed by the defects in the QDSC without HGTSL enhances carrier extraction by defect mediated tunneling processes [18]. This defect mediated carrier extraction that explains the greater EQE for the QDSC without HGTSL compared to the QDSC with HGTSL observed in Figure 4.9.

4.3 Conclusion

In this chapter, the effects of temperature on the GaAs spacer layer in QD structures and QDSCs were investigated. QD structures grown with a low GaAs spacer temperature layer (510 ^{o}C), resulted in incoherent islands with threading dislocations. It was shown that the defect formation in 30-layer InAs/GaAs QD structures can be significantly suppressed by the use of a high-growth-temperature GaAs spacer layer (HGTSL). The incorporation of the HGTSL results in a significant increase in the short-circuit current for a 30-layer InAs/GaAs QDSC with absorption at ~1.0 eV compared to the QDSC without HGTSL.

Bibliography

[1] A. Stintz, G. T. Liu, and H. Li, "Low-threshold current density 1.3-μm InAs quantum-dot lasers with the dots-in-a-well (DWELL) structure," *IEEE Photonics Technol. Lett.*, vol. 12, no. 6, pp. 591–593, 2000.

[2] T. Gu, M. A. El-Emawy, K. Yang, A. Stintz, and L. F. Lester, "Resistance to edge recombination in GaAs-based dots-in-a-well solar cells," *Applied Physics Letters*, vol. 95, no. 26. p. 261106, 2009.

[3] K. Nishi, H. Saito, S. Sugou, and J. Lee, "A narrow photoluminescence linewidth of 21 meV at 1.35 μm from strain-reduced InAs quantum dots covered by In[sub 0.2]Ga[sub 0.8]As grown on GaAs substrates," *Appl. Phys. Lett.*, vol. 74, no. 8, p. 1111, 1999.

[4] H. Y. Liu, M. Hopkinson, C. N. Harrison, M. J. Steer, R. Frith, I. R. Sellers, D. J. Mowbray, and M. S. Skolnick, "Optimizing the growth of 1.3 μm InAs/InGaAs dots-in-a-well structure," *J. Appl. Phys.*, vol. 93, no. 5, pp. 2931–2936, 2003.

[5] H. Y. Liu, I. R. Sellers, M. Gutiérrez, K. M. Groom, W. M. Soong, M. Hopkinson, J. P. R. David, R. Beanland, T. J. Badcock, D. J. Mowbray, and M. S. Skolnick, "Influences of the spacer layer growth temperature on multilayer InAs/GaAs quantum dot structures," *J. Appl. Phys.*, vol. 96, no. 4, p. 1988, 2004.

[6] D. Guimard, R. Morihara, D. Bordel, K. Tanabe, Y. Wakayama, M. Nishioka, and Y. Arakawa, "Fabrication of InAs/GaAs quantum dot solar cells with enhanced photocurrent and without degradation of open circuit voltage," *Appl. Phys. Lett.*, vol. 96, no. 20, p. 203507, 2010.

[7] P. B. Joyce, T. J. Krzyzewski, P. H. Steans, G. R. Bell, J. H. Neave, and T. S. Jones, "Variations in critical coverage for InAs/GaAs quantum dot formation in bilayer structures," *J. Cryst. Growth*, vol. 244, no. 1, pp. 39–48, Sep. 2002.

[8] H. Y. Liu, B. Xu, Y. H. Chen, D. Ding, and Z. G. Wang, "Effects of seed layer on the realization of larger self-assembled coherent InAs/GaAs quantum dots," *J. Appl. Phys.*, vol. 88, no. 9, p. 5433, 2000.

[9] G. Biasiol and E. Kapon, "Mechanisms of Self-Ordering of Quantum Nanostructures Grown on Nonplanar Surfaces," *Phys. Rev. Lett.*, vol. 81, no. 14, pp. 2962–2965, Oct. 1998.

[10] J. L. C. Espinola, M. Dybic, S. Ostapenko, T. V. Torchynska, and G. Polupan, "Carrier dynamics in InAs quantum dots embedded in InGaAs/GaAs multi quantum well structures," in *Journal of Physics: Conference Series*, 2007, vol. 61, pp. 180–184.

[11] T. Müller, F. F. Schrey, G. Strasser, and K. Unterrainer, "Ultrafast intraband spectroscopy of electron capture and relaxation in InAs/GaAs quantum dots," *Appl. Phys. Lett.*, vol. 83, no. 17, p. 3572, 2003.

[12] Y. Wu, K. Arai, and T. Yao, "Temperature dependence of the photoluminescence of ZnSe/ZnS quantum-dot structures.," *Phys. Rev. B. Condens. Matter*, vol. 53, no. 16, pp. R10485–R10488, Apr. 1996.

[13] L. Chen, V. G. Stoleru, D. Pan, and E. Towe, "Enchanced 1 . 3-mm-emission from InAs quantum dots embedded in symmetric (In , Ga) As quantum-well structures," *J. Cryst. Growth*, vol. 242, pp. 263–269, 2002.

[14] K. Y. Ban, W. Hong, S. P. Bremner, S. N. Dahal, H. McFelea, and C. B. Honsberg, "Controllability of the subband occupation of InAs quantum dots on a delta-doped GaAsSb barrier," *J. Appl. Phys.*, vol. 109, no. 1, p. 014312, 2011.

[15] R. Chen, H. Y. Liu, and H. D. Sun, "Electronic energy levels and carrier dynamics in InAs/InGaAs dots-in-a-well structure investigated by optical spectroscopy," *J. Appl. Phys.*, vol. 107, no. 1, p. 013513, 2010.

[16] T. V. Torchynska, J. L. Casas Espinola, L. V. Borkovska, S. Ostapenko, M. Dybiec, O. Polupan, N. O. Korsunska, a. Stintz, P. G. Eliseev, and K. J. Malloy, "Thermal activation of excitons in asymmetric InAs dots-in-a-well In[sub x]Ga[sub 1−x]As/GaAs structures," *J. Appl. Phys.*, vol. 101, no. 2, p. 024323, 2007.

[17] D. Alonso-Alvarez, A. G. Taboada, J. M. Ripalda, B. Alen, Y. Gonzalez, L. Gonzalez, J. M. Garcia, F. Briones, A. Marti, A. Luque, A. M. Sanchez, and S. I. Molina, "Carrier recombination effects in strain compensated quantum dot stacks embedded in solar cells," *Appl. Phys. Lett.*, vol. 93, no. 12, p. 123114, 2008.

[18] S. M. Willis, J. A. R. Dimmock, F. Tutu, H. Y. Liu, M. G. Peinado, H. E. Assender, A. a. R. Watt, and I. R. Sellers, "Defect mediated extraction in InAs/GaAs quantum dot solar cells," *Sol. Energy Mater. Sol. Cells*, pp. 1–6, Apr. 2012.

Chapter 5

InAs/GaAs quantum dot solar cells with an AlAs Cap Layer

It is well established that in InAs/GaAs quantum dot solar cells (QDSC), the QDs extend the absorption spectrum to lower energy photons, and hence increasing the short-circuit current (J_{sc}). However, this increase in J_{sc} is usually accompanied by a significant decrease in open-circuit voltage (V_{oc}), leading to a drop in the efficiency of the QDSCs in comparison to its reference GaAs SC. In general, this drop in V_{oc} is due to the reduction in transition energy between the valence band (VB) and the conduction band (CB) of the cell. The decrease in the effective bandgap of the QDSCs is due to (i) the wetting layer (WL) forming continuous energy levels below the CB, and (ii) the closely packed confined energy levels of holes within the VB [1]. In this chapter, the effect of an AlAs cap layer (CL) above InAs/GaAs QDs on V_{oc} of InAs/GaAs QDSCs is presented. Transmission electron microscope (TEM) images and external quantum efficiency (EQE) measurements clearly indicate the absence of the WL in the InAs/GaAs QDSC with AlAs CL. The absence of the WL leads to an enhanced V_{oc} for InAs QDSC with AlAs CL compared to a reference InAs/GaAs QDSC without AlAs CL. The implications for the design and implementation of QD IBSCs are also discussed in this chapter.

5.1 Experimental Work

5.1.1 Growth Details

The molecular beam epitaxy (MBE) growth procedure for this group of cells was similar to that described for the InAs/InGaAs DWELL solar cell structures in Chapter 4. Three SC samples, two QDSCs and a reference GaAs SC were grown by MBE on an n-type GaAs (100) substrate. The GaAs reference cell, which has a *p-i-n* structure consists of a 200 nm *n*-GaAs buffer layer, 30 nm *n*-$Al_{0.33}Ga_{0.67}As$ window, 300 nm *n*-GaAs base, 400 nm undoped GaAs, 250 nm *p*-GaAs emitter, 30 nm *p*-$Al_{0.75}Ga_{0.25}As$ window and 250 nm p^+-GaAs contact layer. The two QDSCs have the same structure as the GaAs SC except that a 20-layer InAs/GaAs QD structure is inserted in the intrinsic region instead of bulk GaAs. The thickness of the QD region was kept at 400 nm as in the GaAs reference cell. The QD layers consist of 2.1 monolayers (ML) of InAs capped by 20 nm of GaAs, which separates the QD layers. For one of the QDSCs, the formation of the InAs QDs was immediately followed by the deposition of a 2 ML AlAs cap layer (CL). The high growth temperature spacer layer technique [2], discussed in Chapter 4 was used in the growth of these QDSCs. A Nanosurf Easyscan2 atomic force microscope (AFM) was used to image uncapped test structures. Figure 5.1 shows a schematic of the epitaxial structure of the InAs/GaAs QDSC with AlAs CL.

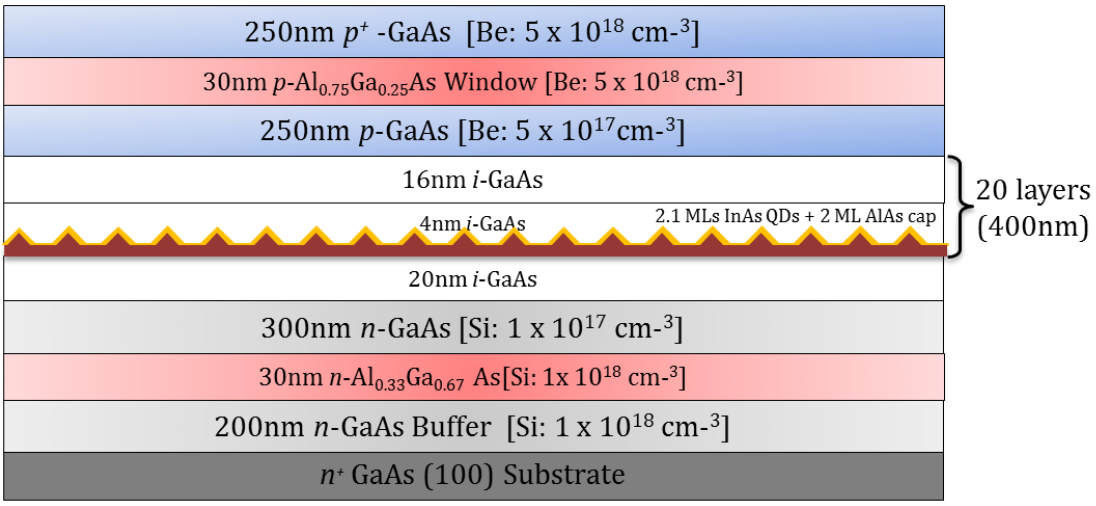

Figure 5.1 Schematic of the QDSC with AlAs CL.

5.1.2 Device Processing and Characterisation

The metal contacts used in fabrication were Au-Zn-Au for the *p* contact and AuGe-Au for the *n* contact. The current density – voltage characteristics were measured using a solar simulator at room temperature (RT) under 1 sun AM1.5 illumination. The external quantum efficiency (EQE) for the SCs was also obtained at room temperature and at zero bias. Photoluminescence (PL) measurements were obtained in a close-cycle He cryostat under 532 nm excitation from a diode-pumped solid-state laser. A 0.25 m monochromator was used to disperse the PL spectra, which was then detected by a TE-cooled Ge detector. Temperature dependent PL measurements were taken from 10 to 300 K at a laser power of 60 mW.

5.2 Results and Discussion

5.2.1 Structural Characterisation

The AFM image of the uncapped test structures is shown in Figure 5.2, which reveals the InAs QD density to be approximately 4.8 *x* 10^{10} cm^{-2}. The base and height of the InAs QDs are found to be ~ 30 nm and ~ 9 nm respectively.

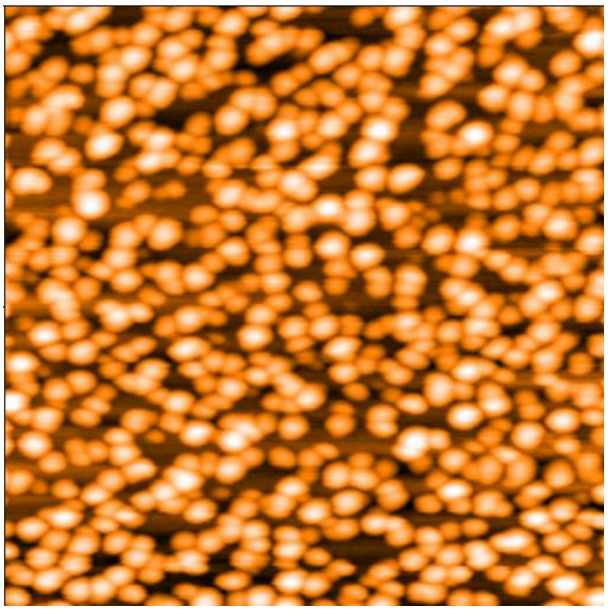

Figure 5.2 AFM image (1 × 1 μm²) of an uncapped quantum-dot sample.

The cross-sectional TEM images for the InAs/GaAs QDSC with AlAs CL and the reference QDSC without AlAs CL are shown in Figure 5.3. Figure 5.3 (a) and (b) show the cross section of the entire solar cell structures for the reference QDSC and the QDSC with AlAs CL respectively. It shows that both QDSCs have good structural quality, with no threading dislocations in the base, *i*-region or emitter. The white streaks between the QDs in Figure 5.3 (d) and (f) can be attributed to the AlAs deposited, confirming the absence of an InAs WL. The InAs QDs exhibit a lens-shaped cross-section, with a base length and height of ~15 nm and ~5 nm for the QDs without AlAs CL, as shown in Figure 5.3 (c) and (e). From Figure 5.3 (f) is can be seen that the QDs for the QDSC with AlAs CL has changed significantly compared to the dots without AlAs CL. The base and height of the InAs QDs with AlAs CL show an increase to ~20 nm and ~7 nm respectively. These values of QD sizes are smaller than those measured from the AFM image. It has been shown that the dot height for capped QDs is smaller than that of uncapped QDs, because of a net migration of In atoms away from the InAs QDs during the GaAs capping process [3].

When InAs QDs are capped with GaAs, there is a tendency for the Ga adatoms to migrate away from the top of the dots because of the strain [4], hence the initial GaAs layers cover the region between InAs QDs. This leads to an increase in the strain at the edge of the QDs. This increase in strain causes In atoms to migrate from the QDs to the WL region, hence the reduction in QD size. The segregation of In atoms leads to alloy intermixing and formation of InGaAs in the region between dots, which is shown as the dark region between InAs QDs in Figure 5.3 (e). On the other hand, if the InAs QDs are capped by AlAs, there is an accumulation of Al atoms on top of the QDs. Since the mobility of Al atoms is much smaller than that of In and Ga atoms, the In atoms in the WL are substituted by Al atoms [5]. This results in a reduced strain at the edges of the QDs, which in turn reduces the In atom migration. The reduction in In atom migration away from the dots explains the larger QD size in the case of the AlAs CL, and hence the absence of InGaAs layer between InAs QDs in Figure 5.3 (f) [6].

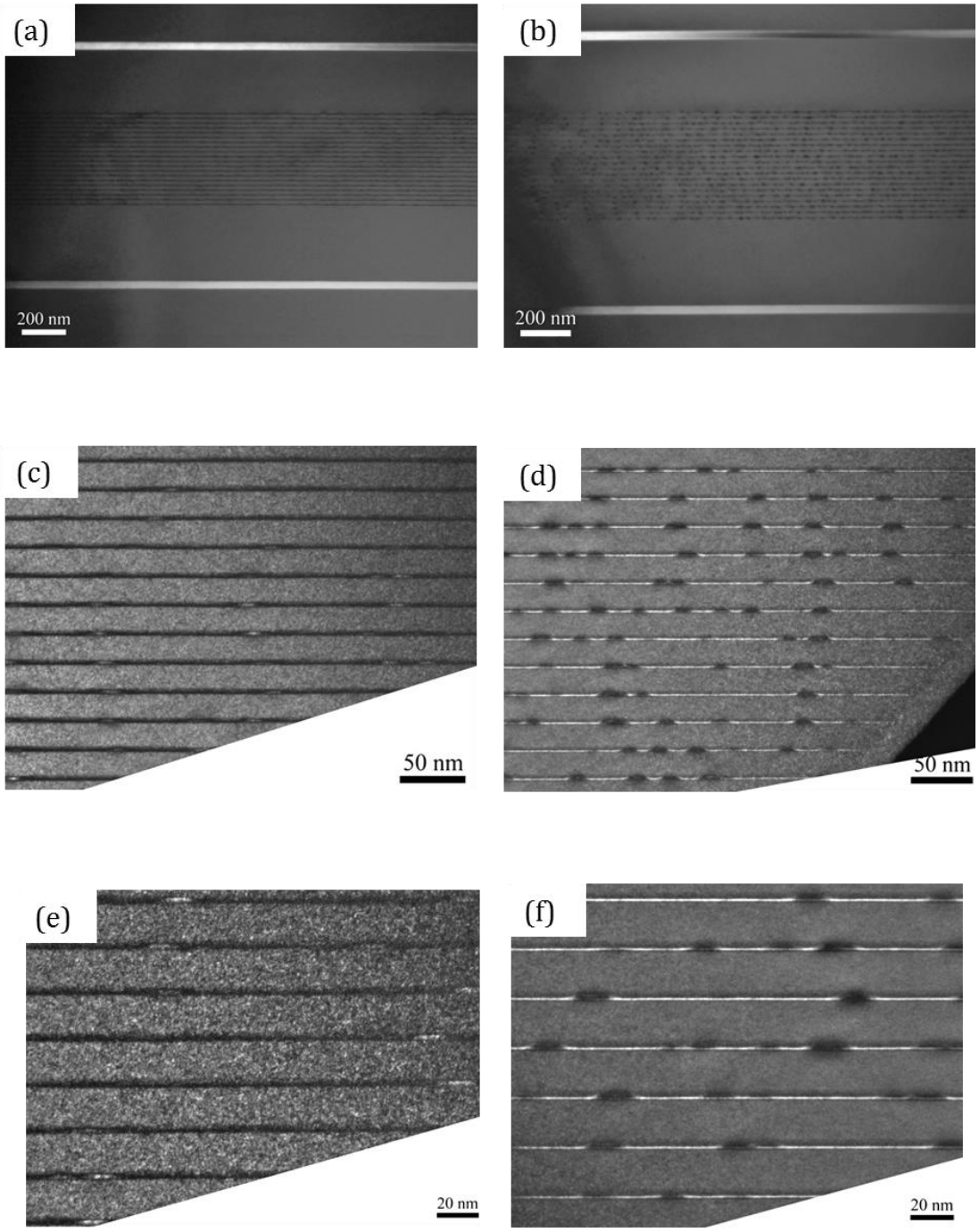

Figure 5.3 Dark field (200) cross-sectional TEM images of the entire InAs/GaAs QDSC structures (a) without and (b) with AlAs CL. (c) and (e) show the QD region for the reference QDSC without AlAs CL, whereas (d) and (e) show the QD region for the QDSC with AlAs CL. The growth direction is in the vertical direction for these images.

5.2.2 Optical Characterisation

The optical properties of InAs/GaAs QDSCs with and without AlAs were compared. Figure 5.4 shows the PL spectra for the QDSCs at RT. The PL peak intensity for the QDSC with AlAs CL is more than double that of the reference QDSC without AlAs CL. The emission peaks for the QDSCs with and without AlAs CL occurs at 1090 nm and 1078 nm respectively. The increase in QD height and volume in the QDSC with AlAs CL is reflected in the PL measurements by the slight redshift of the peak intensity.

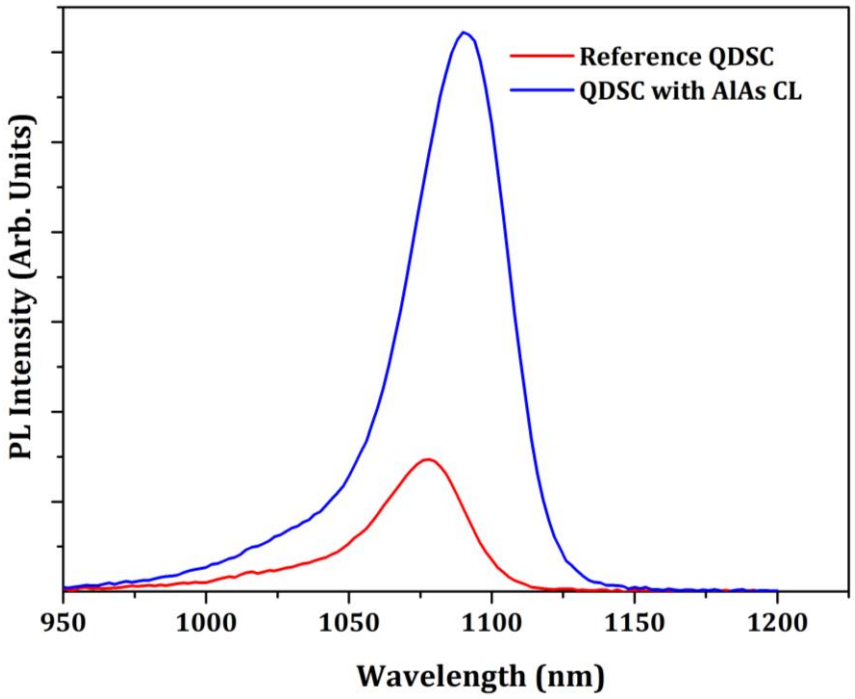

Figure 5.4 PL spectra of the QDSCs at RT.

The full width at half maximum (FWHM) for both emission peaks is ~42 meV. The similar linewidth for both QDSCs shows that the AlAs CL does not affect the size distribution of the QDs. To further investigate the effect of the AlAs CL on the optical properties of the QDs, the temperature-dependent PL measurements were acquired. Figure 5.5 shows the temperature-dependent PL for the QDSCs measured from 10 K to 300 K. Since nonresonant excitation (532nm laser) was used for these PL measurements, carrier transfer from continuum states into QD states plays a vital role in the carrier dynamics.

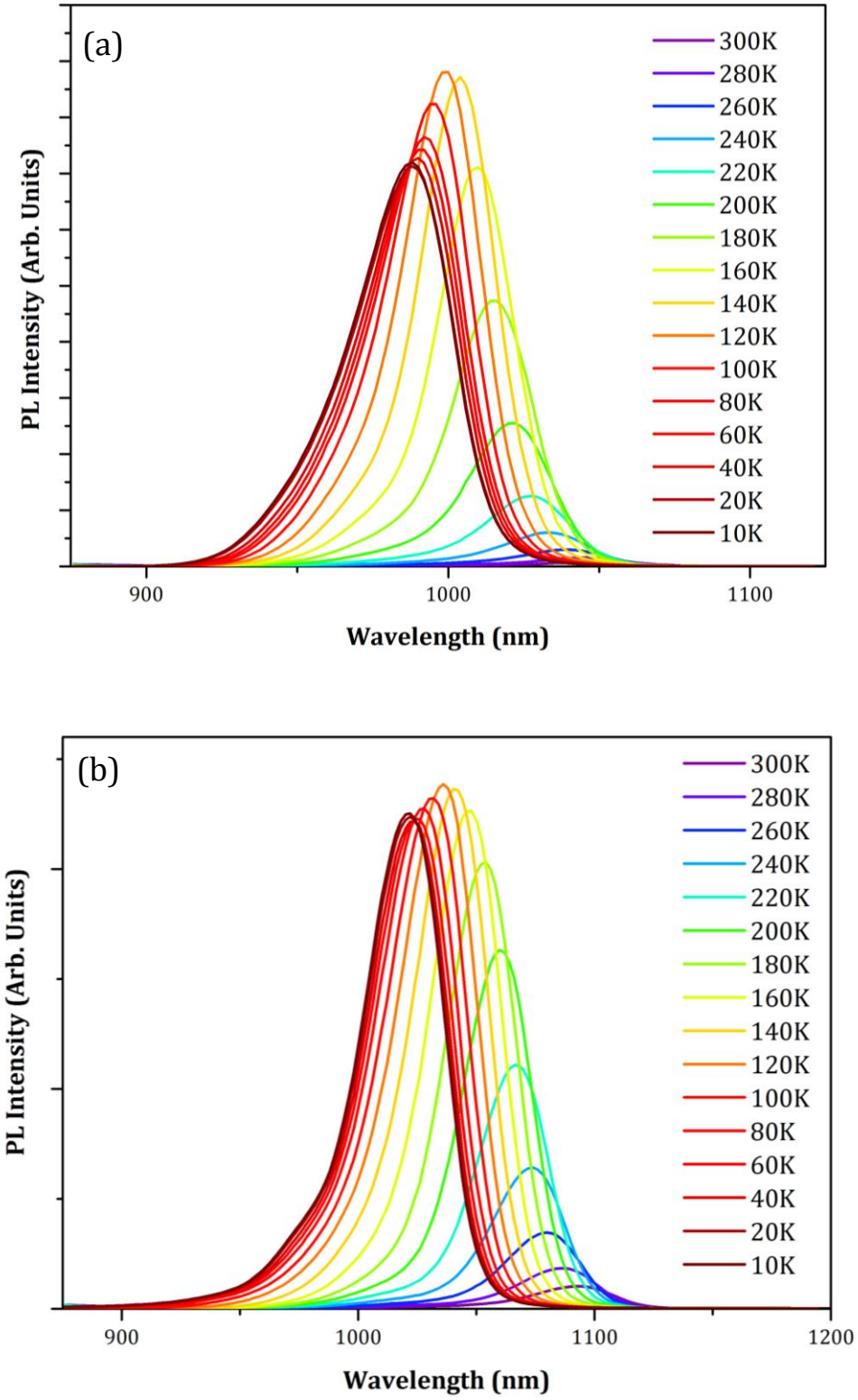

Figure 5.5 Temperature dependent PL for the reference QDSCs (a) and the QDSC with AlAs CL (b) measured from 10K to 300K. (PL is taken at 10K and 20K. Then in increments of 20K to 300K).

In an InAs/GaAs QD system, the optically excited carriers in the GaAs barrier relax to the edge of the CB continuum and then to the WL and finally become trapped in the QD states. This is the way the QD states are population in both the reference QDSC and the QDSC with AlAs CL. Typical times of carrier transfer is faster compared to radiative recombination lifetime (~1 ns) [7] of carriers in QD states. As previously mentioned, carriers in QD states only radiatively recombine or escape. Escaped carriers either undergo nonradiatively recombined at defects sites or are recaptured by other QDs, resulting in interdot carrier transfer. Yu *et. al* [8] have shown that with a GaAs spacer layer as thick as 20nm, there will be a decreased vertical electronic coupling between QD layers. As such, it can be assumed that the effect of lateral coupling is greater than vertical coupling in the QD structures.

The integrated PL intensity was also compared for the QDSCs, as shown in Figure 5.6. It is observed that at low temperatures, the PL intensities of the QDSCs are comparable. However, at higher temperatures (above 180 K), the PL intensity of the QDSC with AlAs CL is stronger than the QDSC without AlAs CL. This shows that placing an AlAs CL on the QDs has led to less carrier escape at high temperatures.

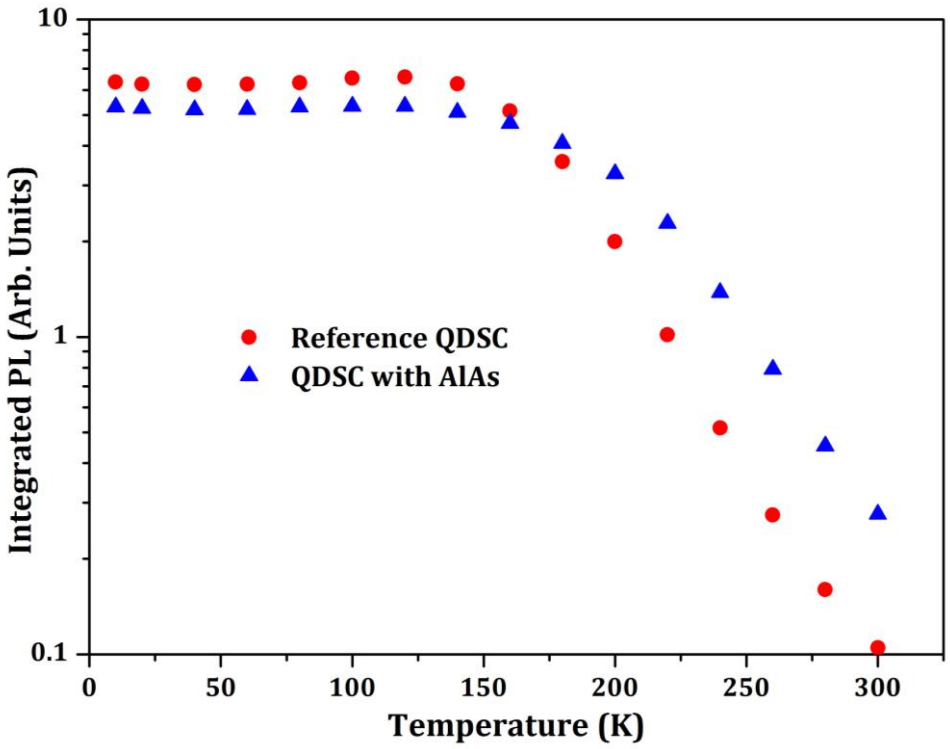

Figure 5.6 Comparison of the temperature dependence of the PL efficiency of the QDSC with and without AlAs CL

Fitting Arrhenius curves to the temperature dependant PL data (180 – 300 K) yields thermal activation energies of 200 ± 20 meV for the QDSC without AlAs CL and 270 ± 25 meV for the QDSC with AlAs. The 200 meV activation energy of the QDSC without AlAs CL is similar to the energy separation between the QD ground state and the WL (~202 meV). In the case of the QDSC with AlAs CL, the 270 meV activation energy is close to the energy separation between the QD ground state and the edge of the GaAs bandgap (~280 meV). The greater thermal activation energy for the QDSC with AlAs CL indicates that there is an increase in carrier confinement potential [9]. This points to what was observed in Figure 5.3 (f); the AlAs CL has led to removal of the WL, and without the WL the energy separation between the electronic sub-band levels of the QDs and the continuum states in the CB has increased, hence the increase of ~70 meV in thermal activation energy.

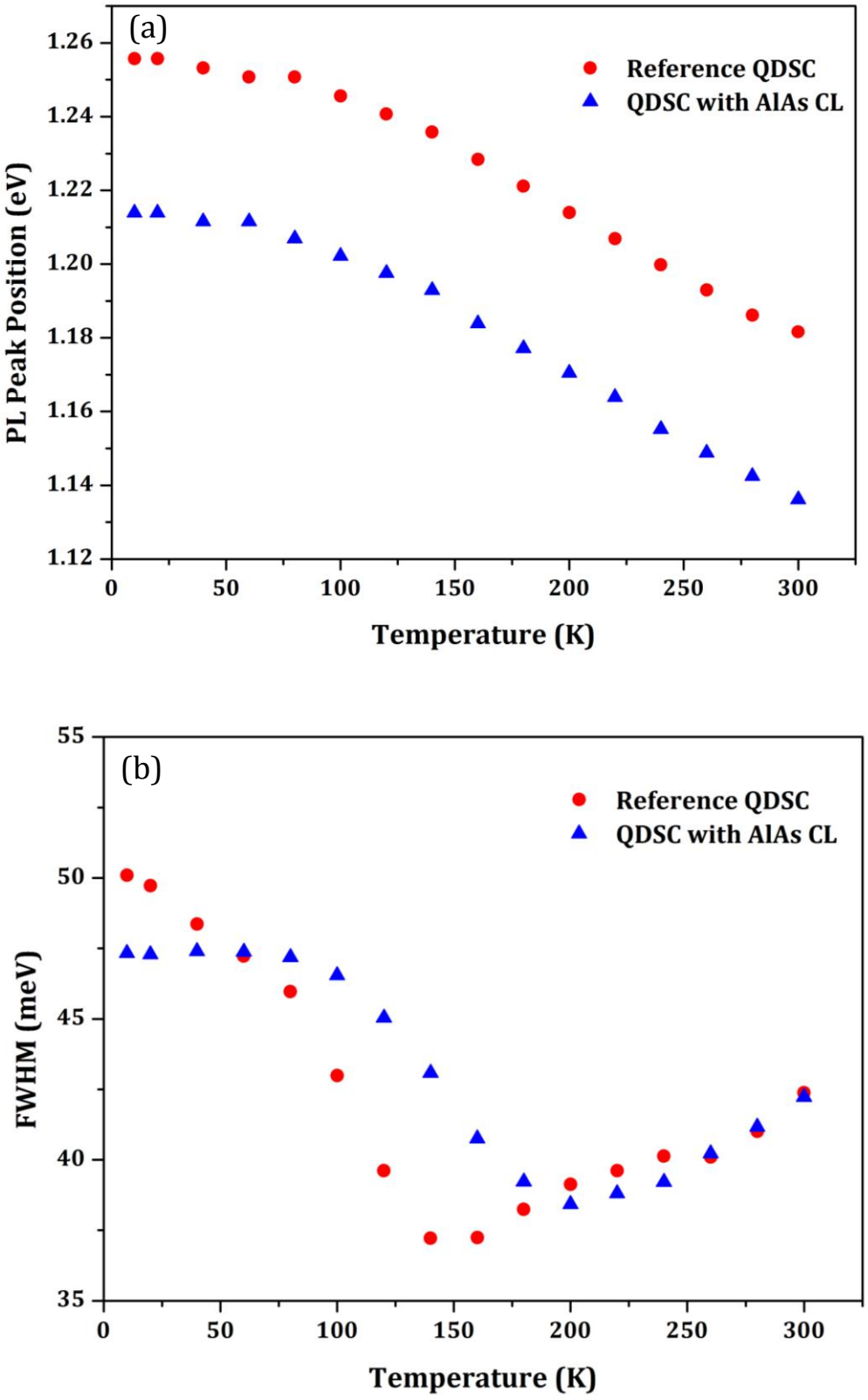

Figure 5.7 PL emission peak positions (a) and FWHM (b) as a function of temperature for the reference QDSC and the QDSC with AlAs CL.

Figure 5.7 shows the effects of temperature on the PL emission energy and the FWHM. From Figure 5.7 (a) it can be seen that the emission energy of QD ground states decrease with increasing temperature, following the empirical Varshni relationship [10] for both QDSCs. As the temperature increases, both QDSCs show an initial trend of a reduction in FWHM. With increasing temperature, thermalised carriers from smaller QDs with shallow energy levels repopulate larger QDs with deeper levels, resulting in a reduction in FWHM. As temperature is increased further, electron-phonon scattering becomes dominant and the FWHM begins to increase [11]. From Figure 5.7 (b) it can be seen that the FWHM for the reference QDSC drops faster and reaches it reaches its minimum (140K) earlier than the QDSC with AlAs CL. While the FWHM for the reference QDSC begins to fall at 20K, the FWHM of the QDSC with AlAs CL remains constants from 10K until 100K where it begins to drop, reaching its minimum at 160K. These results confirm once again that capping the InAs QDs with AlAs CL has led to an enhancement in carrier confinement.

The power dependent PL for the QDSCs is shown in Figure 5.8. The effect of increasing excitation power (1 – 70 mW) on the PL emission energy and the FWHM is shown in Figure 5.9. At higher optical excitation powers, both QDSC structures show little change in ground state emission energies (shown in Figure 5.9 (b)). For even higher excitation powers beyond 70 mW, excited states will be obvious. Figure 5.9 (b) shows a slight increase in FWHM for both QDSCs. This can be attributed to the filling of lower QD states, causing photoexcited carriers to occupy upper QD states.

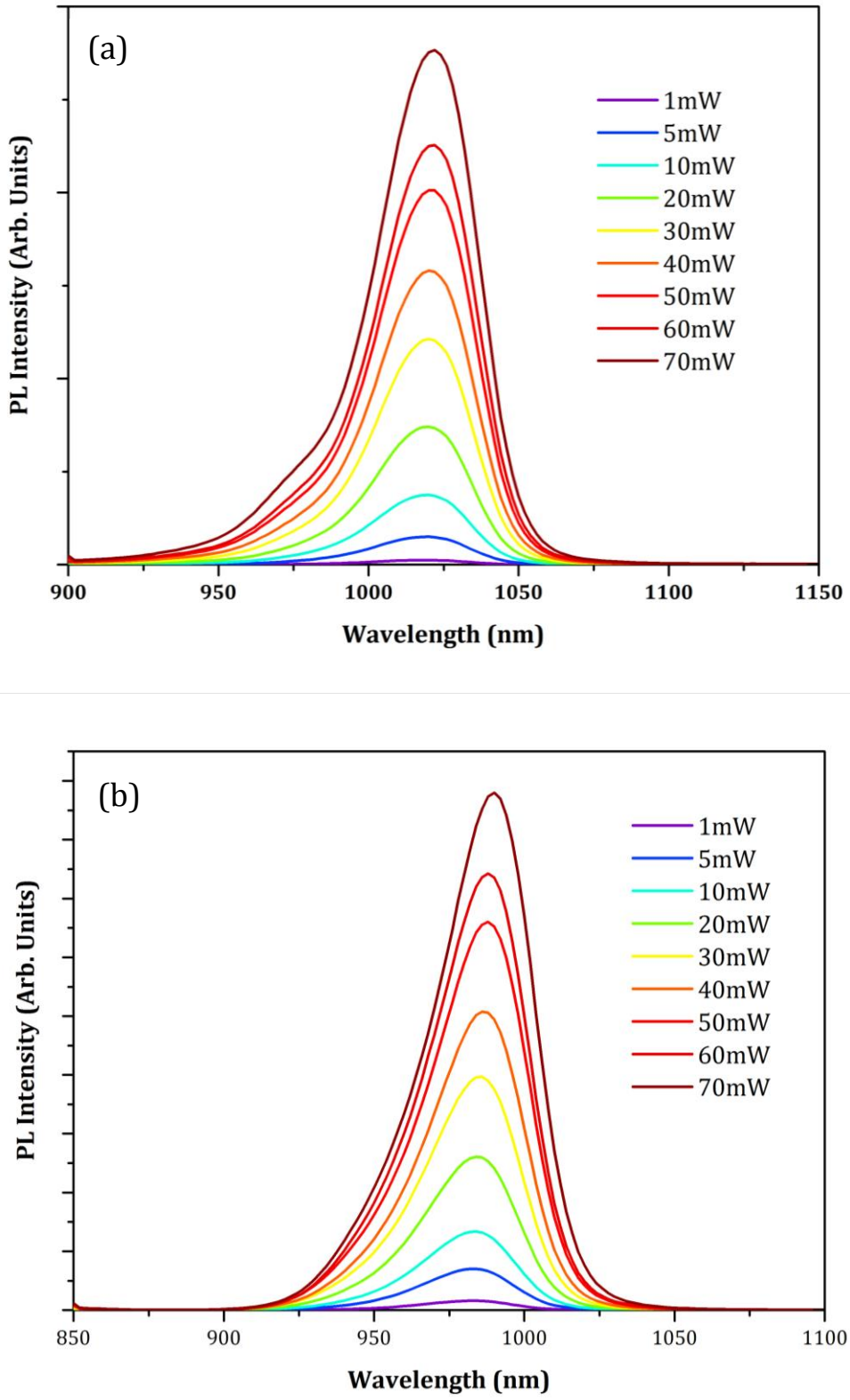

Figure 5.8 Excitation power dependent PL for the reference QDSCs (a) and the QDSC with AlAs CL (b)

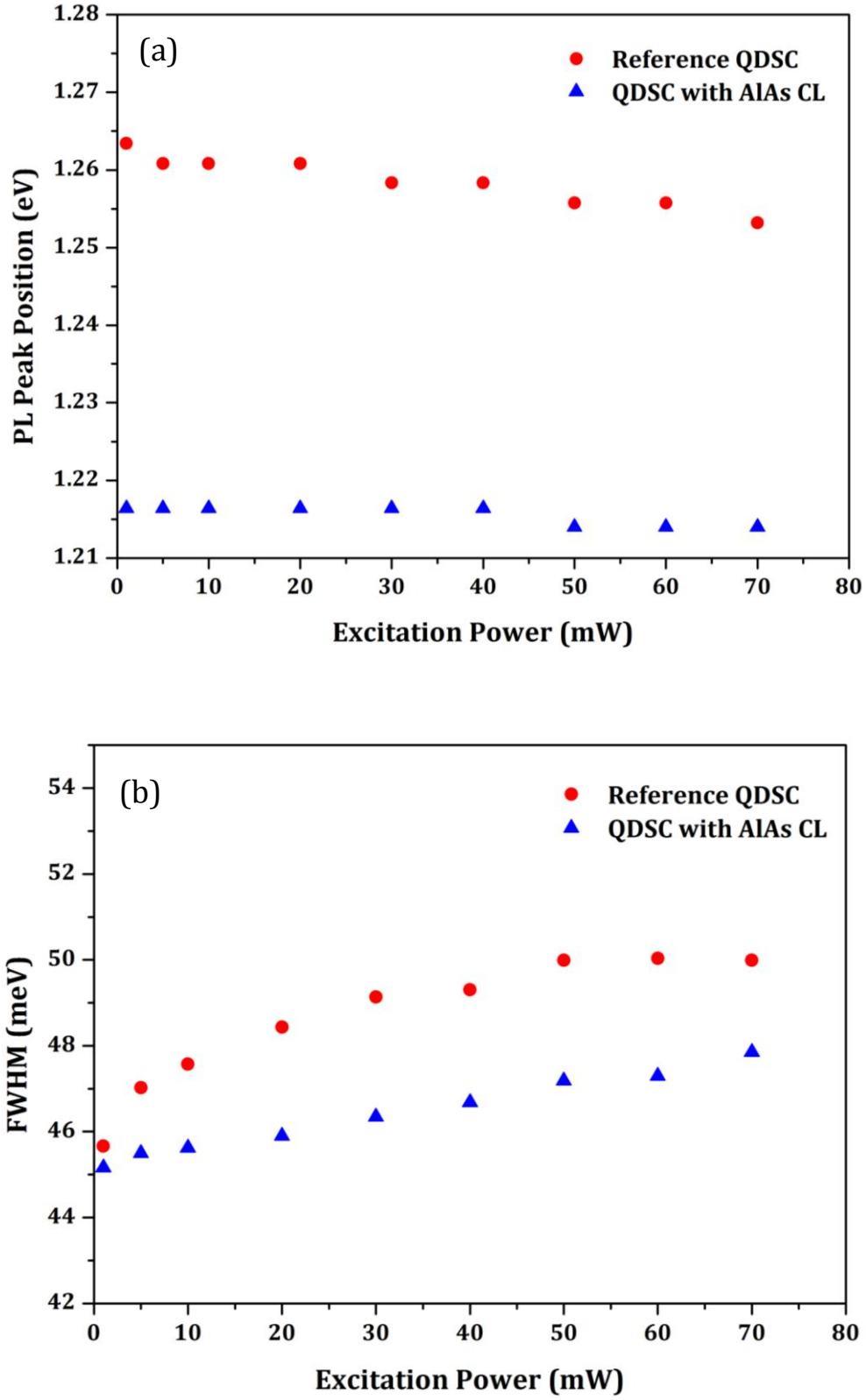

Figure 5.9 PL emission peak positions (a) and FWHM (b) as a function of excitation power.

5.2.3 Solar Cell Performances

Over the device fabrication process more than twenty SC devices were fabricated from each of the three wafers. The final eight had reproducible results and the best performing of these devices are presented here. Figure 5.10 shows the EQE of the solar cells as a function of wavelength. For the GaAs reference cell there is a drop in spectral response at a wavelength of ~ 870 nm, corresponding to the bandgap of GaAs. Above the GaAs bandgap, the EQE of the reference QDSC is slightly reduced compared to the GaAs reference cell. This can be attributed to local defects around the InAs QD/GaAs cap interface. It is clearly evident from the EQE measurements that for both QDSCs, the QDs contribute to the absorption of sub-bandgap photons beyond 1100 nm.

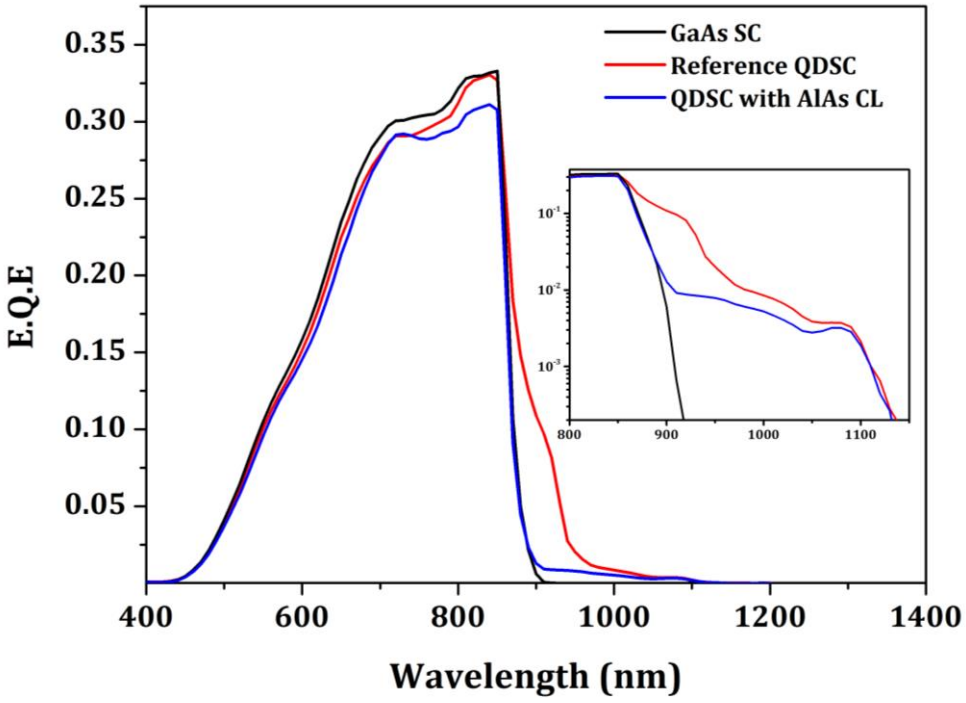

Figure 5.10 External quantum efficiency of InAs QDSCs with and without the AlAs CL, and the GaAs reference solar cell. The inset shows the EQE on a logarithmic scale for the wavelength range of 800 – 1200 nm.

The QDSC with AlAs CL has a substantial reduction in EQE above the GaAs bandgap. The reason for this is not clear but it is most likely due to defects at the AlAs-GaAs interface within the QD region because the growth temperature of AlAs CL is much lower than its optimized growth temperature around 700 ^{o}C. Since AlAs is a higher bandgap material than GaAs, it is also possible the AlAs layers around the QDs are impeding carrier transport.

The reference QDSC shows a near band-edge peak which can be attributed to the WL between QDs [12]. This photon absorption by the WL can be seen for the reference QDSC at ~915 nm. On the other hand, the EQE of the QDSC with AlAs CL (as shown by the inset of Figure 5.10), has a sharp drop within this region in a manner that is close to the GaAs reference sample. This indicates there is no WL absorption in QDSC with AlAs CL, and hence confirm what was observed in Figure 5.3 (f); i.e., the elimination of the WL of InAs/GaAs QDs by an AlAs CL.

The current density – voltage curve for the SCs measured under 1-sun AM1.5 illumination is shown in Figure 5.11. With a J_{sc} of 6.9 mA/cm^2 and a V_{oc} of 0.9 V, the power generated by the GaAs reference SC is greater than both QDSCs. In comparison, the J_{sc} and V_{oc} for the QDSCs are 7.4 mA/cm^2 and 0.69 V for the reference QDSC and 6.5 mA/cm^2 and 0.79 V for the QDSC with AlAs CL. The increase in J_{sc} for the reference QDSC is due to the presence of the QD structures within the *i*-region absorbing sub-bandgap photons, as shown in by the EQE measurements in Figure 5.10.

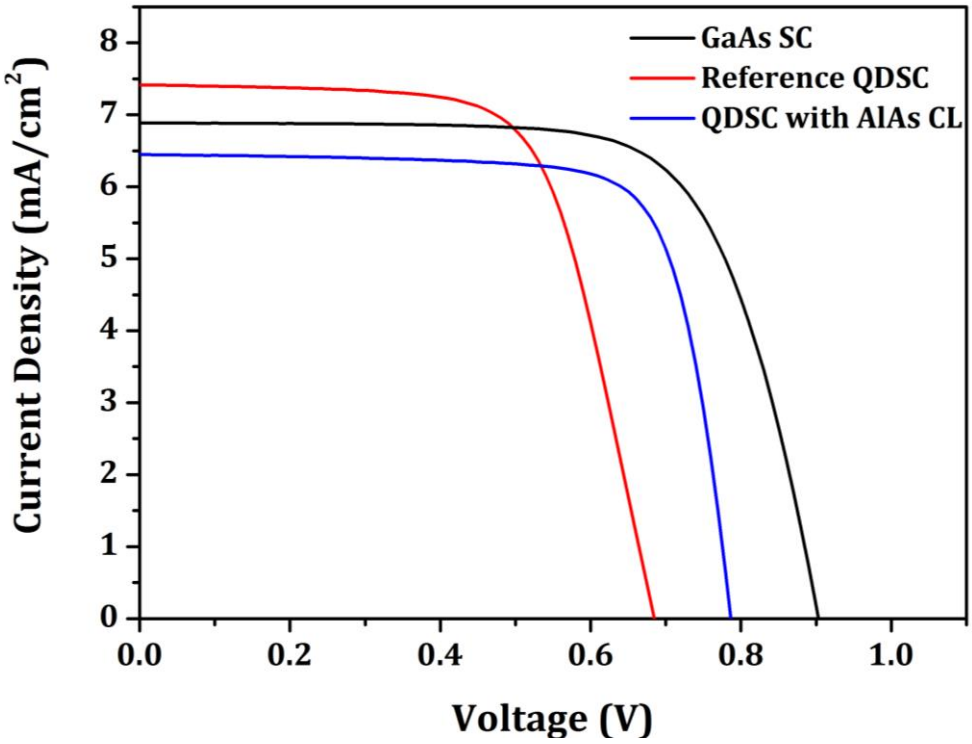

Figure 5.11 Current density vs. voltage curves for the InAs/GaAs QDSCs with and without AlAs CL, and the GaAs reference solar cell under 1-sun AM1.5 illumination.

For reasons mentioned earlier, the QDSC with AlAs CL has a reduced J_{sc} compared to both the GaAs reference SC and the reference QDSC. The drop in V_{oc} in the reference QDSC is due to the reduction in the CB-VB transition energy of the cell due to the WL and the closely packed confined energy levels of holes inside the QDs. In the case of the QDSC with AlAs CL, the absence of the WL leads to an enhancement of the V_{oc}. The dark current density-voltage curve for the QDSC with AlAs CL is reduced compared to the reference QDSC as shown in Figure 5.12. This can be attributed to the stronger carrier confinement achieved by the AlAs CL, and this also contributes to the increase in V_{oc}.

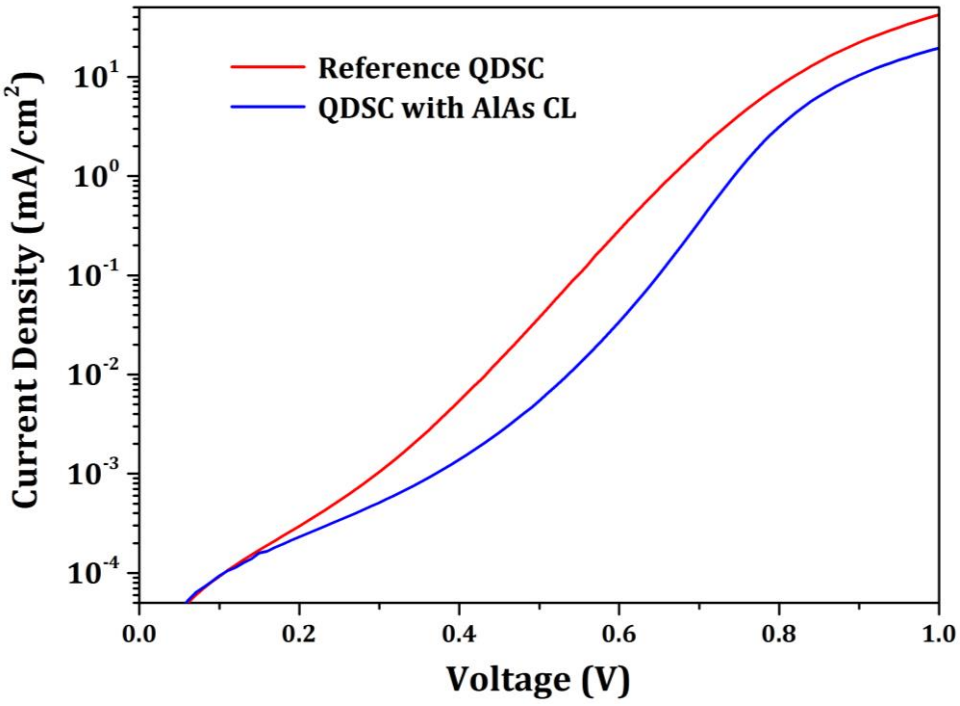

Figure 5.12 Dark current-density of the QDSCs.

In terms of efficiency, the enhancement of the V_{oc} in the QDSC with AlAs, more than compensates for the loss in J_{sc} to ensure that the efficiency of the QDSC with AlAs (3.86 %) is greater than that of the reference QDSC without an AlAs CL (3.40 %). It should be mentioned at this point that during the device processing the GaAs contact layer was left un-etched in order to simplify the fabrication. This explains the relatively low efficiency values for all the cells. Table 5.1 presents a summary of the solar cell parameters.

Solar Cells	*Jsc* (mA/cm²)	*Voc* (V)	*FF* (%)	*η* (%)
GaAs Reference Cell	6.89	0.90	70	4.35
Reference QDSC	7.41	0.69	67	3.40
QDSC with AlAs CL	6.45	0.79	76	3.86

Table 5.1 Short-circuit current (*Jsc*), open current voltage (*Voc*), fill factor (*FF*), and efficiency (*η*) for the QDSCs and the GaAs SC under 1 sun AM1.5 illumination.

As already mentioned, one of the main conditions for the optimal realisation of QD IBSCs is the requirement that the QD electronic sub-band levels that represent the intermediate band be optically coupled to, but electrically isolated from the CB. It has been shown that the increase in sub-bandgap photocurrent in InAs/GaAs QDSCs is due to the thermal escape of carriers from the QDs sub-bandgap energy levels into the CB and this is incompatible with the preservation of V_{oc} [13]. Due to the reduction in the CB-VB transition level in the QDSCs, the electronic populations in the intermediate band (IB) and the CB are not sufficiently separated [14]. The excited QD confined states and localised energy levels from defects encourage thermal escape and can also assist tunneling escape [15]. As a result, the IB-CB transition occurs by carrier escape mechanisms instead of the optical transition expected for the realisation of high efficiencies predicted by the IBSC model [16], [17]. This is the case for the reference QDSC, which shows a drop in V_{oc} of 0.21 V as compared to the GaAs reference cell. The preservation of the V_{oc} requires that the electronic population of the VB, IB and CB are associated with their own quasi-Fermi level [18]. The QDSC with AlAs CL has a V_{oc} of 0.79 V; a reduction of 0.11 V compared to the GaAs reference cell. Since the V_{oc} of a cell is equal to the difference between quasi-Fermi levels of the VB and CB (divided by the electron charge), the enhancement in effective bandgap resulting from the absence of the WL, corresponds accordingly to an enhancement of the V_{oc}. The increase in the effective bandgap for the QDSC with AlAs coupled with the redshift of the QD PL peak indicates that there is a wider electron population separation between the QD electron states and the edge of the CB continuum. To further illustrate this, Figure 5.13 presents simplified band diagrams of the QDSCs.

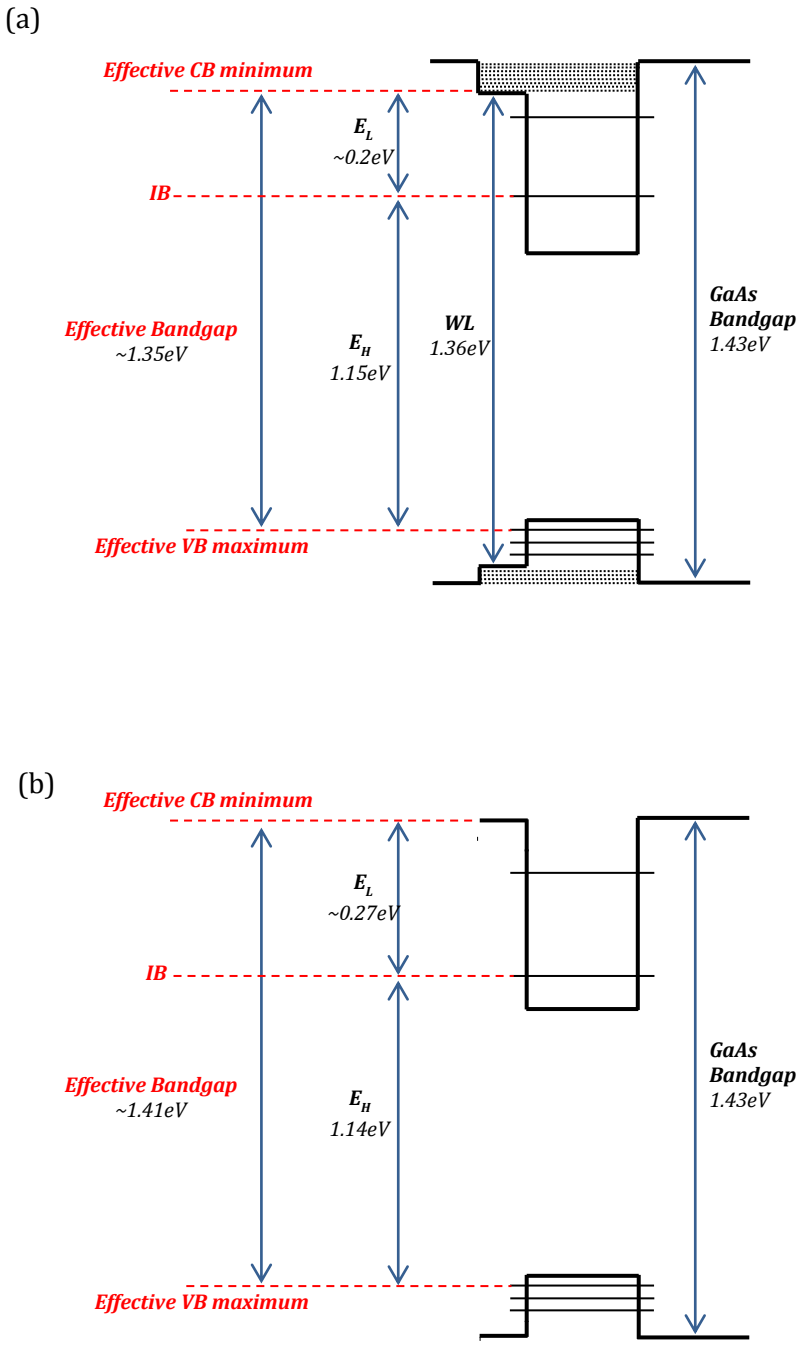

Figure 5.13 Simplified bandgap diagram of the QDSC with WL (a) and the QDSC without WL (b). The WL value is taken from the EQE plot. E_H is the ground state PL peak energy at room temperature and E_L is taken to be the value of the thermal activation energy.

5.3 Conclusion

In summary, we have presented the fabrication of an InAs/GaAs QDSC with an enhanced V_{oc} by the deposition of an AlAs CL on the InAs QDs to eliminate the WL. The enhancement in voltage was accompanied by an increase in thermal activation energy, both of which are due to increase in the effective bandgap of the QDSC. This result holds some promise for the splitting of QD sub-bandgap electron energy levels from the CB, which could be important in the implementation of IBSCs. Having eliminated the WL, it can be seen that, if a significant increase in QD density is achieved, then this will result in QDSCs with high values for J_{sc} in addition to the enhanced V_{oc}.

Bibliography

[1] A. Luque and A. Marti, "The intermediate band solar cell: progress toward the realization of an attractive concept.," *Advanced Materials*, vol. 22, no. 2, pp. 160–174, Jan. 2010.

[2] F. K. Tutu, I. R. Sellers, M. G. Peinado, C. E. Pastore, S. M. Willis, a. R. Watt, T. Wang, and H. Y. Liu, "Improved performance of multilayer InAs/GaAs quantum-dot solar cells using a high-growth-temperature GaAs spacer layer," *Journal of Applied Physics*, vol. 111, no. 4, p. 046101, 2012.

[3] R. Songmuang, S. Kiravittaya, and O. G. Schmidt, "Shape evolution of InAs quantum dots during overgrowth," *Journal of Crystal Growth*, vol. 249, no. 3–4, pp. 416–421, Mar. 2003.

[4] Q. Xie, P. Chen, and A. Madhukar, "InAs island-induced-strain driven adatom migration during GaAs overlayer growth," *Applied Physics Letters*, vol. 65, no. 16, p. 2051, 1994.

[5] A. F. Tsatsul'nikov, A. R. Kovsh, A. E. Zhukov, Y. M. Shernyakov, Y. G. Musikhin, V. M. Ustinov, N. A. Bert, P. S. Kop'ev, Z. I. Alferov, A. M. Mintairov, J. L. Merz, N. N. Ledentsov, and D. Bimberg, "Volmer–Weber and Stranski–Krastanov InAs-(Al,Ga)As quantum dots emitting at 1.3 μm," *Journal of Applied Physics*, vol. 88, no. 11, p. 6272, 2000.

[6] F. Ferdos, S. Wang, Y. Wei, M. Sadeghi, Q. Zhao, and A. Larsson, "Influence of initial GaAs and AlAs cap layers on InAs quantum dots grown by molecular beam epitaxy," *Journal of Crystal Growth*, vol. 251, no. 1–4, pp. 145–149, Apr. 2003.

[7] F. Adler, M. Geiger, a. Bauknecht, D. Haase, P. Ernst, a. Dörnen, F. Scholz, and H. Schweizer, "Self-assembled InAs/GaAs quantum dots under resonant excitation," *Journal of Applied Physics*, vol. 83, no. 3, p. 1631, 1998.

[8] Y. I. Mazur, Z. M. Wang, G. G. Tarasov, M. Xiao, G. J. Salamo, J. W. Tomm, V. Talalaev, and H. Kissel, "Interdot carrier transfer in asymmetric bilayer InAs/GaAs quantum dot structures," *Applied Physics Letters*, vol. 86, no. 6, p. 063102, 2005.

[9] R. Chen, H. Y. Liu, and H. D. Sun, "Electronic energy levels and carrier dynamics in InAs/InGaAs dots-in-a-well structure investigated by optical spectroscopy," *Journal of Applied Physics*, vol. 107, no. 1, p. 013513, 2010.

[10] E. Grilli, M. Guzzi, R. Zamboni, and L. Pavesi, "High-precision determination of the temperature dependence of the fundamental

energy gap in gallium arsenide.," *Physical review. B, Condensed matter*, vol. 45, no. 4, pp. 1638–1644, Jan. 1992.

[11] H. S. Lee, J. Y. Lee, T. W. Kim, D. U. Lee, D. C. Choo, M. Jung, and M. D. Kim, "Microstructural and optical properties of InAs/GaAs quantum dots embedded in modulation-doped Al[sub x]Ga[sub 1−x]As/GaAs heterostructures," *Journal of Applied Physics*, vol. 91, no. 8, p. 5195, 2002.

[12] D. Guimard, R. Morihara, D. Bordel, K. Tanabe, Y. Wakayama, M. Nishioka, and Y. Arakawa, "Fabrication of InAs/GaAs quantum dot solar cells with enhanced photocurrent and without degradation of open circuit voltage," *Applied Physics Letters*, vol. 96, no. 20, p. 203507, 2010.

[13] E. Antolin, A. Marti, C. R. Stanley, C. D. Farmer, E. Cánovas, N. Lopez, P. G. Linares, and A. Luque, "Low temperature characterization of the photocurrent produced by two-photon transitions in a quantum dot intermediate band solar cell," *Thin Solid Films*, vol. 516, no. 20, pp. 6919 – 6923, 2008.

[14] A. Marti, C. R. Stanley, and A. Luque, *Nanostructured Materials for Solar Enegy Conversion*. Amsterdam: Elsevier Science, 2006, pp. 539–566.

[15] E. Antolin, A. Marti, C. D. Farmer, P. G. Linares, E. Hernández, A. M. Sánchez, T. Ben, S. I. Molina, C. R. Stanley, and A. Luque, "Reducing carrier escape in the InAs/GaAs quantum dot intermediate band solar cell," *Journal of Applied Physics*, vol. 108, no. 6, p. 064513, 2010.

[16] A. Luque and A. Marti, "Increasing the Efficiency of Ideal Solar Cells by Photon Induced Transitions at Intermediate Levels," *Physical Review Letters*, vol. 78, no. 26, pp. 5014–5017, Jun. 1997.

[17] A. Martí, E. Antolín, C. Stanley, C. Farmer, N. López, P. Díaz, E. Cánovas, P. Linares, and A. Luque, "Production of Photocurrent due to Intermediate-to-Conduction-Band Transitions: A Demonstration of a Key Operating Principle of the Intermediate-Band Solar Cell," *Physical Review Letters*, vol. 97, no. 247701, pp. 1–4, Dec. 2006.

[18] N. J. Ekins-Daukes, C. B. Honsberg, and M. Yamaguchi, "Signature of intermediate band materials from luminescence measurements," in *31st IEEE Photovoltaic Specialists Conference, 2005. Conference*, 2005, pp. 49–54.

Chapter 6

InAs/GaAs quantum dot solar cells with Sb – Mediated Growth

One of the major challenges in the implementation of QD-IBSCs is the weak absorption of QDs as a result of low QD density. Moreover, in an ideal IB material, the IB extends throughout the entire material, while in QDs, the mini-band formed is limited mainly to the QD region [1]. On the other hand, the strain-driven self-assembled QDs from lattice-mismatched materials limit the number of layers of QDs that can be incorporated in the solar cells without degradation of material quality. Although QD solar cells with 50 QD layers have been demonstrated, an increase in recombination in the QD region led to a decrease in efficiency [2]. Therefore, QDs have made only limited progress towards high efficiency solar cells. Even though the introduction of QDs has been shown to extend solar spectral coverage through sub-bandgap photon absorption, the contribution of QDs to the enhancement of photocurrent is still marginal. The current gain is not enough to compensate for the typical loss in voltage.

In order to realize the potential of QD IBSCs, the optical absorption of QD arrays must be substantially improved. To this end, strain-balanced layers,

plasmonic materials, and strain-free nanostructures have been investigated to boost the photon absorption and hence the short-circuit current density (J_{sc}) in QD-IBSCs [3]–[6]. Another alternative for increasing photon absorption would be to grow high in-plane density of QDs [7], [8]. Zhou *et al.* aimed to increasing the solar cell efficiency using high density of QDs (five layers with sheet density of 7.0×10^{10} cm^{-2}) by a low temperature growth and a small V/III flux ratio [8]. However, due to the formation of nonradiative recombination centers and low overall absorption volume in the QD region ($\sim 3.5 \times 10^{11}$ cm^{-2}), no improvement in the J_{sc} was demonstrated.

In this chapter, the antimony (Sb)-mediated growth of high-density InAs QDs for enhanced GaAs sub-bandgap photon absorption in QD-IBSCs is presented. In-plane quantum dot density over 1×10^{11} cm^{-2} was achieved by depositing Sb before InAs QD growth. The growth temperature and InAs coverage were investigated to obtain high QD density as well as low density of defective coalesced dots. Distinct improvement in J_{sc} has been demonstrated by using a high QD density of $\sim 2.0 \times 10^{12}$ cm^{-2} (20 QD layers with sheet density of about 1.0×10^{11} cm^{-2}). Some results from ongoing work on QDSCs with both AlAs CL and Sb-mediated growth are presented at the end of the chapter. Preliminary work on InAs/InGaP QDSCs is also briefly discussed.

6.1 Experimental Work

6.1.1 Growth Details

The samples were grown by molecular beam epitaxy (MBE) on *n+* GaAs (100) substrates. To obtain high density QDs, a series of samples consists of a buried QD layer sandwiched by GaAs barriers and an uncapped surface QD layer were grown with different amount of Sb irradiation and InAs coverage. The QD growth temperatures were between 470 and 500 ^{o}C. Three solar cell samples; a GaAs reference cell, a QD reference cell without Sb-mediated growth and a QD cell with Sb-mediated growth, were grown. The reference GaAs solar cell and QD reference cell structure were grown using the same

conditions described in Chapter 6. In order to suppress the formation of threading dislocations, high-growth-temperature GaAs spacer layers were used [9], [10]. Apart from the QD growth conditions, the Sb-mediated high-density QD cell has the same device structure as the QD reference cell. The morphological properties of the QD samples grown at different conditions were characterized by a Veeco Nanoscope V atomic force microscope (AFM). Figure 6.1 shows the schematic of the QDSC with Sb-mediated growth.

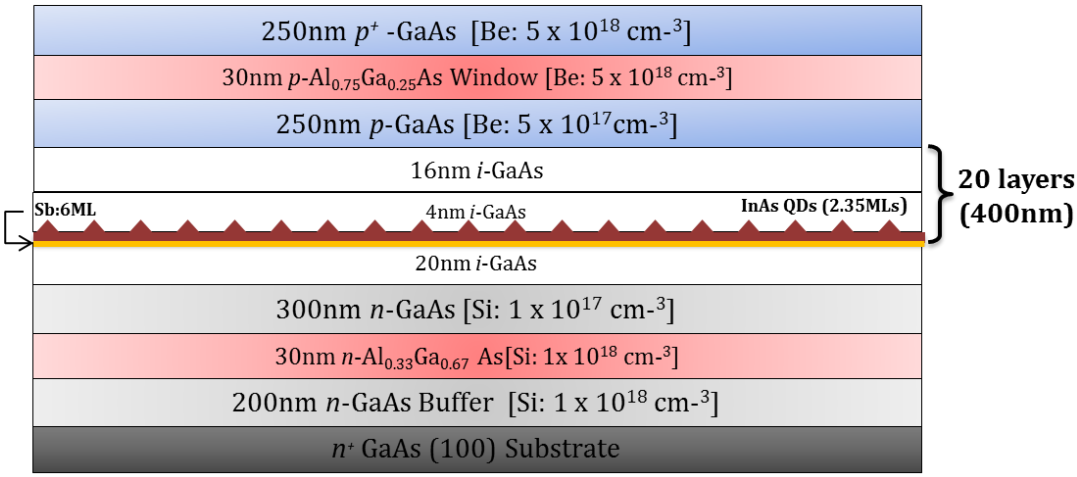

Figure 6.1 Schematic of the QDSC with Sb-mediated growth.

6.1.2 Device Processing and Characterisation

The metal contacts, Au-Zn-Au and AuGe-Au, were deposited by evaporation for the *p* and *n* contacts, respectively. The current density–voltage (*J*-*V*) characteristics were measured under the illumination of a one sun AM 1.5 solar simulator at room temperature (RT). The external quantum efficiency (EQE) measurements were also obtained at room temperature and at zero bias. Photoluminescence (PL) measurements were carried out with excitation from a 532 nm diode-pumped solid-state laser at a power of 60 mW. Temperature dependent PL measurements were taken from 10 to 300 K for the QDSCs.

6.2 Results and Discussion

6.2.1 Structural Characterisation

Figure 6.2 shows the AFM images of three QD samples grown at 500 °C. Figure 6.2 (a), (c) and are AFM images (1 × 1 μm^2) of 2.1 ML InAs QDs grown with no Sb irradiation, 3 ML Sb and 6 ML Sb irradiation respectively. Without any supply of Sb, the QD density is about 2.3 × 10^{10} cm^{-2}. It is clearly shown that after Sb deposition, the QD density increases and the QD size and height decreases. With Sb supply amounts of 3 ML and 6 ML, the QD density increases to 2.9 × 10^{10} cm^{-2} and 4.4 × 10^{10} cm^{-2}, respectively. From the 5 × 5 μm^2 AFM images for the QD growths with no Sb, 3 ML Sb and 6 ML Sb (shown in Figure 6.2 (b), (d) and (e)) it can be seen that there are no defective cluster dots.

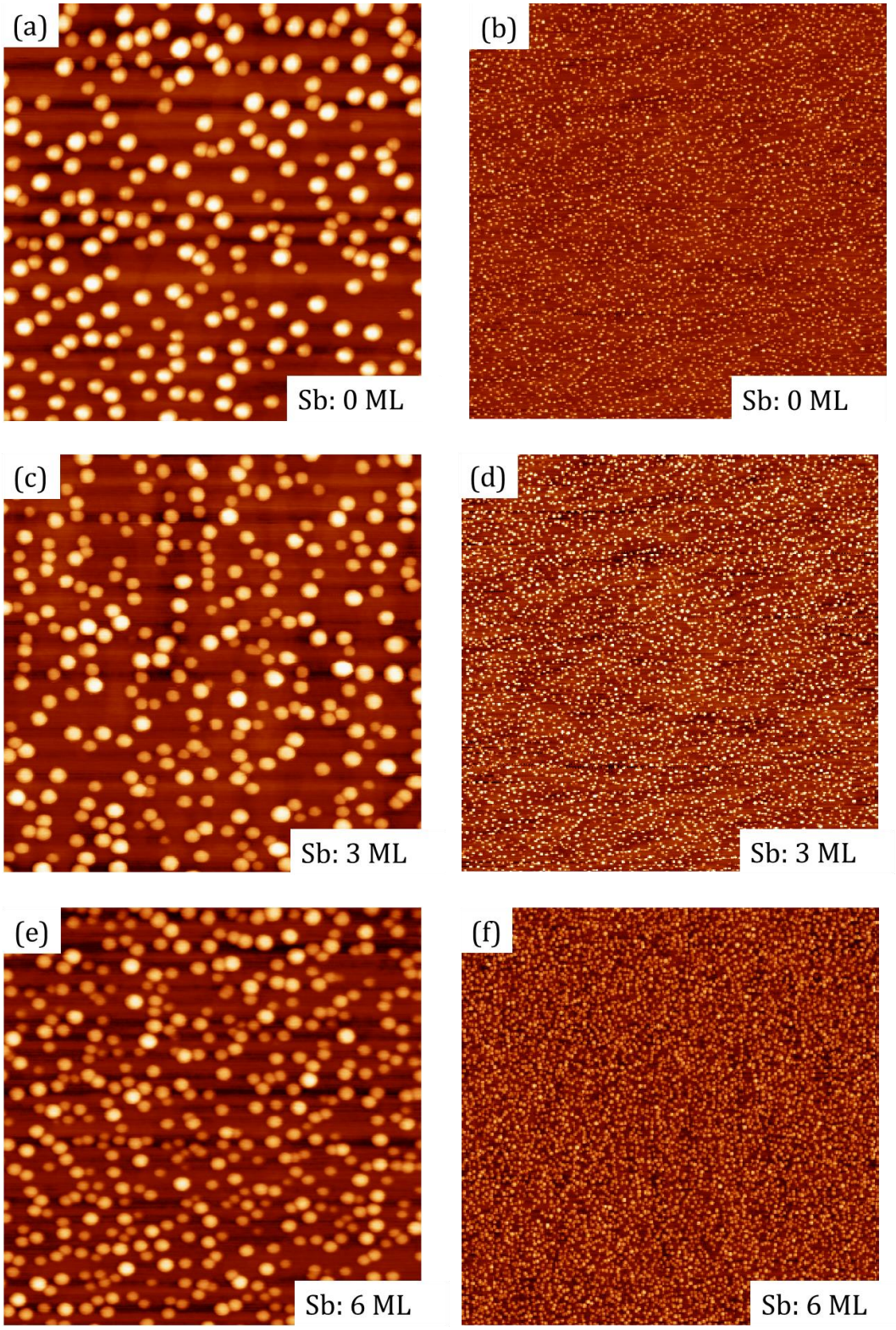

Figure 6.2 AFM images (1 × 1 μm²) of 2.1 ML InAs QDs grown at 500 °C with (a) no Sb, (c) 3 ML Sb and (e) 6 ML Sb irradiation. The corresponding 5 × 5 μm² images are shown in (b), (d) and (f).

The increase of QD density can be attributed to the Sb atoms segregated at the growth front [11]. Here, the Sb atoms work as an active surfactant, which bonds to the GaAs layer and forms small islands. In addition, the supply of Sb increases the step densities on the GaAs surfaces as evidenced by in-situ scanning tunneling microscopy analysis [12]. These islands and numerous surface steps formed on GaAs surface reduce the In adatom diffusion length and provide nucleation sites for InAs QD growth. Consequently, Sb-mediated QD growth has resulted in high QD density but with smaller QD sizes and heights.

In order to further improve the QD density, a higher InAs coverage, 2.8 ML, is deposited along with Sb supply amount of 6 ML. As shown in Figure 6.3 (a), at a growth temperature of 500 ^{o}C, the increase in InAs coverage to 2.8 ML has increased the QD density to 6.4 × 10^{10} cm^{-2}. The increase of QD density with InAs coverage has been observed to follow a power law dependence [13]. Figure 6.3 (c) and (e) are the AFM images (1 × 1 μm^2) of InAs QDs deposited at two lower temperatures, 470 ^{o}C and 485 ^{o}C, while keeping the same amounts of Sb (6 ML) and InAs (2.8ML). The decrease in growth temperature leads to formation of even smaller and denser QDs. The in-plane QD density increased to 8.9 × 10^{10} cm^{-2} at the growth temperature of 485 ^{o}C and 1.14 × 10^{11} cm^{-2} at 470 ^{o}C. The further reduction in In adatom diffusion length at lower growth temperatures is believed to contribute to this increase in QD density. However, this also leads to a significant increase in large clusters, as shown in Figure 6.3 (b), (d) and (f). The cluster density increases more than one order of magnitude from 1.8 × 10^{8} cm^{-2} to 3.3 × 10^{9} cm^{-2} with reducing the growth temperature from 500 ^{o}C to 470 ^{o}C. Figure 6.4 shows the QD density and cluster density as a function of growth temperature.

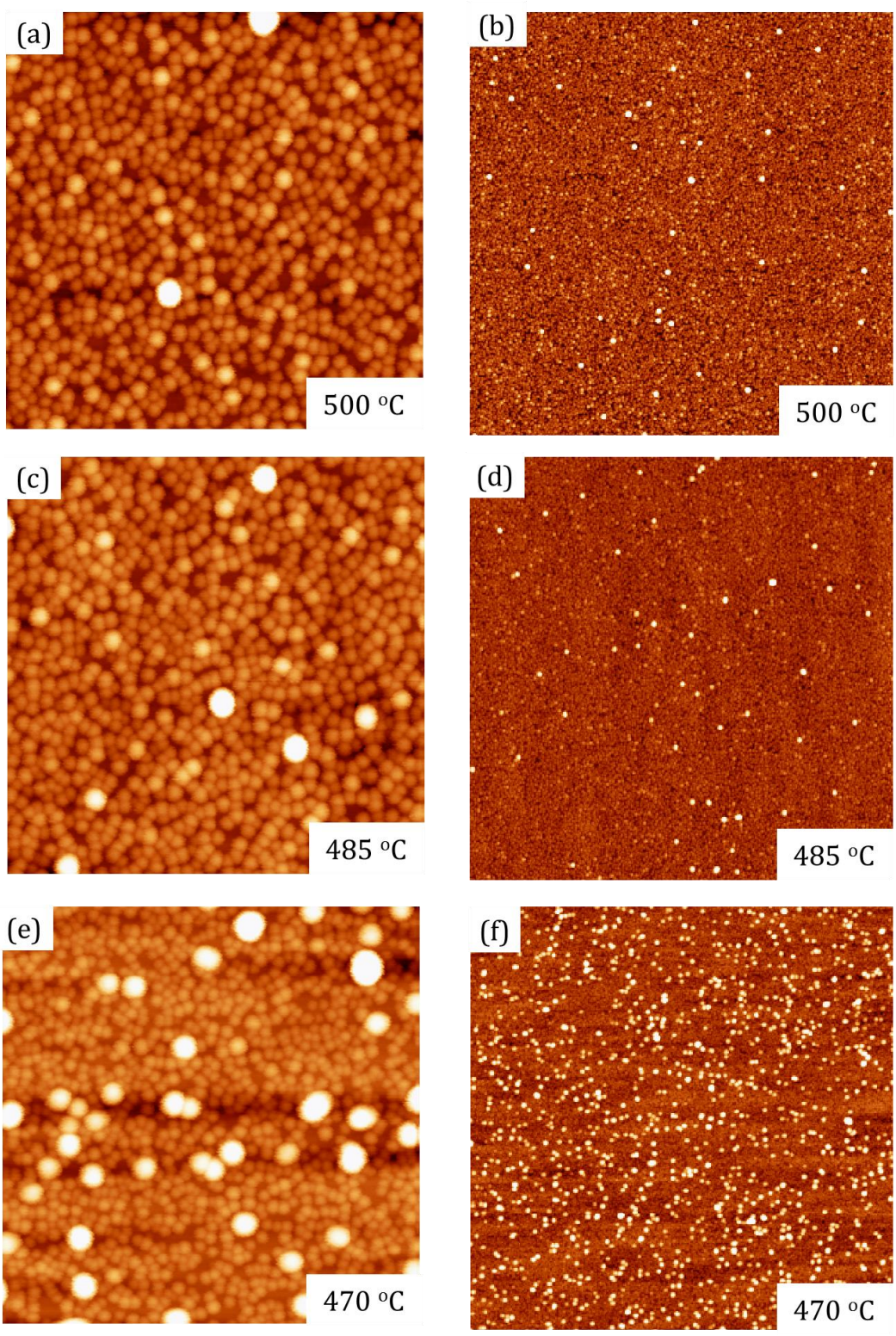

Figure 6.3 AFM images (1 ×1 μm²) of 2.8 ML InAs QDs grown at (a) 500 °C, (c) 485 °C and (e) 470 °C with 6 ML Sb irradiation. The corresponding 5 × 5 μm² images are shown in (b), (d) and (f).

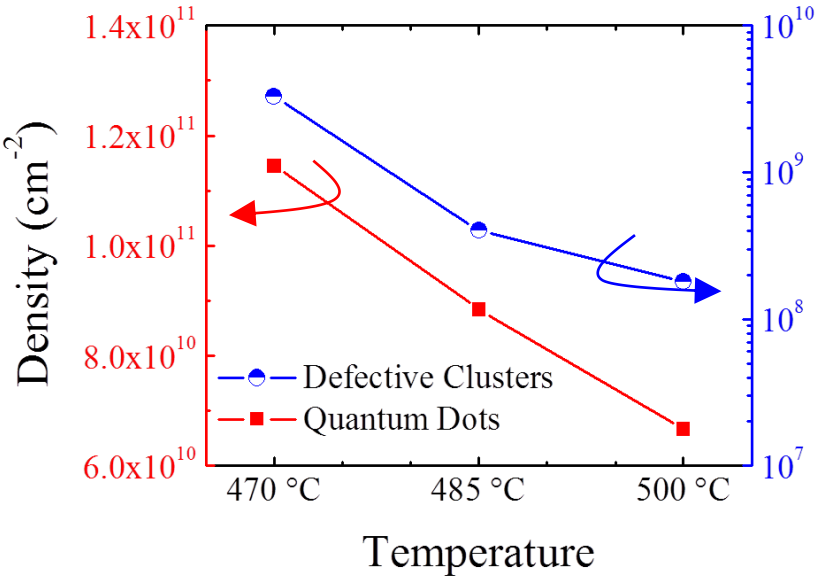

Figure 6.4 Coherent QD density (filled red square, left axis) and defective cluster density (half-filled blue circle, right axis) as a function of growth temperature.

The appearance of large clusters is due to the coalescence of small dots [14]. The coalescence results in large clusters and then misfit dislocations. The defective clusters are non-radiative recombination centres which decrease the lifetime of photo-excited carriers. The material degradation of QD grown at low temperatures is also confirmed by the reduced PL intensity, as shown in Figure 6.5. The PL spectra of the smaller QDs obtained at low growth temperatures show a slight redshift, which is in contradiction to the enhanced quantum confinement of small QDs. This abnormal PL spectra redshift of smaller QDs suggests that the lower growth temperature has led to the incorporation of the Sb atoms in the QD structure. At lower deposition temperatures, a higher amount of Sb is expected on the growth surface. The increase of the effective Sb amount on the substrate surface can affect the QD emission in two ways. Firstly, the Sb can be incorporated into the wetting layers and reduce the strain of the QDs, which can result in a red shift of the QD PL. Secondly, the presence of the Sb can suppress the interdiffusion of In-Ga during GaAs capping [15]. Consequently, at lower growth temperatures, the aspect ratio of the QDs can be better preserved because of a higher Sb amount.

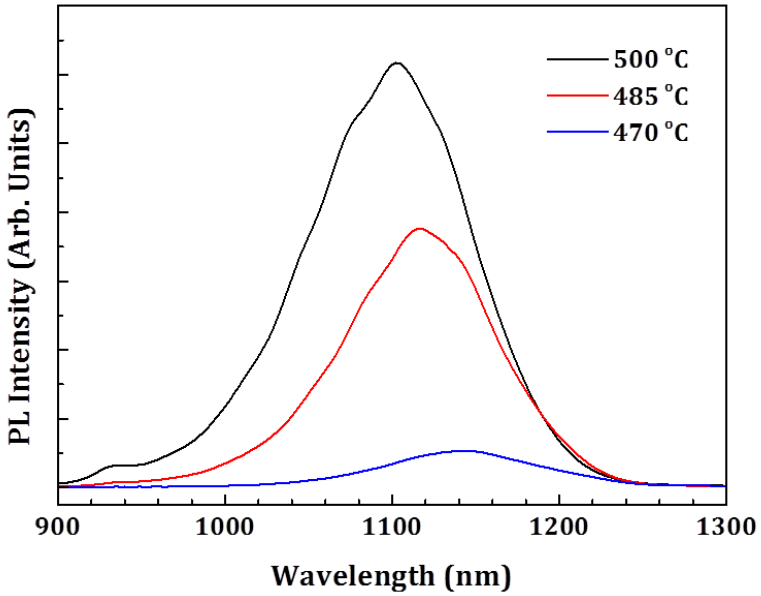

Figure 6.5 PL spectra of InAs QDs growth with 6 ML of Sb and at different temperatures.

In order to obtain high density of coherent-island while suppressing coalescence, InAs coverages ranging from 2.2 to 2.8 ML QD are used at the growth temperature of 485 ºC, at which moderately high QD densities and relatively low cluster densities can be grown. The Sb supply amount remains at 6 ML for all samples. Figure 6.6 (a) – (e) are AFM images of QDs grown using InAs coverages of 2.2 ML, 2.35 ML, 2.5 ML, 2.65 ML, and 2.8 ML. Figure 6.6 (f) shows the coherent QD density and big cluster density as a function of InAs coverage. At low InAs coverages of 2.2 ML and 2.35 ML, the surfaces are nearly cluster free and the coherent QD densities are 7.5×10^{10} cm^{-2} and 1.0×10^{11} cm^{-2}. Except for a slight drop in QD density for 2.8 ML InAs QDs, further increase in InAs coverage leads to further increase in QD density. The slight decrease in QD density at 2.8 ML is due to the formation of large clusters from the ripening process and coalescence of small dots. While the coherent QD density increases to the order of 1.0×10^{11} cm^{-2}, the defective clusters abruptly increase to 4.0×10^{8} cm^{-2}. The cluster density can be maintained relatively low about 1.0×10^{8} cm^{-2}, when the InAs coverage is kept below 2.5 ML. Interestingly, the PL spectra measured at room temperature (Figure 6.7(a)) show a redshift with increasing InAs coverage.

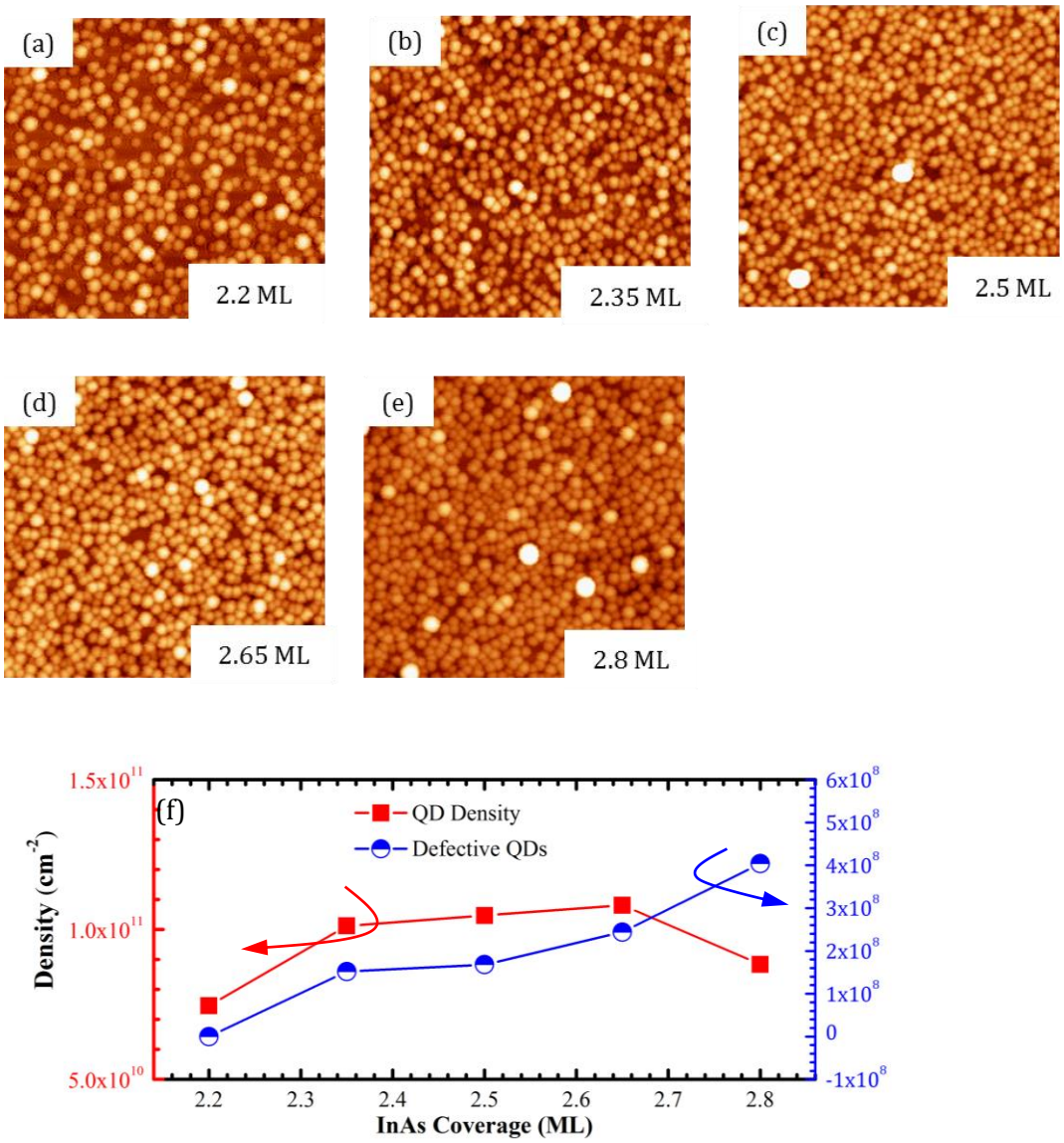

Figure 6.6 AFM images (1 ×1 μm²) of QDs grown at 485 ºC with 6 ML Sb irradiation and InAs coverage of (a) 2.2 ML, (b) 2.35 ML, (c) 2.5 ML, (d) 2.65 ML, (e) 2.8 ML. (f) Coherent QD density (filled red square, left axis) and defective cluster density (half-filled blue circle, right axis) as a function of InAs coverage.

Unlike the growth carried out at different temperatures, the effective Sb supply amount of all the samples in Figure 6.6(a)-(e) is the same. Therefore, effects of Sb irradiation on the surface energy and In adatom diffusion length do not play a critical role in the QD evolution of the samples with different InAs coverages. When increasing InAs coverage, the Sb limits the diffusion of In adatoms and thus, causes nucleation of additional QDs. However, the QDs formed at earlier stages may also have material gain from In adatoms around

the QD edge within the diffusion length as well as from direct deposition. Due to reduced surface diffusion length, the material gain from surface adatoms is negligible while increase in the QD volume may be mainly from direct deposition. Therefore, at a higher InAs coverage, the QDs are denser and slightly taller, which is clearly shown in the height histograms in Figure 6.7(b).

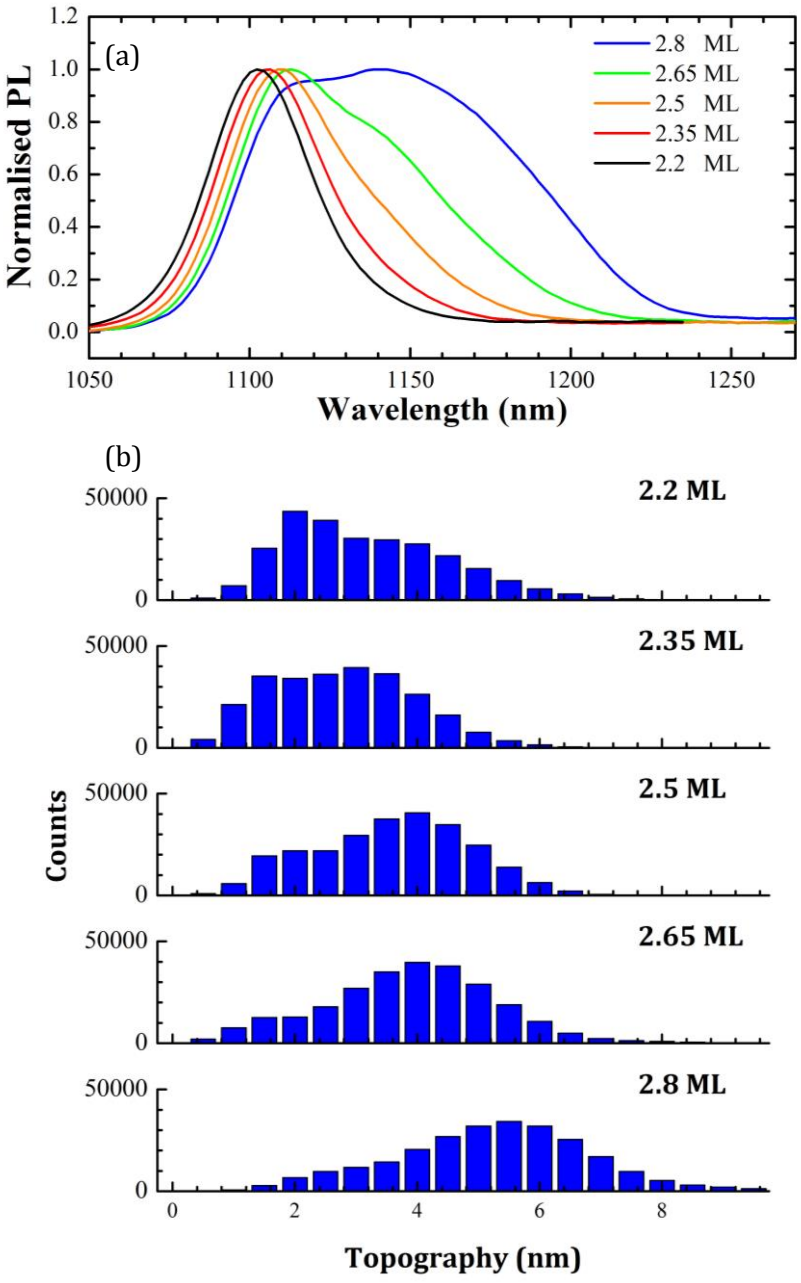

Figure 6.7 (a) Normalized room temperature PL spectra and (b) height histogram of QD samples in Figure 6.6 (a)-(e).

6.2.2 Optical Characterisation

To fabricate the QDSC, the QDs were grown using 6 ML Sb pre-deposition and InAs coverage of 2.35 ML at 485 ºC. At this growth condition, the Sb-mediated growth can achieve an in-plane QD density as high as 1.0×10^{11} cm^{-2} and maintain a lower defective cluster density of about 1.0×10^{8} cm^{-2}. The optical properties of the reference QDSC and the high-density QDSC with Sb-mediated growth were compared. Figure 6.8 shows the PL spectra for the QDSCs at RT. The PL peak intensity for the QDSC with Sb-mediated growth is about double that of the reference QDSC without Sb. The emission peaks for the reference QDSC and the QDSC with Sb-mediated growth are at 1078 nm and 1096 nm respectively. As already mentioned, the redshift of the PL emission of the QDSC with Sb-mediated growth is likely due to the incorporation of Sb into the QD structure.

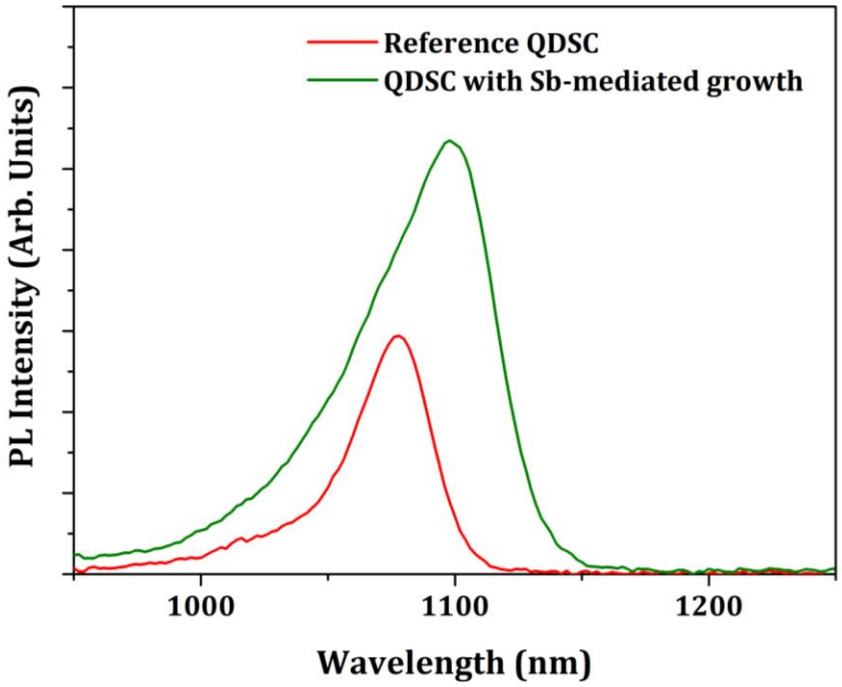

Figure 6.8 PL spectra of QDSCs at RT

The full width at half maximum (FWHM) for the reference QDSC and the high-density QDSC emission peaks are ~42 meV and 72 meV. This difference in FWHM suggests that the high-density QDSC with Sb has a broader

distribution of QD sizes. The bimodal nature of the high-density QDSC with Sb is seen in Figure 6.9 which shows the temperature-dependent PL (10 – 300K) and the excitation dependent PL of the QDSC.

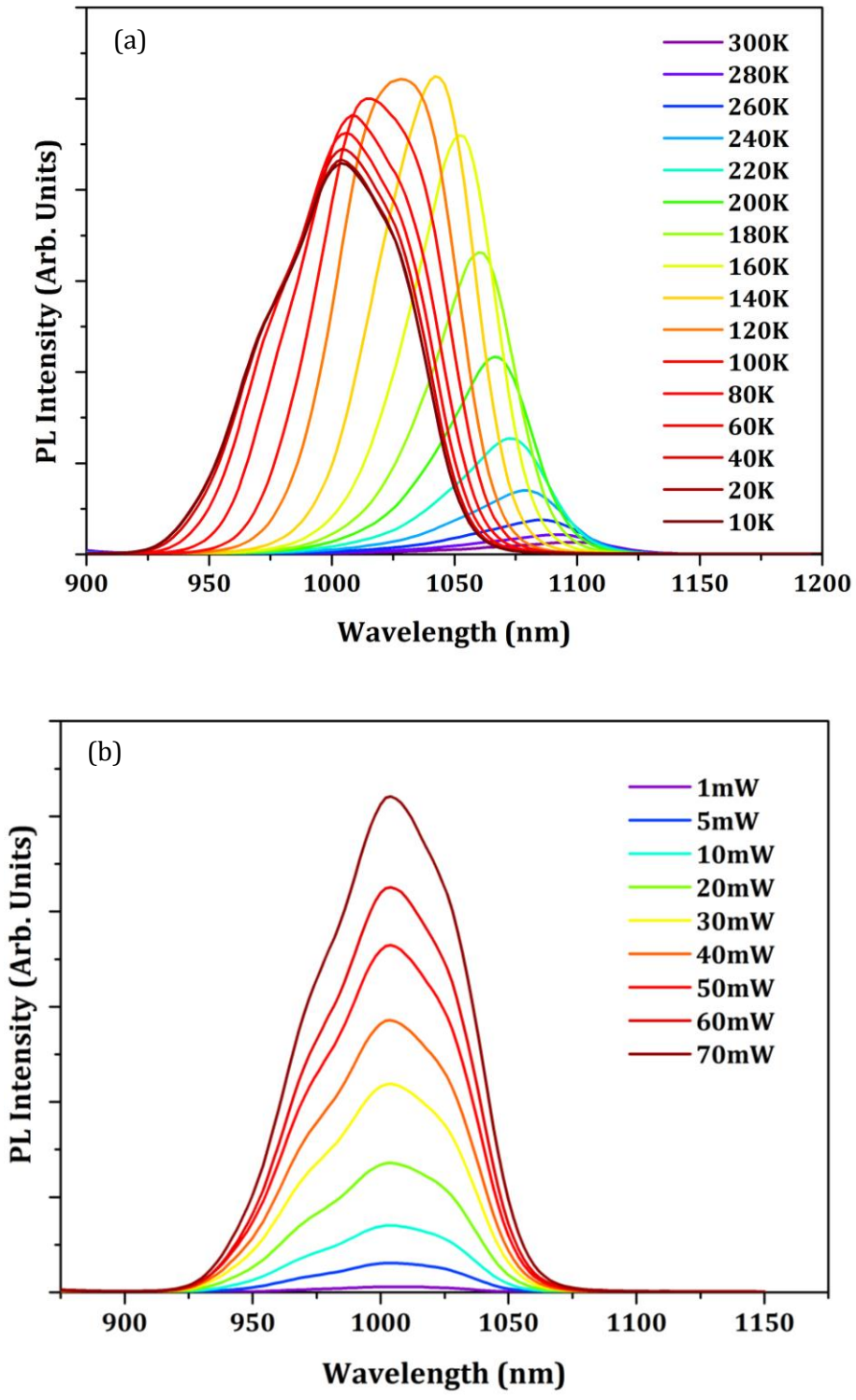

Figure 6.9 Temperature dependent PL (a) and excitation power dependent PL (b) for the QDSC with Sb-mediated growth.

The integrated PL intensity was also compared for the QDSCs, as shown in Figure 6.10. It is observed that at low temperatures, the PL intensities of the QDSCs are comparable. At higher temperatures, the PL intensity of the high-density QDSC with Sb is slightly stronger than the reference QDSC. This suggests that Sb-mediated growth has led to slightly less carrier escape at high temperatures attributed to the absence of InGaAs layers between QDs.

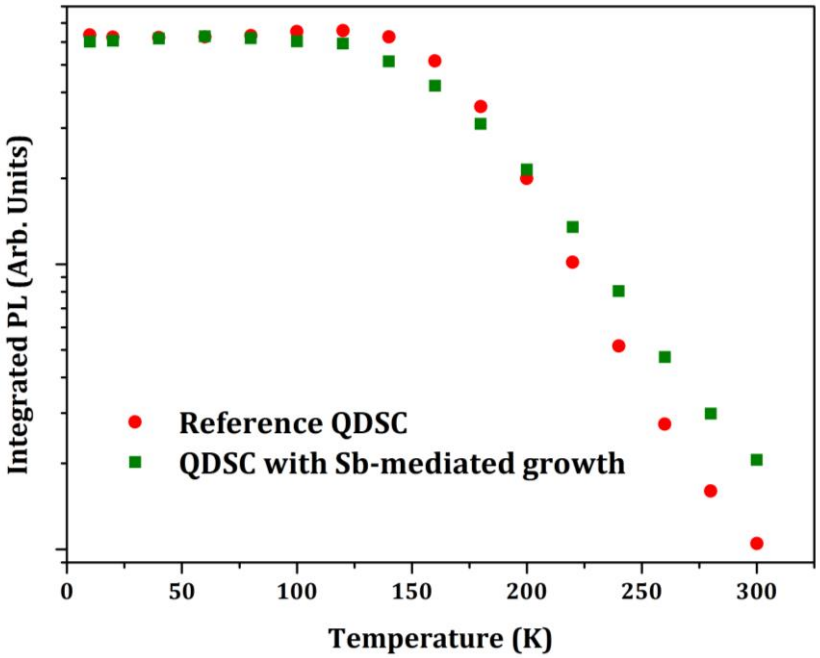

Figure 6.10 Comparison of the temperature dependence of the integrated PL intensity of the reference QDSC and the QDSC with Sb-mediated growth.

Figure 6.11 shows the effects temperature on the PL emission energy and the FWHM. Figure 6.11 (a) shows that the emission energy of QD ground states decrease with increasing temperature, following the empirical Varshni relationship [16] for both QDSCs. The FWHM for both QDSCs begin to decrease with increasing temperature, reaching a minimum value before rising. With increasing temperature, thermalised carriers from smaller QDs with shallow energy levels repopulate larger QDs with deeper levels, resulting in a reduction in FWHM. As temperature is increased further, electron-phonon scattering becomes dominant and the FWHM begins to increase [17]. The reference QDSC shows a reduction in FWHM of 28 % from

its highest value at 10K to its minimum value at 140 K, whereas the high-density QDSC with Sb shows a reduction of 48 % in FWHM from its highest to its lowest value at 180 K. The larger reduction in FWHM for the high-density QDSC with Sb can be attributed an enhancement in interdot transfer due to the increased lateral coupling in high density QD layers.

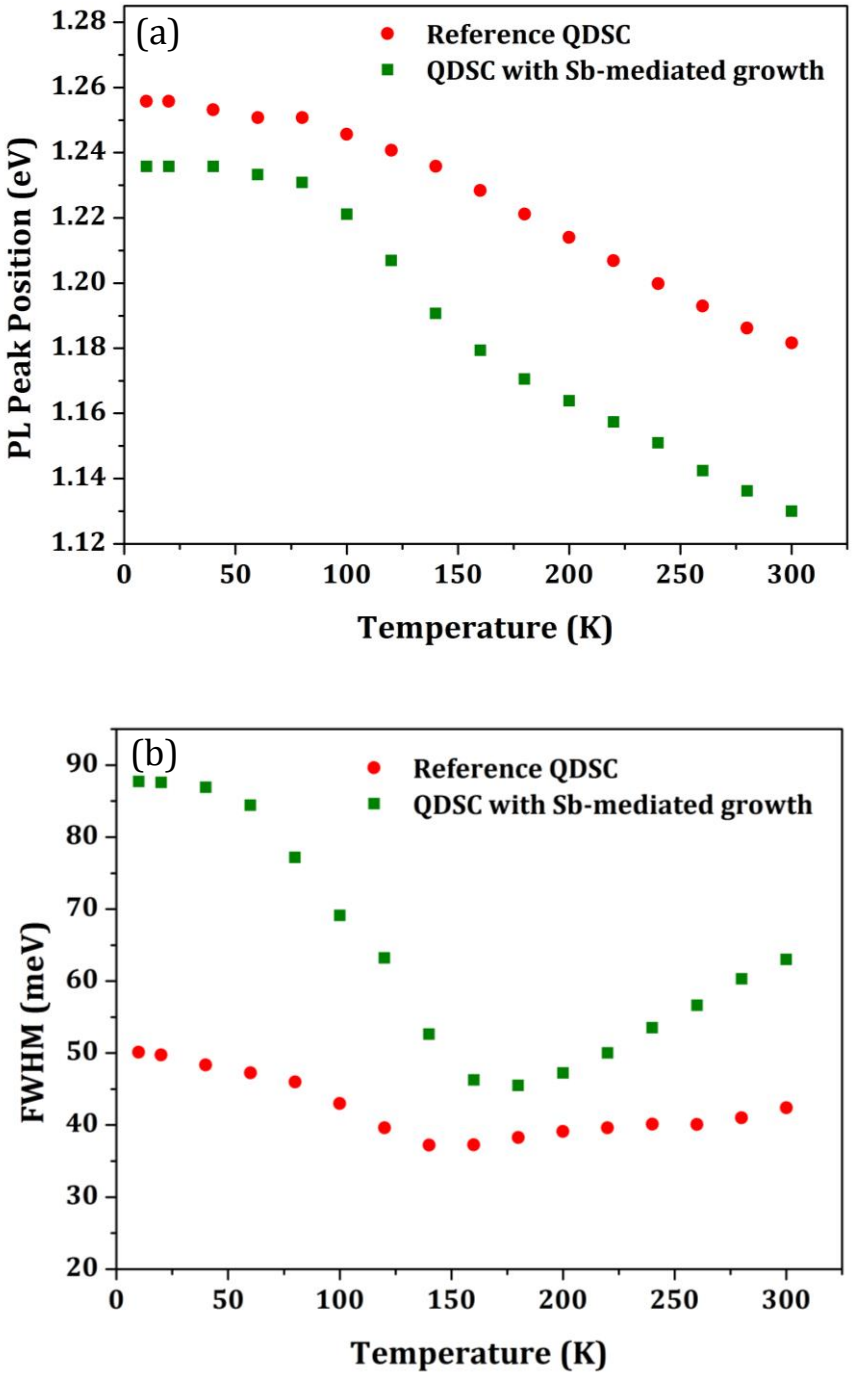

Figure 6.11 PL emission peak positions (a) and FWHM (b) as a function of temperature for the reference QDSC and the QDSC with Sb-mediated growth.

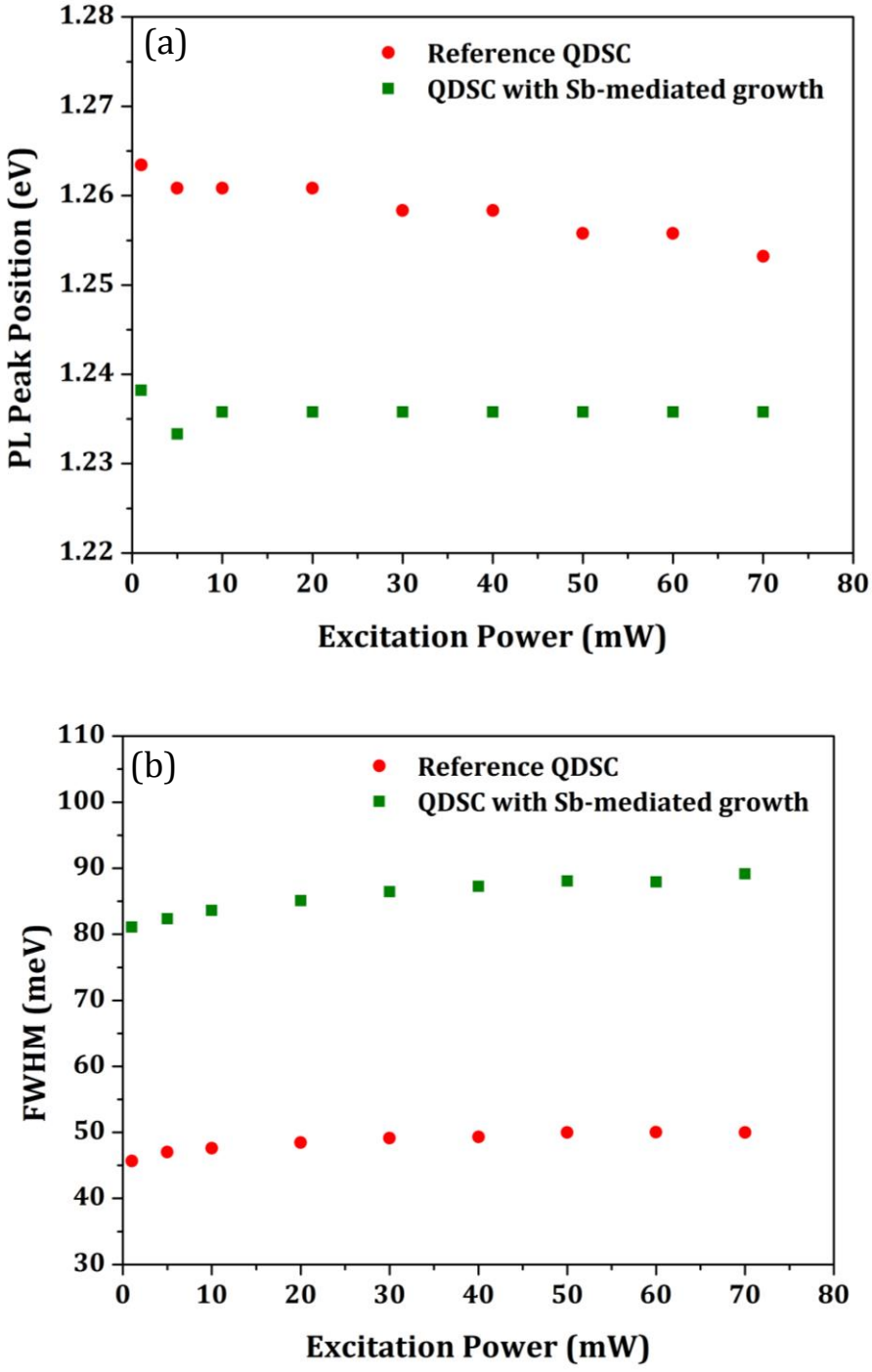

Figure 6.12 PL emission peak positions (a) and FWHM (b) as a function of excitation power for the reference QDSC and the QDSC with Sb-mediated growth

The effect of increasing excitation power (1 – 70 mW) on the PL emission energy and the FWHM is shown in Figure 6.12. At higher optical excitation powers, both QDSC structures show little change in ground state emission

energies (shown in Figure 6.12 (b)). For even higher excitation powers beyond 70 mW, excited states will be obvious. Figure 6.12 (b) shows a slight increase in FWHM for both QDSCs. This can be attributed to the filling of lower QD states, causing photoexcited carrier to occupy upper QD states.

6.2.3 Solar Cell Performances

Over the device fabrication process more than twenty SC devices were fabricated from each of the three wafers. The final eight had reproducible results and the best performing of these devices are presented. The current density-voltage (*J-V*) characteristics of the reference GaAs cell, reference QDSC, and the high-density QDSC with Sb measured under one sun (AM 1.5) illumination at room temperature is shown in Figure 6.13. The *J-V* curve shows that the GaAs reference SC has an open-circuit voltage (V_{oc}) of 0.90 V, much higher than the reference QDSC (V_{oc} = 0.69 V) and high-density QDSC (V_{oc} = 0.71 V). The degradation of V_{oc} can be attributed to the decreased effective bandgap and thermal coupling between QD energy levels and the GaAs conduction band at one sun illumination [18], [19].

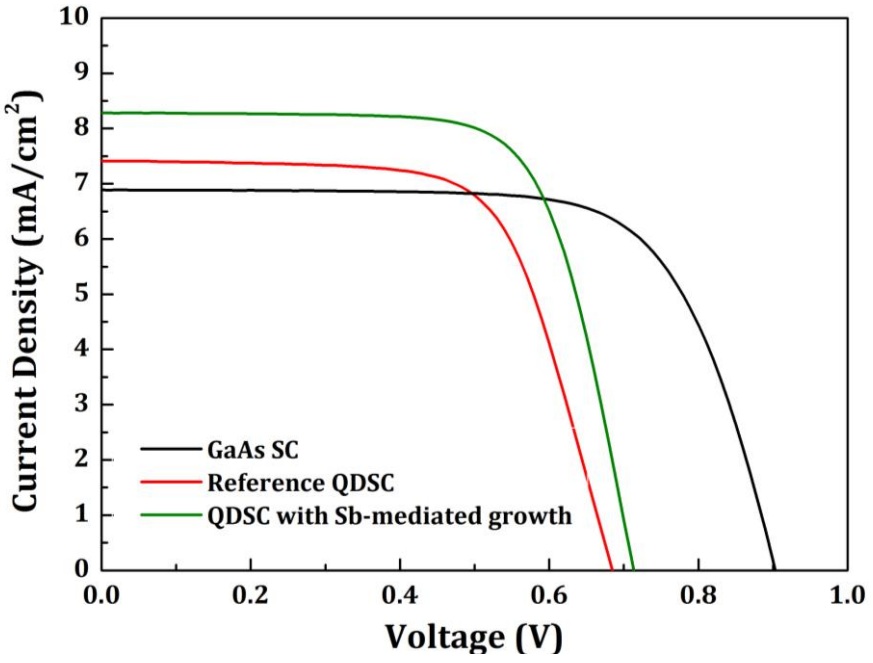

Figure 6.13 Current density vs. voltage curves for the GaAs reference solar cell, the reference QDSC and the QDSC with Sb-mediated growth under 1-sun AM1.5 illumination.

The decrease of the effective bandgap can be overcome by using high energy barriers and growth techniques such as employing AlAs cap layers to eliminate the QD wetting layers [20] as discussed in Chapter 5.

The degradation of V_{oc} due to thermal coupling of the energy level can also be resolved by concentrated solar illumination [21]. The QDSC with Sb-mediated growth shows some V_{oc} recovery, compared with the reference QDSC. Since Sb irradiation leads to a reduction of In adatom diffusion length, this suppresses intermixing between InAs and GaAs to form InGaAs during the QD capping process. The preservation of InAs QD morphology with Sb leads to higher thermal activation energy for the QDSC with Sb than the reference QDSC without Sb [22]. Therefore, thermal escape of the photo-excited carrier, which has been one of the major reasons for V_{oc} degradation, can be reduced. As a result the dark current density-voltage curve for the high-density QDSC with Sb is reduced compared to the reference QDSC as shown in Figure 6.14.

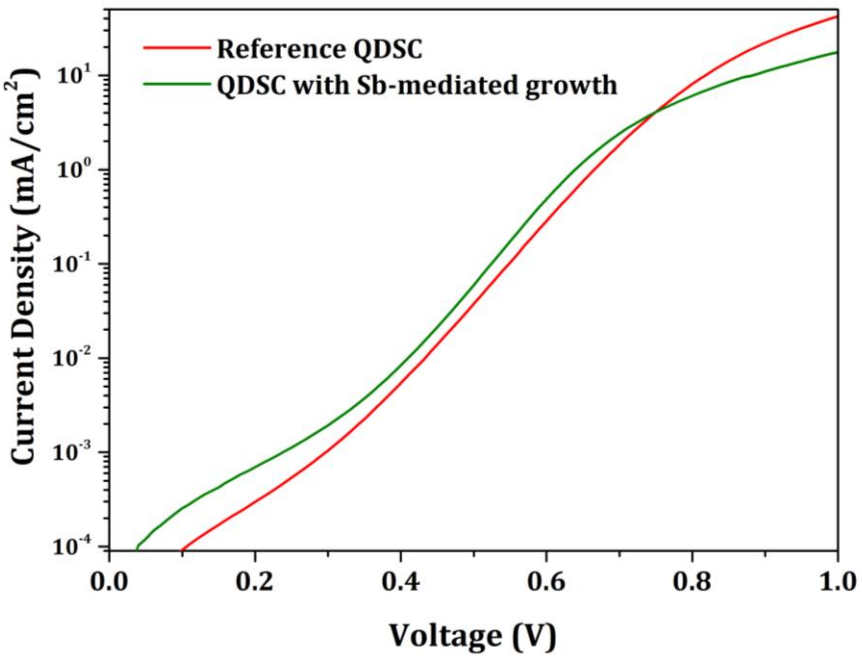

Figure 6.14 Dark current-density of the QDSCs

Even though, both QDSCs suffer from a voltage drop, the J_{sc} of the QDSCs have larger values compared with the GaAs reference cell. By inserting 20 layers of QDs without Sb in the GaAs *p-i-n* junction, the J_{sc} increases from 6.9 mA/cm^2 to 7.4 mA/cm^2. The J_{sc} of the high-density QDSC with Sb increases further to 8.3 mA/cm^2, which is about a 20% increase in J_{sc} compared with the reference GaAs cell and 12% compared to the reference QDSC. The degradation of the QDSC V_{oc} is offset by the distinct improvement of J_{sc}. By using QD arrays, the photon absorption wavelength is extended to 1100 nm. The *J-V* and EQE results clearly show the advantage of using Sb-mediated QDs in solar cells. The QDSC structures are identical except the QD layer; the reference QDSC and high-density QDSC with Sb have in-plane QD density of 4.8×10^{10} cm^{-2} and 1.0×10^{11} cm^{-2} respectively. The improvement in J_{sc} of QDSCs is due to the GaAs sub-bandgap photon absorption by the high-density QDs, which is confirmed by the EQE measurements shown in Figure 6.15.

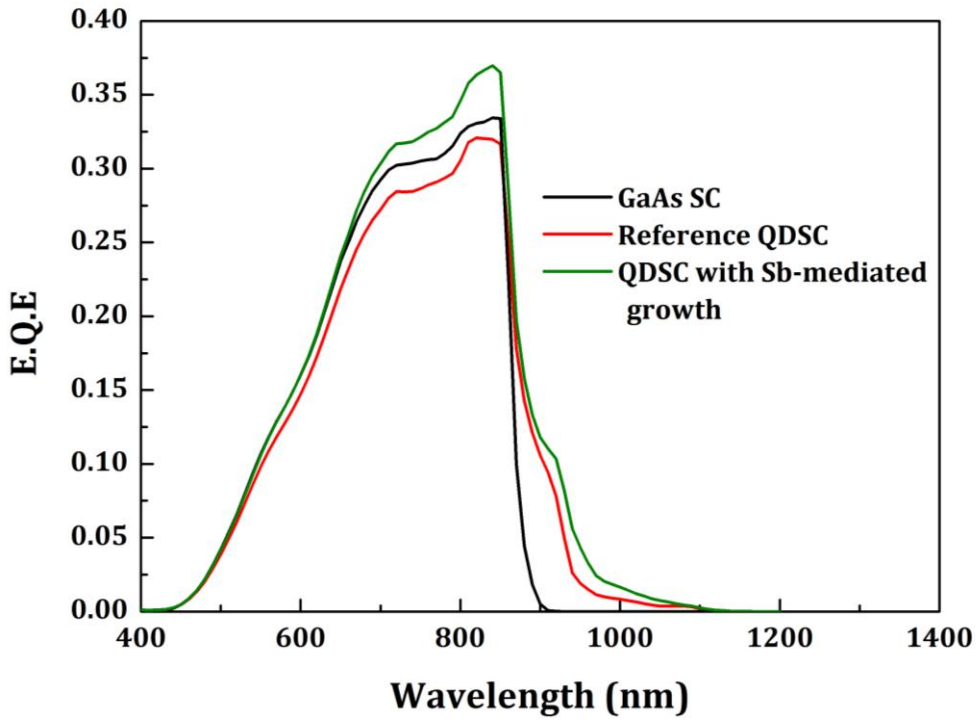

Figure 6.15 External quantum efficiency of the reference GaAs solar cell, reference QDSC and QDSC with Sb-mediated growth

As shown by the PL intensity difference (in Figure 6.8) between the reference QDSC and QDSC with Sb also supports the significantly increased QD density by using Sb. In addition, since Sb is a surfactant, the incorporation of residual Sb during the GaAs emitter growth can improve the material quality and positively affect the minority carrier transport properties, and this might explain the increased EQE of the QDSC with Sb at the GaAs band edge. The mechanism by which this occurs is the subject of further studies. In order to show the contribution of the high-density QD arrays to the enhanced J_{sc}, the EQE spectra of the QDSC with and without Sb are compared and plotted in Figure 6.16. The relative EQE values of the QDSCs above GaAs bandgap are found to be similar. In the GaAs sub-bandgap wavelength region, the EQE of QDSC with Sb is about twice as strong as that of the reference QDSC. The magnitude of improvement in EQE correlates well with the PL spectra and QD density estimated by AFM measurements. Therefore, it is safe to conclude that the improved J_{sc} of QDSC with Sb was due to the high-density QDs in addition to possible material quality improvement caused by Sb-mediated growth.

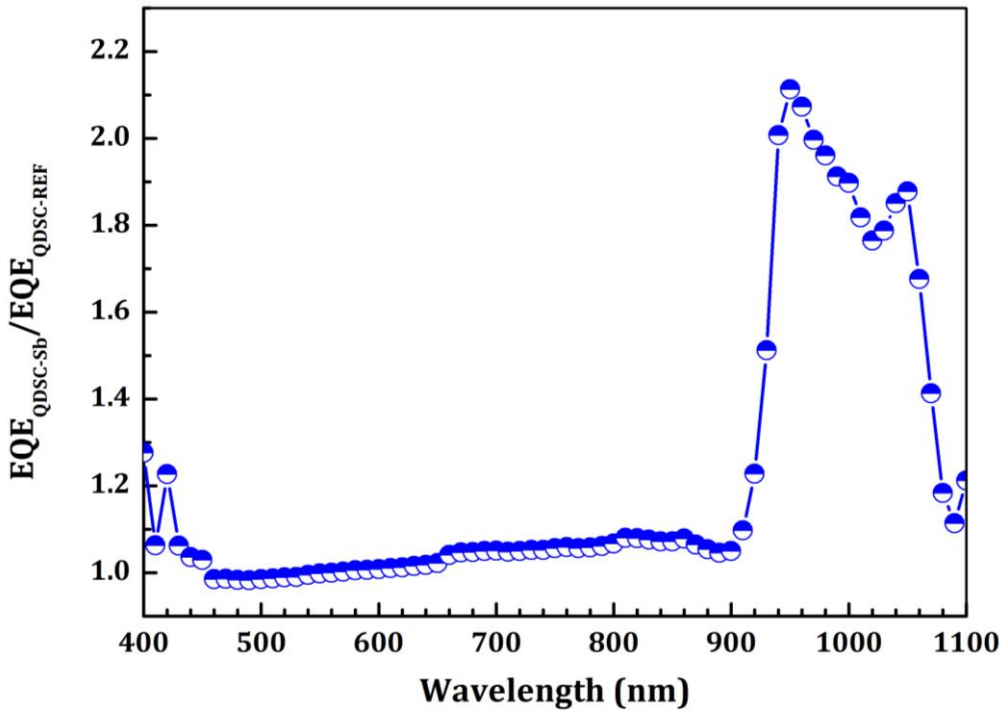

Figure 6.16 External quantum efficiency ratio between reference QDSC and high density QDSC.

In terms of efficiency, the enhancement of the J_{sc} in the QDSC with Sb, leads to an efficiency of 4.18%, compared with 3.40% for the reference QDSC and 4.36% for the GaAs SC. Again as with the previous chapter, the GaAs contact layer was left un-etched during the device fabrication, leading to the relatively low efficiency values for all the cells. Table 6.1 presents a summary of the solar cell parameters.

Solar Cells	*Jsc* (mA/cm²)	*Voc* (V)	*FF* (%)	*η* (%)
GaAs Reference Cell	6.89	0.90	70	4.36
Reference QDSC	7.41	0.69	67	3.40
QDSC with Sb-mediated growth	8.28	0.71	70	4.18

Table 6.1 Short-circuit current (*Jsc*), open-circuit voltage (*Voc*), fill factor (*FF*), and efficiency (*η*) for the QDSCs and GaAs SC under 1 sun AM1.5 illumination.

6.3 Ongoing Work

6.3.1 InAs/GaAs quantum dot solar cell with AlAs Cap Layer and Sb-Mediated Growth

Having shown the enhancement of the open-circuit voltage by the AlAs cap layer in Chapter 5 and the increase in short-circuit current by Sb-mediated growth in this chapter, the two techniques were brought together in a single QDSC structure. As intended, the external quantum efficiency presented in Figure 6.17 shows both an absence of the WL and an increase in QD absorption. From initial results it is clear to see the potential of AlAs CL and Sb in advancing the march towards the implementation of the QD IBSC.

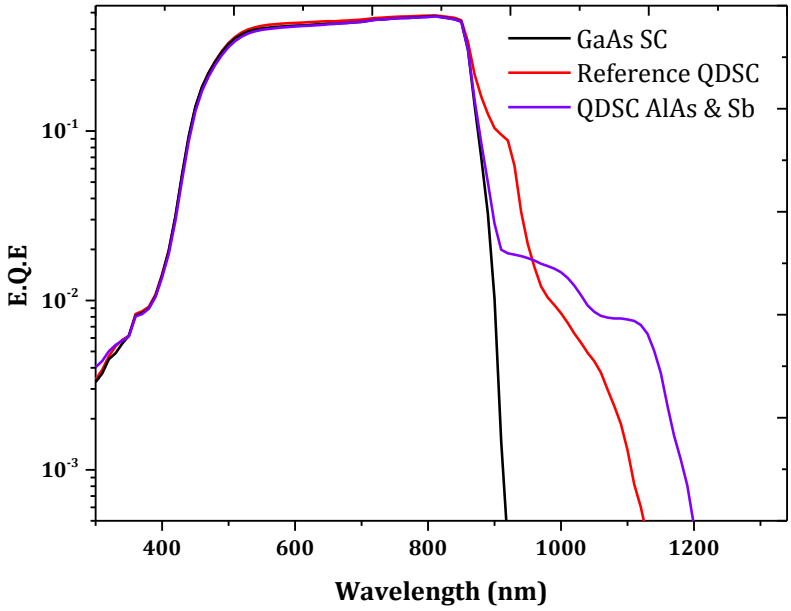

Figure 6.17 External quantum efficiency of the reference QDSC, the QDSC with AlAs CL and Sb, and the GaAs reference solar cell

6.3.2 InAs/InGaP quantum dot solar cell

The work on InAs/GaAs QDSC with an AlAs cap layer has highlighted the importance of the need to increase the transition energy separation between the would-be IB (electron energy levels in the QDs) and the continuum states in the CB. Without this energy separation, thermal escape will be the mechanism by which electrons in the QD move into the CB after excitation from the VB. The thermal escape prevents the occurrence of the second sub-bandgap absorption from the IB to the CB, and this not compatible with the preservation of the open-circuit voltage. Although the second sub-bandgap absorption for QDSCs has been observed at low temperatures, it remains elusive at room temperature.

As a means of promoting the second sub-bandgap absorption in QD IBSCs it has been proposed that embedding the QDs in a high bandgap material such as AlGaAs will result in a wider energy separation between the QD electron energy levels and the CB. Since AlGaAs is an indirect bandgap material, better

results might be achieved with a direct and high bandgap material such as InGaP. The design and growth of InAs/InGaP QDSCs has already been completed. $In_{0.49}Ga_{0.51}P$ was grown lattice-matched to the GaAs substrate. The whole *p-i-n* structure was grown using $In_{0.49}Ga_{0.51}P$, with the exception of the window layer which was $Al_{0.52}In_{0.48}$ P, and the p^+ contact layer which was GaAs. The fabrication of solar cell devices from these wafer samples are yet to be completed.

6.4 Conclusion

In conclusion, we optimized the growth of Sb-mediated high-density QDs by MBE. High-density QDs, which was more than twice as dense as that of conventional QDs, is achieved. With moderate growth temperature and InAs coverage, defective cluster density was reduced down to 1.0×10^{8} cm^{-2} while maintaining coherent QD density as high as $\sim1.0\times10^{11}$ cm^{-2}. By inserting the InAs QDs in the intrinsic region of the *p-i-n* GaAs solar cells, the EQE spectra were extended to 1100 nm, which made a substantial contribution to the J_{sc} of the QDSCs. The QDSC with Sb-mediated growth demonstrated a further improvement in GaAs sub-bandgap spectral response in the near infrared region and hence the J_{sc}. Compared with the reference QDSC, there was a 12% increase in J_{sc} for the QDSC with Sb, along with a slight V_{oc} recovery. This result shows that under one sun illumination, a significant increase in J_{sc} could compensate for the typical V_{oc} degradation of QDSCs.

Bibliography

[1] A. Marti, L. Cuadra, and A. Luque, "Quantum dot intermediate band solar cell," in *Conference Record of the 28th IEEE Photovoltaics Specialists Conference*, 2000, pp. 940–943.

[2] T. Sugaya, S. Furue, H. Komaki, T. Amano, M. Mori, K. Komori, S. Niki, O. Numakami, and Y. Okano, "Highly stacked and well-aligned In[sub 0.4]Ga[sub 0.6]As quantum dot solar cells with In[sub 0.2]Ga[sub 0.8]As cap layer," *Appl. Phys. Lett.*, vol. 97, no. 18, p. 183104, 2010.

[3] S. M. Hubbard, C. D. Cress, C. G. Bailey, R. P. Raffaelle, S. G. Bailey, and D. M. Wilt, "Effect of strain compensation on quantum dot enhanced GaAs solar cells," *Appl. Phys. Lett.*, vol. 92, no. 12, p. 123512, 2008.

[4] R. Oshima, A. Takata, and Y. Okada, "Strain-compensated InAs/GaNAs quantum dots for use in high-efficiency solar cells," *Appl. Phys. Lett.*, vol. 93, no. 8, p. 083111, 2008.

[5] H. Lu, S. Mokkapati, and L. Fu, "Plasmonic quantum dot solar cells for enhanced infrared response," *Appl. Phys. …*, vol. 103505, 2012.

[6] J. Wu, S. C. Mangham, V. R. Reddy, M. O. Manasreh, and B. D. Weaver, "Surface plasmon enhanced intermediate band based quantum dots solar cell," *Sol. Energy Mater. Sol. Cells*, pp. 1–6, Apr. 2012.

[7] P. Aivaliotis, L. R. Wilson, E. a. Zibik, J. W. Cockburn, M. J. Steer, and H. Y. Liu, "Enhancing the dot density in quantum dot infrared photodetectors via the incorporation of antimony," *Appl. Phys. Lett.*, vol. 91, no. 1, p. 013503, 2007.

[8] D. Zhou, G. Sharma, S. F. Thomassen, T. W. Reenaas, and B. O. Fimland, "Optimization towards high density quantum dots for intermediate band solar cells grown by molecular beam epitaxy," *Appl. Phys. Lett.*, vol. 96, no. 6, pp. 061913–3, 2010.

[9] F. K. Tutu, I. R. Sellers, M. G. Peinado, C. E. Pastore, S. M. Willis, a. R. Watt, T. Wang, and H. Y. Liu, "Improved performance of multilayer InAs/GaAs quantum-dot solar cells using a high-growth-temperature GaAs spacer layer," *J. Appl. Phys.*, vol. 111, no. 4, p. 046101, 2012.

[10] H. Y. Liu, I. R. Sellers, T. J. Badcock, D. J. Mowbray, M. S. Skolnick, K. M. Groom, M. Gutiérrez, M. Hopkinson, J. S. Ng, J. P. R. David, and R. Beanland, "Improved performance of 1.3 μm multilayer InAs quantum-dot lasers using a high-growth-temperature GaAs spacer layer," *Appl. Phys. Lett.*, vol. 85, no. 5, p. 704, 2004.

[11] T. Kanto and K. Yamaguchi, "In-plane self-arrangement of high-density InAs quantum dots on GaAsSb/GaAs(001) by molecular beam epitaxy," *J. Appl. Phys.*, vol. 101, no. 9, p. 094901, 2007.

[12] N. Kakuda, S. Tsukamoto, A. Ishii, K. Fujiwara, T. Ebisuzaki, K. Yamaguchi, and Y. Arakawa, "Surface reconstructions on Sb-irradiated GaAs(001) formed by molecular beam epitaxy," *Microelectronics J.*, vol. 38, no. 4–5, pp. 620–624, Apr. 2007.

[13] D. Leonard, K. Pond, and P. Petroff, "Critical layer thickness for self-assembled InAs islands on GaAs," *Phys. Rev. B*, vol. 50, no. 16, 1994.

[14] H. Y. Liu, B. Xu, Y. H. Chen, D. Ding, and Z. G. Wang, "Effects of seed layer on the realization of larger self-assembled coherent InAs/GaAs quantum dots," *J. Appl. Phys.*, vol. 88, no. 9, p. 5433, 2000.

[15] T. Bray, Y. Zhao, P. Reece, and S. P. Bremner, "Photoluminescence of antimony sprayed indium arsenide quantum dots for novel photovoltaic devices," *J. Appl. Phys.*, vol. 113, no. 9, p. 093102, 2013.

[16] E. Grilli, M. Guzzi, R. Zamboni, and L. Pavesi, "High-precision determination of the temperature dependence of the fundamental energy gap in gallium arsenide.," *Phys. Rev. B. Condens. Matter*, vol. 45, no. 4, pp. 1638–1644, Jan. 1992.

[17] H. S. Lee, J. Y. Lee, T. W. Kim, D. U. Lee, D. C. Choo, M. Jung, and M. D. Kim, "Microstructural and optical properties of InAs/GaAs quantum dots embedded in modulation-doped Al[sub x]Ga[sub 1−x]As/GaAs heterostructures," *J. Appl. Phys.*, vol. 91, no. 8, p. 5195, 2002.

[18] D. Guimard, R. Morihara, D. Bordel, K. Tanabe, Y. Wakayama, M. Nishioka, and Y. Arakawa, "Fabrication of InAs/GaAs quantum dot solar cells with enhanced photocurrent and without degradation of open circuit voltage," *Appl. Phys. Lett.*, vol. 96, no. 20, p. 203507, 2010.

[19] A. Luque and A. Marti, "The intermediate band solar cell: progress toward the realization of an attractive concept.," *Adv. Mater.*, vol. 22, no. 2, pp. 160–174, Jan. 2010.

[20] F. K. Tutu, P. Lam, J. Wu, N. Miyashita, Y. Okada, K.-H. Lee, N. J. Ekins-Daukes, J. Wilson, and H. Liu, "InAs/GaAs quantum dot solar cell with an AlAs cap layer," *Appl. Phys. Lett.*, vol. 102, no. 16, p. 163907, 2013.

[21] P. Linares, A. Martí, E. Antolín, C. D. Farmer, I. Ramiro, C. R. Stanley, and A. Luque, "Voltage recovery in intermediate band solar cells," *Sol. Energy Mater. Sol. Cells*, vol. 98, pp. 240–244, 2012.

[22] X. Yang, T. Yang, K. Wang, H. Ji, H. Ni, Z. Niu, and Z. Wang, "Effect of antimony irradiation on InAs/Sb:GaAs quantum dots grown by molecular beam epitaxy," *Semicond. Sci. Technol.*, vol. 26, no. 7, p. 075010, Jul. 2011.

Chapter 7

Conclusion and Future Work

This chapter summarises the efforts on implementing quantum dot solar cell, as discussed in the previous chapters of this thesis. The salient achievements of the different solar cells are highlighted and the conclusions emerging from this work are presented. There is also a brief discussion of future work that could be done to progress the development of quantum dot solar cells.

7.1 Summary and Conclusions

There is a significant loss in conventional bulk semiconductor solar cells due to sub-bandgap photons. In order to overcome the Shockley-Quiesser limit for solar cells [1], the intermediate band solar cell (IBSC) has been proposed. The idea behind this approach is the introduction of an intermediate band within the bandgap of a semiconductor, allowing sub-bandgap photons to be leveraged. This will lead to an increase in the photocurrent from the cell, and provided that the output voltage is not reduced, an increase in efficiency will be attained. The goal of this research project was the realisation of III-V quantum dot (QD) IBSCs. The work presented in this thesis focused on the design, epitaxial growth (on GaAs substrates), device fabrication and characterisation of III-V QDSC for the implementation of IBSCs.

A study of the influence of growth conditions of GaAs spacer layers on 30-layer InAs/GaAs dot-in-well solar cells was first conducted. TEM images showed that the adoption of a high growth temperature spacer layer technique suppressed the formation of defects, resulting in a cell with a significant increase in short-circuit current [2]. The key operating principles of the QD IBSC have been demonstrated by the InAs/GaAs material system. However, the presence of the wetting layer (WL) and the valence band (VB) offset mean that, even though an increase of the current is observed, it is accompanied by a significant drop in open-circuit voltage. Therefore, one approach to enhancing the cell operation with respect to epitaxial growth is the growth of QD structures without a wetting layer or VB offset. A number of material structures have been proposed that seek to achieve this. In order to increase the contribution of QDs to the photocurrent, a high dot density is vital. This requires the increase in dot density per layer or the ability to stack many dot layers with little accumulated stress.

In an attempt to preserve the open-circuit voltage, the WL of an InAs/GaAs QDSC structure was eliminated by the use of an AlAs cap layer. External quantum efficiency measurements clearly show the absence of the WL, resulting in an enhanced open-circuit voltage [3]. Without the WL, the resulting increase in energy separation between the QD electron energy levels and the continuum states in the conduction band (CB) illustrated a key step in the realisation of QD IBSCs using III-V materials. The need to increase sub-bandgap photon absorption by the QDs was further addressed by the use of Sb-mediated growth. After optimisation of the growth temperature and InAs amount for the Sb-mediated growth, a QDSC was fabricated with a very high density of InAs QDs ($\sim 1 \times 10^{11}/cm^2$) [4]. This result showed that a significant increase in short-circuit current could compensate for the drop in open-circuit voltage observed in InAs/GaAs QDSCs.

By combining the effects of the AlAs cap layer and Sb-mediated growth, the achievement of this work has been to clearly highlight a path to the implementation of QD IBSCs. A higher energy separation between the CB

edge and the QD energy levels, and an increase in QD density has been demonstrated. The growth of InAs quantum dots in InGaP, a high bandgap material was also demonstrated, and has the potential of achieving distinct quasi-Fermi levels and encouraging the second sub-bandgap absorption in QD IBSCs. The presented results for the QDSC with AlAs cap, the QDSC with Sb-mediated growth and these ongoing works represent progress towards the implementation of IBSCs with QDs.

7.2 Future Work

There is still much to be explored with regard to the implementation of QD IBSCs. Future work will continue to focus on the development of novel III-V material systems for QD IBSCs. As a next step from InAs/GaAs QDSCs, the InAs/GaAsSb QD material system has been shown to eliminate the VB offset and hence proves promising for QDSCs. An improvement in the carrier lifetime of the QD region due to the type II band alignment makes this material system one to consider [5]. The caveat is that GaAsSb is not lattice-matched to GaAs, and so a lot of consideration must be given to the maintenance of strain in the structure.

Direct Si-doping of QDs has been shown to improve the material quality of QD structures and in the case of InAs/GaAsN QD structures, even lead to two-photon absorption at room temperature [6]. This is a very important step for QD IBSCs and it is one that needs be investigated as part of any future work on QDSCs. There is also a unique opportunity to work with QD material systems containing phosphorous since the UCL MBE facility is custom designed with a white-phosphorus temperature controller, unlike most MBE systems. This is advantageous because it ensures a stable phosphorus flux and composition. InP/GaAsP and InPSb/GaAs QDSC structures also show some promise [7].

Having already demonstrated the first QD lasers to be realised on a Ge-on-Si substrate, there is also a real opportunity within the UCL MBE Group for the

growth of III-V QDSC structures on Ge or Si substrates [8]. Developing low-cost and high-efficiency III-V/Si solar cell structures is a challenging but worthwhile pursuit. It is apparent that any significant advancement in photovoltaic technology will have to adopt a low cost manufacture approach, and the successful growth of III-V solar cells on Si will be a huge step in that direction.

Bibliography

[1] W. Shockley and H. J. Queisser, "Detailed Balance Limit of Efficiency of p-n Junction Solar Cells," *J. Appl. Phys.*, vol. 32, no. 3, p. 510, 1961.

[2] F. K. Tutu, I. R. Sellers, M. G. Peinado, C. E. Pastore, S. M. Willis, a. R. Watt, T. Wang, and H. Y. Liu, "Improved performance of multilayer InAs/GaAs quantum-dot solar cells using a high-growth-temperature GaAs spacer layer," *J. Appl. Phys.*, vol. 111, no. 4, p. 046101, 2012.

[3] F. K. Tutu, P. Lam, J. Wu, N. Miyashita, Y. Okada, K.-H. Lee, N. J. Ekins-Daukes, J. Wilson, and H. Liu, "InAs/GaAs quantum dot solar cell with an AlAs cap layer," *Appl. Phys. Lett.*, vol. 102, no. 16, p. 163907, 2013.

[4] F. K. Tutu, J. Wu, P. Lam, M. Tang, N. Miyashita, Y. Okada, J. Wilson, R. Allison, and H. Liu, "Antimony mediated growth of high-density InAs quantum dots for photovoltaic cells," *Appl. Phys. Lett.*, vol. 103, no. 4, p. 043901, 2013.

[5] K. Nishikawa, Y. Takedo, K. Yamanaka, T. Motohiro, D. Sato, J. Ota, N. Miyashita, and Y. Okada, "Over 100 ns intrinsic radiative recombination lifetime in type II InAs/GaAs1â^' xSbx quantum dots," *Appl. Phys. Lett.*, vol. 111, p. 044325, 2012.

[6] Y. Okada, T. Morioka, K. Yoshida, R. Oshima, Y. Shoji, T. Inoue, and T. Kita, "Increase in photocurrent by optical transitions via intermediate quantum states in direct-doped InAs/GaNAs strain-compensated quantum dot solar cell," *J. Appl. Phys.*, vol. 109, no. 2, p. 024301, 2011.

[7] M. Y. Levy and C. B. Honsberg, "Nanostructured Absorbers for Multiple Transition Solar Cells," *IEEE Trans. Electron Devices*, vol. 55, no. 3, pp. 706–711, Mar. 2008.

[8] H. Liu, T. Wang, Q. Jiang, R. Hogg, F. Tutu, F. Pozzi, and A. Seeds, "Long-wavelength InAs/GaAs quantum-dot laser diode monolithically grown on Ge substrate," *Nat. Photonics*, no. JUNE, pp. 1–4, Jun. 2011.